ABSTRACT

VETTER, ERIC PHILIP. Semiconductor Spintronics: Spin Transport and Dynamics in Organic, Inorganic, and Hybrid Semiconductor Materials. (Under the direction of Drs. Jacob Jones and Dali Sun).

Spin-based electronics seek to utilize the properties of electron spin in order to develop next-generation devices with novel functionalities and applications. As with conventional electronics, semiconductors play a critical role in spintronics by allowing for the active manipulation of information carriers. The ability to control the transport and dynamics of spins inside of a semiconductor material is a primary goal of spintronics. Towards this end, a thorough understanding of spin behavior in different semiconductor materials warrants further development. This dissertation investigates spin transport and dynamics in a variety of semiconductor materials comprising inorganic, organic, and hybrid organic-inorganic components with the aim of furthering the fundamental knowledge of these promising materials for spintronics applications.

The first chapter of this thesis provides a brief overview of spintronics history and the underlying physical phenomena that allow for the manipulation of spin-based devices. Spin current generation and spin-to-charge interconversion are explained in the context of the spin Hall and Rashba-Edelstein effects. Experimental methods for generating pure spin currents through both continuous-wave microwave and ultrafast pulsed laser excitations are examined.

Chapter 2 details the experimental methods used to fabricate and measure the spintronics devices studied in this thesis. The first half of this chapter discusses sample fabrication with regard to vacuum deposition methods used for the development of magnetic thin films. The latter half of this chapter discusses spin pumping measurements conducted at both room and low temperature.

Chapter 3 represents the main body of this work and is split into three sections. The first section deals with organic semiconductor spintronics and examines the major differences in spin transport and spin relaxation in these materials as compared with their inorganic counterparts. A manuscript about the effects of structural conformation on spin-orbit coupling in conjugated polymers is detailed here. The following section touches on inorganic semiconductors and their application in spintronics. Problems associated with spin injection into these materials and ways to overcome them are discussed. A published manuscript investigating spintronic THz emission from a NiFe/*n*-GaN heterostructure is reproduced here, and the effects of carrier concentration on emitted THz intensity are analyzed. The last section of this chapter touches on the recent advent of hybrid organic-inorganic perovskite semiconductor spintronics. Spin-dependent phenomena in this class of materials is briefly discussed, followed by a publication on the observation of long spin lifetimes in single crystal $MAPbBr_3$ as determined by oblique spin pumping studies.

Finally, Chapter 4 concludes this thesis and offers some future outlooks for the materials discussed here.

Semiconductor Spintronics: Spin Transport and Dynamics in Organic, Inorganic, and Hybrid Semiconductor Materials

by
Eric Philip Vetter

A dissertation submitted to the Graduate Faculty of
North Carolina State University
in partial fulfillment of the
requirements for the degree of
Doctor of Philosophy

Materials Science and Engineering

Raleigh, North Carolina
2021

APPROVED BY:

Dr. Jacob Jones
Committee Chair

Dr. Dali Sun
Committee Co-Chair

Dr. Elizabeth Dickey

Dr. Lew Reynolds Jr.

Dr. Divine Kumah

DEDICATION

This dissertation is dedicated to the love of my life, Vanessa, and to my mother Judy and father Steve for their constant support and encouragement that have sustained me in all of my endeavors. You inspire me to be a better person every single day and my accomplishments would not be possible without you.

BIOGRAPHY

Eric Vetter was born in Fairfax, Virginia on February 16, 1993. He received his Bachelor of Science in Chemistry with a specialization in Materials Science from the University of Virginia in 2015. He spent an additional year at UVa following graduation in order to finish his research project on magnetic nanostructures in CoPt alloys before starting his PhD in Materials Science and Engineering at North Carolina State University in 2016. He joined Professor Dali Sun's research group in 2017 with plans to graduate in the Spring of 2021.

ACKNOWLEDGMENTS

I would like to acknowledge everyone who has helped me during my PhD. First, to Vanessa, I would not have made it far without your love, support, and guidance. You are an unwavering light in dark times, a voice of reason when I need it most, and my foremost joy in this world. I love you more than words can express, forever and always.

To my friends Dennis and James, you have been by my side throughout this entire journey and I have watched our friendship flourish in good times and display resilience in bad. You are like brothers to me, and while I will be sad to part ways as we near the end of our time here I know you are both destined for success and happiness in whatever you do. Even when distance separates us our friendship will not fade, and I am excited to see what the future has in store for us.

To my family, Mom, Dad, and Dana, thank you for always being there for me when I need you and for supporting and encouraging me always. I do not express often enough how grateful I am for you and everything you do for me.

To Dali, my professor, you have been a wonderful mentor and teacher over the past years. Your optimism and excitement for science is unshakeable, and I am thankful for your support. I hope you never lose your good cheer and continue to lift up those around you as you achieve great things.

Finally, I would like to acknowledge those at NC State that have helped me at various points in my tenure here. To my committee members; Dr. Reynolds, Dr. Dickey, Dr. Kumah, and Dr. Jones – Thank you so much for everything. To my labmate, Zhengjie, thank you for putting up with me and I wish you great luck in all your endeavors.

TABLE OF CONTENTS

LIST OF FIGURES

Chapter 1

Spintronics

The spin based devices described in this dissertation build on an extensive body of research in the field of spintronics, and the first part of this chapter will provide a brief summary of its history. The subsequent sections will review more recent progress and overview the concepts of spin injection and detection.

1.1 History

Spintronics, a portmanteau of "spin electronics", can trace its origin back to the discovery of solid state electron tunneling in 1958 by Japanese researcher Leo Esaki, who was working for Sony (then called Tokyo Tushin Kogyo) at that time. Dr. Esaki shared the 1973 Nobel Prize in Physics along with Ivar Giaever, "for their experimental discoveries regarding tunneling phenomena in semiconductors and superconductors, respectively." [1]

His work paved the way for the subsequent discovery of tunnel magnetoresistance (TMR) in 1975 by Michel Jullière, who observed electron tunneling between two ferromagnetic electrodes separated by a semiconducting barrier in a Fe-Ge(amorphous)-Co tunnel junction [2]. The relative conductance of this device depended on the magnetization direction of the respective electrodes as determined by the external magnetic field strength and direction in conjunction with the electrodes' differential coercivities, although the maximum magnetoresistance was limited to about 14% at 4.2 K in his study. Jullière explained the resultant magnetoresistance effect based on the spin polarization potential of the ferromagnets calculated from the spin dependent density of states (DOS) at the Fermi energy. The Jullière model, as depicted in Figure 1, expresses the

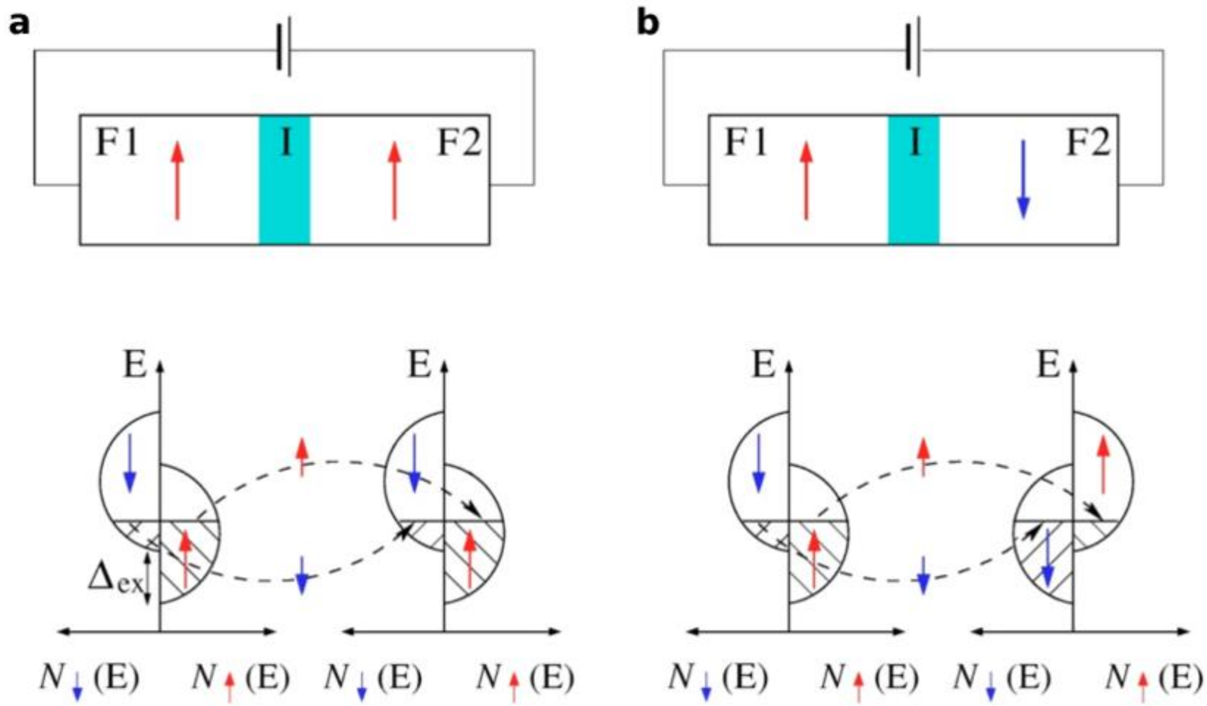

Figure 1. Schematic illustration of Julliere's tunnel magnetoresistance model depicting electron tunneling in a ferromagnet / insulator / ferromagnet (F1/I/F2) tunnel junction with (a) parallel and (b) antiparallel magnetization orientations. The spin-resolved density of states in the FM metals have an exchange spin splitting of Δ_{ex}. Red and blue arrows in the two ferromagnetic regions are determined by the majority-spin sub-band and dashed lines represent spin-conserved tunneling. This figure is taken from Ref. [3].

differences in device resistance for parallel (R_p) and antiparallel (R_{ap}) states, defined by the external field direction, as:

$$TMR = \frac{R_{ap} - R_p}{R_p} = \frac{2P_1P_2}{1 - P_1P_2}$$

where the spin polarization P can be calculated from the spin dependent density of states D at the Fermi energy E_F by the relation:

$$P = \frac{D_{\uparrow}(E_F) - D_{\downarrow}(E_F)}{D_{\uparrow}(E_F) + D_{\downarrow}(E_F)}$$

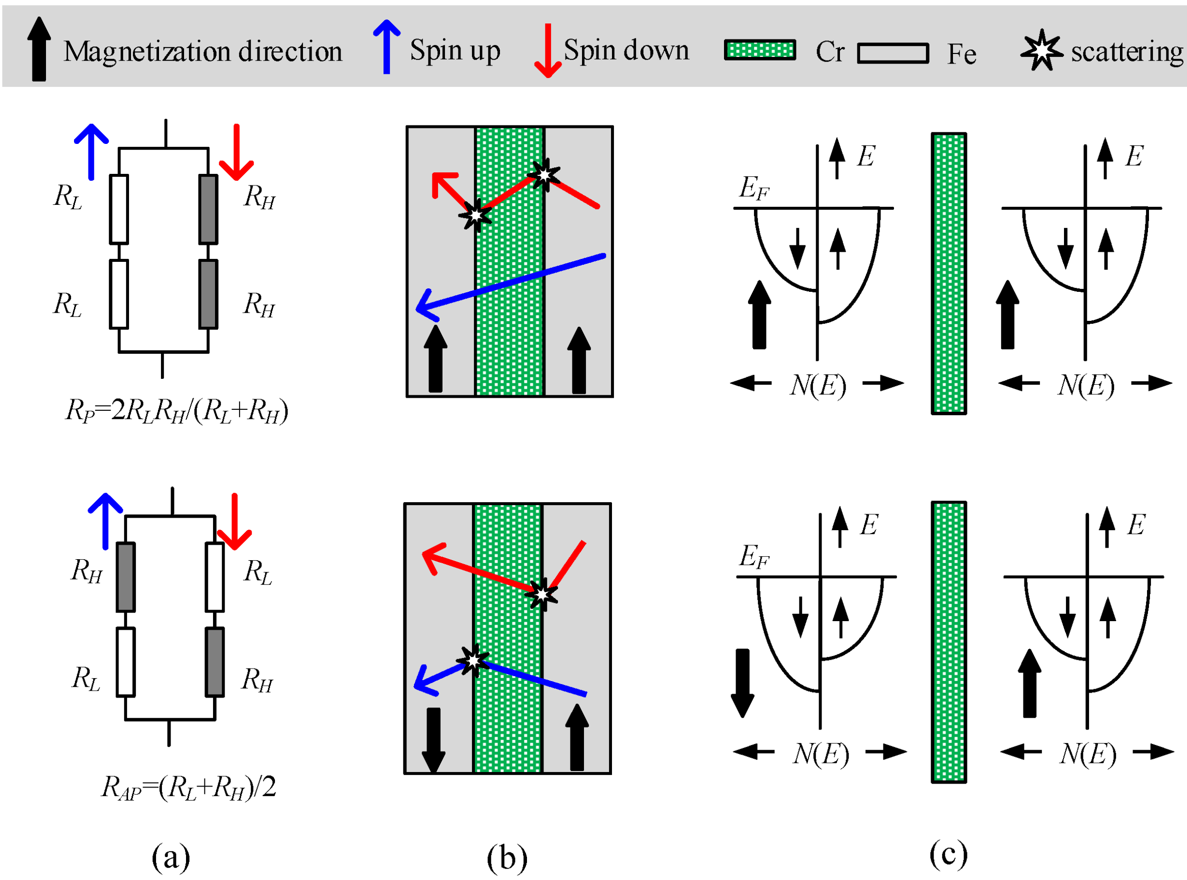

Figure 2. Schematic depictions of (a) resistor model for giant magnetoresistance; (b) spin-dependent scattering at the interfaces between ferromagnetic and non-magnetic layers with parallel (P) and antiparallel (AP) magnetizations; (c) spin-resolved density of states with parallel and antiparallel configurations. E, E_F, and N(E) are the electron energy, Fermi level, and density of states, respectively. This figure is taken from Ref. [4].

A decade later, in the late 1980's, the giant magnetoresistance (GMR) effect was independently discovered by the research groups of Albert Fert and Peter Grünberg [5], [6], for which Fert and Grünberg received the Nobel Prize in Physics in 2007. Their pioneering studies on the antiferromagnetically exchange coupled magnetic multilayers of Fe/Cr/Fe grown by molecular beam epitaxy demonstrated significant magnetoresistance of up to 50% at 4.2 K and 1.5% at room temperature. Their results showed that a spin polarized current traversing two magnetic regions experienced spin-dependent scattering as determined by the local magnetic orientation of the respective layers, as shown schematically in Figure 2, in agreement with the two-channel transport model originally proposed by Nevill Mott in 1936 to explain the sudden increase in resistivity of ferromagnetic metals when heated above their Curie temperature [7]. Here, conduction in magnetic metals can be treated as two independent channels, corresponding to up-spin and down-spin electrons, for which the scattering rates are significantly different as a result of their imbalanced density of states at the Fermi energy.

The technological ramifications related to the discoveries of TMR and GMR are immense and omnipresent in the modern era, where magnetic storage devices taking advantage of these effects have enabled the rapid progress of our present information age. In 1997, less than a decade after the original discovery of GMR, commercial magnetic storage read heads based on GMR went into production at IBM. The company was able to achieve an areal storage density of 1 Gbit/in^2 in a 16.8GB hard drive. This technology quickly became the industry standard until it was supplanted by TMR-based heads in 2004, developed by Seagate. The new TMR devices were able to achieve an areal density of 84 Gbit/in^2 initially, which has since improved to over a Terabit/in^2 by 2014 [8]. Thus, in less than 20 years a two-order of magnitude increase in storage density was accomplished in large part due to the initial discoveries of GMR and TMR. Further advances in spintronics will continue to push these limits and enable unprecedented advances in many other aspects of technology.

1.2 Spin-to-Charge Conversion

The discoveries and implementation of GMR and TMR effects laid the foundation for the field of spintronics, yet the devices premised on these effects are still fundamentally electronic in nature whereby a net flow of charge carriers is necessary for their primary functionality and thus are subject to some of the same physical limitations as conventional electronics. However, more recent progress in spintronics research has realized the ability to control and manipulate pure ‘spin currents’ where a transfer of angular momentum is achieved in the absence of any net charge current, with important implications for the next generation of spin-based devices and applications.

This following sections will detail the physical phenomena involved in the interconversion between pure spin and charge currents in addition to the experimental techniques used to access them. First we will focus on the spin Hall effect and its reciprocal the inverse spin Hall effect, followed by the related but distinct Rashba Edelstein effect and its correspondent inverse. Second we will detail two laboratory techniques used for probing these effects in different material systems: ferromagnetic resonance, a continuous-wave microwave excitation approach used for ‘spin-pumping’, and ultrafast demagnetization, which utilizes femtosecond laser pulses to induce ultrafast spin currents.

1.2.1 Spin Hall and Inverse Spin Hall Effects

A major breakthrough related to the development of spintronics came with the ability to harness pure spin currents and interconvert between them and traditional charge currents as a way to exploit the electron spin degree of freedom for the transport, storage, and processing of information. In a seminal paper published in 1971, Russian physicists Mikhail Dyakonov and Vladimir Perel detailed a novel electron transport phenomenon whereby an unpolarized electrical

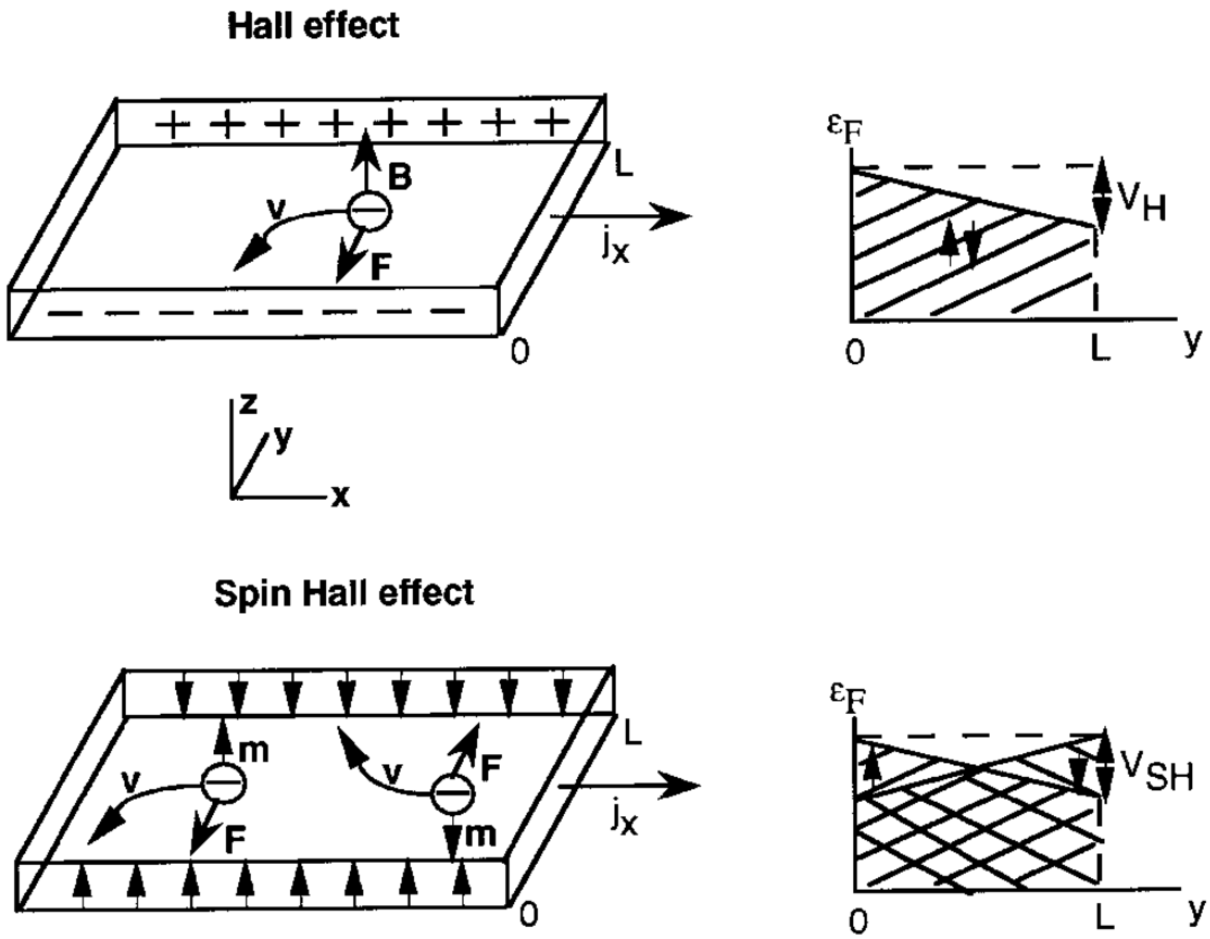

Figure 3. Schematic illustrations of the Hall effect and spin Hall effect. The charge carriers are assumed to be electronlike. In the Hall effect, the Lorentz force on the moving charges causes charge imbalance; in the spin Hall effect skew scattering of the moving magnetic moments causes spin imbalance, in a direction perpendicular to the current flow. In the Hall effect the Fermi levels for up and down electrons are the same, and the difference in the Fermi levels at both edges of the sample is the Hall voltage V_H. In the spin Hall effect the difference in the Fermi levels for each spin at both edges of the sample is V_{SH}, but it is of opposite sign for spin up and down electrons. This figure is taken from Ref. [9].

current passing through a semiconductor sample would generate a spin flow perpendicular to the current direction moving from the bulk of the material to the surface [9]. This process results from spin-orbit effects in electron scattering leading to spin accumulation at the respective surfaces of the sample. The effect would later be re-predicted independently by Jorge E. Hirsch in 1999, where he coined its term it in the titular paper ‘Spin Hall Effect’ that developed its theory phenomenologically with impurity scattering [10]. A year later Zhang extended the effect to the diffusive transport regime [11]. Despite the word ‘Hall’ in its name, the Spin Hall Effect (SHE) is distinct from the classical Ordinary Hall Effect wherein the trajectory of charge carriers is curved by the Lorentz force in the presence of a magnetic field with a component perpendicular to the direction of their travel, as seen in Figure 3.

Roughly a decade after Dyakonov’s original prediction of the Spin Hall Effect, in 1983, Dyakonov and Averkiev proposed an experimental method for the observation of its reciprocal effect, now known as the Inverse Spin Hall Effect (ISHE), where a spin current passing through a material with strong spin-orbit coupling would lead to the generation of a transverse charge current [12]. A year later this would lead to the first experimental observations of this effect being made by the group of V. G. Fleisher [13], [14], who used a circularly polarized laser to excite a surface photocurrent in a sample of $Ga_{0.73}Al_{0.27}As$. The relation between spin and charge currents due to the SHE and ISHE can be expressed as $J_c = J_s \theta_{SH} \times \sigma$, where J_c is the charge current density, J_s is the spin current density, σ is the spin polarization vector, and θ_{SH} is the spin Hall angle which can be regarded as a measure of the conversion efficiency between spin and charge currents.

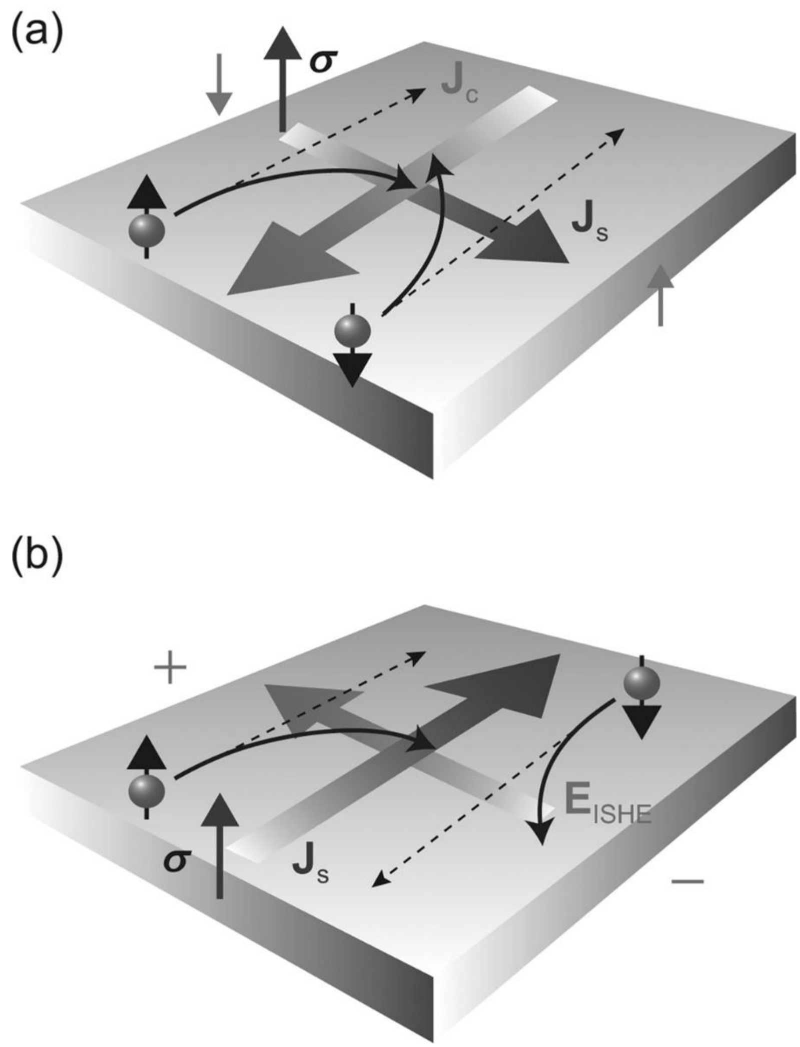

Figure 4. (a) Schematic illustration of the direct spin-Hall effect. J_c, J_s, and σ denote a charge current, the spatial direction of a spin current, and the spin-polarization vector of the spin current, respectively. (b) Schematic illustration of the inverse spin-Hall effect. E_{ISHE}, J_s, and σ denote the electromotive force due to the inverse spin-Hall effect, the spatial direction of a spin current, and the spin-polarization vector of the spin current, respectively. This figure is taken from Ref. [15].

It should be noted that the physical mechanism of spin current generation here as it relates to spin-orbit coupling is extrinsic in nature, where carriers undergo spin-dependent Mott scattering in the form of either skew scattering or the side-jump mechanism controlled by their spin-orbit interaction with impurity centers [16]. An intrinsic mechanism exists where the carriers' trajectories themselves are distorted due to the combined effects of spin-orbit interaction and inversion asymmetry within the material associated with a spin-dependent band structure, which will be detailed in the following section in discussion with the Rashba-Edelstein effect.

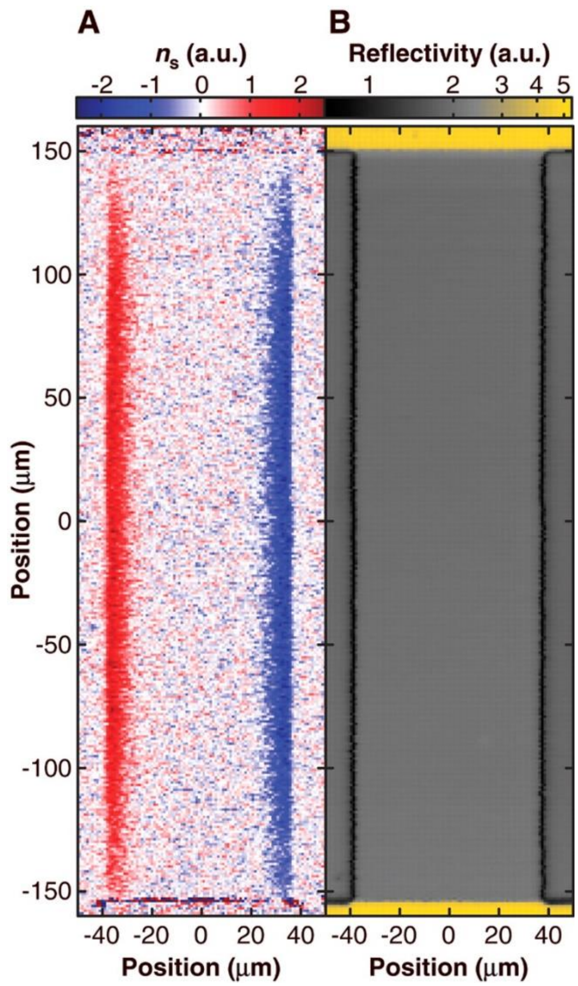

Figure 5. Two-dimensional images of (a) spin density n_s and (b) reflectivity, R, for unstrained GaAs measured at T = 30 K and E = 10 mV μm^{-1}. This figure is taken from Ref. [17].

While experimental observation of the Inverse Spin Hall Effect was thus established, it took over 30 years from the inception of the Spin Hall Effect for its direct observation due to limitations in the ability to unambiguously detect spin accumulation experimentally. However, in the mid-2000's it was ultimately achieved independently by the groups of David Awschalom (UC Santa Barbara, US), through Kerr rotation spectroscopy on unstrained GaAs and strained InGaAs films (see Figure 5) [17], and Tomas Jungwirth (University of Cambridge, UK), by measuring the circular polarization of light emitted from LED structures based on a two-dimensional hole gas in (Al,Ga)As/GaAs heterostructures [18]. These experimental breakthroughs spawned an avalanche of subsequent research interest and publications in the field of spintronics and opened the door for the fabrication of novel spin-based devices.

1.2.2 Rasbha-Edelstein and Inverse Rashba Edelstein Effects

In contrast to the SHE, an intrinsic spin-to-charge mechanism was first proposed by Victor Edelstein in a seminal paper published in 1990 titled "Spin Polarization of Conduction Electrons Induced by Electric Current in Two-Dimensional Asymmetric Electron Systems", which is known today as the Rashba-Edelstein Effect [19]. In his work, Edelstein laid out a theory for the generation of spin polarized conduction electrons resulting from the passage of charge current in a system lacking inversion symmetry at its surface or interfaces, such as in quantum well heterostructures.

The root of this effect can be traced to the spin dependent band structure of the surface or interface states where a lack of structural inversion symmetry in the direction perpendicular to the two-dimensional plane, in addition to atomic spin-orbit coupling, results in the well-known Rashba effect [20]. Here, the effect of the broken symmetry of the system can be added into the Hamiltonian as an electric field and expressed naively as $H_R = -\alpha_R(\sigma \times p) \cdot \hat{z}$, where $\alpha_R =$

$-g\mu_B E_0/2mc^2$ is termed the Rashba parameter. The result is a momentum-dependent splitting of spin bands in the reduced dimensional surface/interface region wherein spin and momentum are now locked within each split branch. The Fermi contours of the spin-split bands trace out two concentric circles with opposite spin helicities when viewed from the $\hat{z}$ direction. In the Rashba-Edelstein Effect (REE), a charge current injected into such a Rashba system perturbs the equilibrium of the system by causing an imbalance in momentum and shifting the Fermi contours with respect to one another, resulting in a two-dimensional spin accumulation orthogonal to the current direction. Similarly, a spin current of a given spin polarization injected into the same system causes a spin imbalance and shifts the contours in the reverse manner, thus generating an orthogonal two-dimensional charge current manifesting the Inverse Rashba Edelstein Effect (IREE) as depicted in Figure 6.

Mathematically, the expression for spin-to-charge conversion due to the Inverse Rashba Edelstein Effect can be given as $j_s^{3D} \propto \lambda_{IREE}(\frac{2e}{\hbar})j_c^{2D} \times S$, in direct analog to the equation for ISHE, where a bulk spin current density j_s^{3D} injected into a Rashba interface is converted into a two-dimensional charge current density j_c^{2D} with a conversion efficiency provided by λ_{IREE}, the Rashba-Edelstein length (The factor $\frac{2e}{\hbar}$ converts units of spin current from J m^{-2} to A m^{-2}). The λ_{IREE} is comparable to the spin Hall angle θ_{SH}, except that it is dimensional with units of length due to the reduced dimensionality of the conversion process ($\lambda_{IREE} = \frac{j_c^{2D}}{j_s^{3D}}$, so the units do not cancel out as they do for θ_{SH}). This 'coherence length' can be related to a Rashba coefficient, α_R, by $\lambda_{IREE} = {}^{\alpha_R \tau_S}/_{\hbar}$, where τ_S is the relaxation time relating spin injection with spin-momentum scattering and ħ is the Planck constant over 2π. The Rashba coefficient, as with θ_{SH}, typically

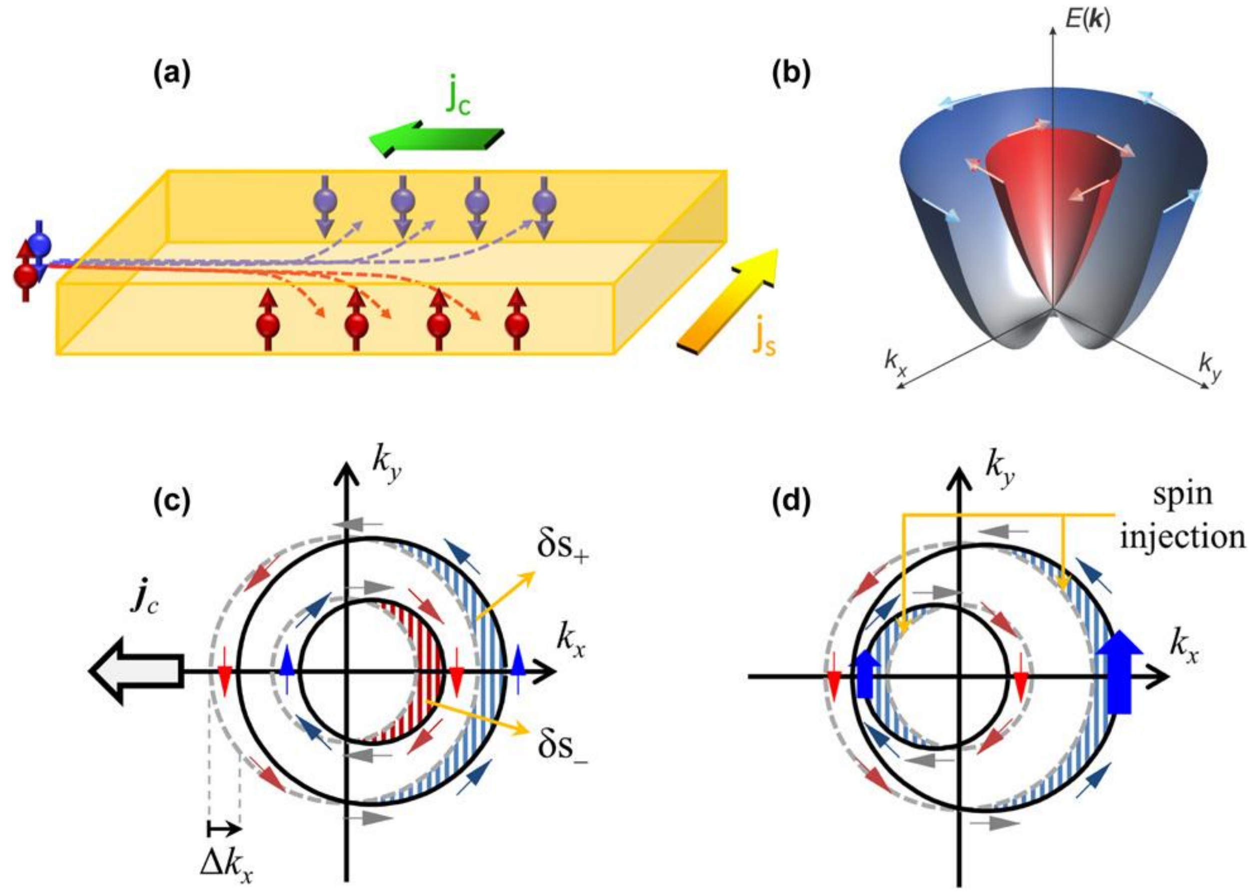

Figure 6. (a) Schematic illustration of the spin Hall effect. (b) Momentum-dependent spin split subbands plotted as red and blue parabolic lines. (c) Illustration of REE, where a charge current injected at the interface along –x induces a shift Δk_x of both Fermi contours resulting in spin accumulation polarized along the y-axis due to inequivalence of the two contours. (d) Illustration of IREE, where a spin current injected perpendicularly with spin polarization along the y-axis results in a net charge current generated orthogonally to the spin current injection and polarization directions. This figure is taken from Ref. [21].

increases with stronger spin-orbit coupling as is generally found in heavy elements such as Bi, Pb, and Pt.

While it is obvious that broken symmetry should occur at the surface of a material or interface of a heterostructure, it is also possible for a material system to possess *bulk* inversion asymmetry such as in many well-studied III-V uniaxial wurtzite compounds (e.g. GaAs, GaN, AlN, etc.), with similar modifications of their band structures related to spin-orbit effects. This bulk effect is referred to as the Dresselhaus effect [22], and may be present in conjunction with the Rashba effect, with their relative strengths depending on the specific material system. However, the result of this in terms of the orientation of the spin-momentum locked band structure for this more complicated case is not easily defined and will not be touched on further here.

1.3 Experimental Techniques to Generate Pure Spin Currents

This section will review two experimentally relevant techniques used for the generation of spin currents that allow for the probing of ISHE and IREE effects in various material systems. It is useful in a laboratory setting to study spin-to-charge conversion rather than charge-to-spin due to the difficulty of directly measuring spin accumulation, which typically requires ultra-sensitive optical methods such as Magneto-Optical Kerr Effect (MOKE) spectroscopy and a material with low spin-orbit coupling that allows for large spin diffusion lengths, whereas measuring charge currents in the form of a voltage is comparatively easy.

The first half of this section will detail a continuous-wave (cw) excitation method utilizing microwaves (typical frequencies on the order of ~1-20 GHz) to cause ferromagnetic resonance in a magnetic thin film adjacent to a non-magnetic spin-orbit coupling material in the presence of an external magnetic field. This technique is commonly referred to in the literature as 'spin pumping', and has been used to study spin injection into almost every class of material including metals [15], semiconductors [23], topological insulators [24], superconductors [25], etc.

The second half will discuss an ultrafast method where a pulsed femtosecond laser is used to cause ultrafast demagnetization in a magnetic thin film and subsequently generate an ultrafast, high-energy spin current that can travel into an adjacent spin-to-charge conversion material. This ultrafast regime leads to interesting and novel physics that cannot be accessed through traditional cw-excitation, and will be discussed here in the context of the spintronic emission of terahertz radiation.

1.3.1 Ferromagnetic Resonance and Spin Pumping

Ferromagnetic resonance (FMR) absorption was first discussed theoretically by Gans and Loyarte [26] and Dorfmann [27] in the early 1920's. However, a seminal theoretical paper written by Laundau and Lifshitz in 1935 laid the fundamental foundation from which the current understanding of FMR is derived, along with some later corrections by T. L. Gilbert [28]. The experimental discovery of FMR was made by Griffiths at the Clarendon Laboratory at Oxford in 1946, where he performed resonance absorption experiments on thin film samples of Fe, Co, and Ni as a function of microwave frequency with wavelengths on the order of 1-3 cm [29]. He found that the energy lost by a high frequency current flowing through a conductor was proportional to the product of the conductor's electrical resistivity and magnetic permeability, which could be used to determine its effective permeability at high frequency. In 1948, Charles Kittel synthesized the results of Griffiths' experiment and previous theoretical works to quantitatively describe the FMR process in terms of the precessional motion of magnetization in an applied magnetic field [30], [31]. Starting from the Larmor equation that connects resonance frequency and applied field, $\omega_0 = g\frac{e}{2mc}H$ (where ω_0 is the resonant frequency, g is the spectroscopic splitting factor of the electron spin, $\frac{e}{mc}$ is equivalent to the gyromagnetic ratio γ being the ratio of a particle's magnetic moment to its angular momentum, and H is the applied field) and combining it with the equation of motion of a magnetic moment under an applied field, $\frac{dJ}{dt} = M \times H$ (where J is the angular momentum per unit volume and M is the magnetization), Kittel derived the famous equation linking the resonant frequency of a ferromagnetic film to an external field as $f = \frac{\gamma}{2\pi}\sqrt{B(B + \mu_0 M)}$, where B is the resonant field, which is now referred to as the Kittel formula.

The precessional motion of the magnetization M in a solid material can be described by the differential Landau-Lifshitz-Gilbert (LLG) equation, represented pictorially in Figure 7, where in 1955 T. L. Gilbert through the work of his Ph.D. thesis improved upon the original model proposed by Landau and Lifshitz by adding a time dependent damping term η [28] and is fully expressed as:

$$\frac{dM}{dt} = -\gamma\left(M \times H_{eff} - \eta M \times \frac{dM}{dt}\right) \equiv -\gamma \mathrm{M(t)} \times H_{eff} + \frac{\alpha}{M_s} M(t) \times \frac{dM(t)}{dt}$$

where the first term in the expression describes the steady state precession of magnetization under an effective magnetic field and the second term describes the dissipative precessional damping where $\eta \equiv \alpha$ is the dimensionless Gilbert damping parameter.

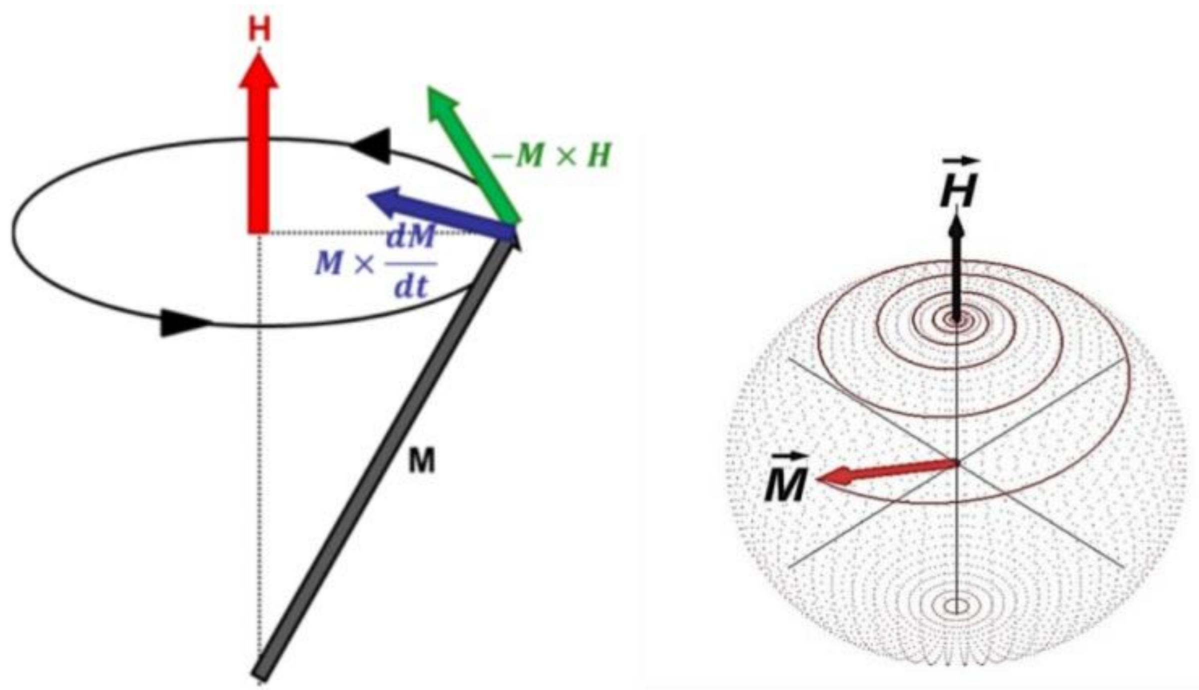

Figure 7. (Left) Precessional movement of magnetization M in response to rotational field H. (Right) Motion of M for a constant applied field H. This figure is taken from Ref. [32].

In a microscopic context, FMR can be described by the quantized absorption of a radiofrequency field by Zeeman split electron energy levels due to the presence of an external magnetic field. Microwave frequency electromagnetic radiation passing through a conductor, such as in the stripline of a coplanar waveguide, can be used to produce a high frequency magnetic field with energy $E = h\nu$. This *rf*-field may be absorbed by the Zeeman split energy levels of a ferromagnetic material when the quantized splitting of its energy levels due to the presence of an external field is exactly equal to the microwave energy, leading to microwave absorption and the perturbation of the material's equilibrium magnetization in the form of magnetization precession (i.e. ferromagnetic resonance), as shown in Figure 8. This microwave absorption possesses a Lorentzian line shape, and the addition of an *ac* magnetic field modulation to the external *dc* field will modify the intensity of microwave absorption as $\frac{dI}{dH}$ resulting in a Lorentzian-derivative line shape.

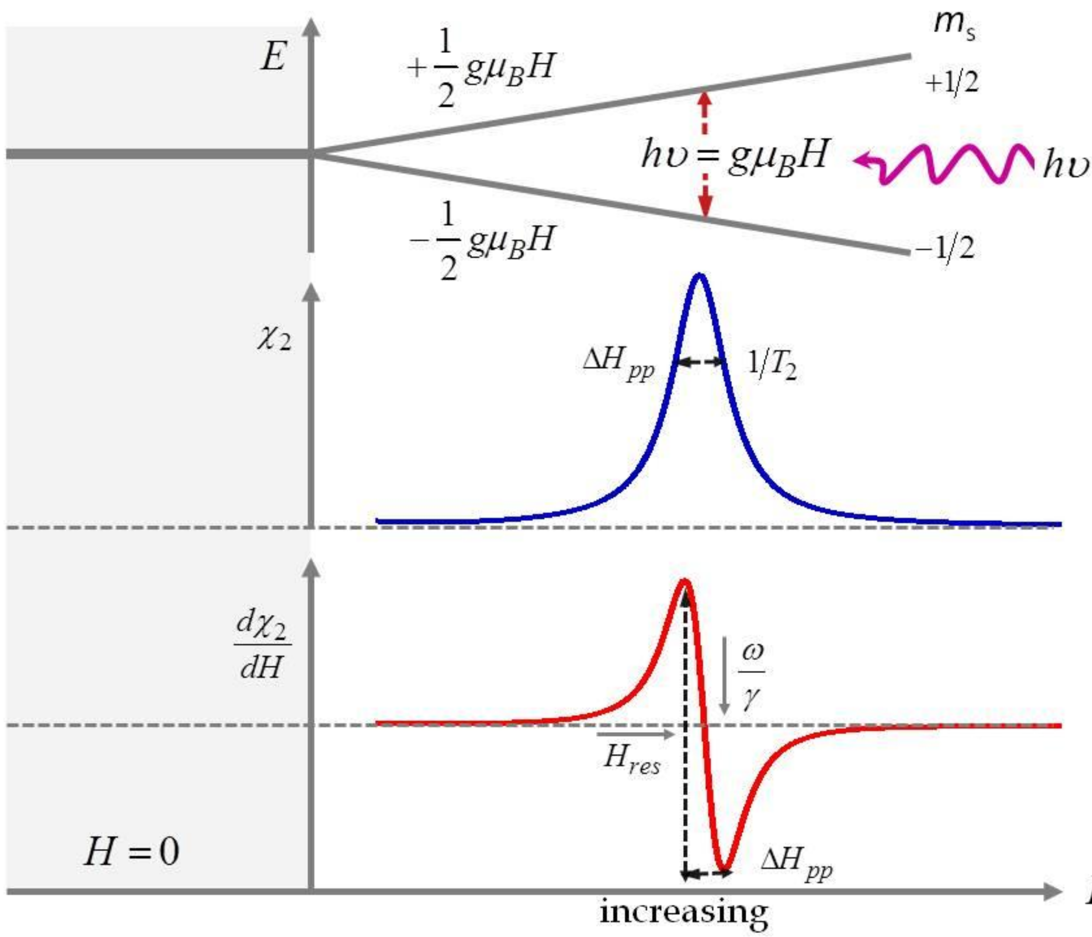

Figure 8. Zeeman splitting of energy levels and corresponding resonance absorption for a free electron as a function of applied field. Arbitrary units are used for the vertical and horizontal axes. This figure is taken from Ref. [33].

By fixing the microwave excitation at a constant frequency and sweeping the external magnetic field (or vice-versa), the resonant field can be determined and plotted as a function of frequency. Fitting of this relation to the Kittel equation in the form of $(\frac{2\pi f}{\gamma})^2 = H_R(H_R + 4\pi M_s)$, where H_R is the FMR resonant field, allows for determination of a ferromagnet's saturation magnetization ($4\pi M_s$) and gyromagnetic ratio (γ). Additionally, the linewidth of the FMR absorption peak may be similarly plotted versus frequency to allow for the extraction of the dimensionless Gilbert damping parameter as $\alpha = \frac{\sqrt{3}\gamma}{4\pi f}\Delta H + H_0$, where ΔH is the microwave absorption linewidth and H_0 is a frequency-independent linewidth contribution arising from inhomogeneities in the sample film.

Under the resonance condition, the magnetization precession in a ferromagnetic (FM) thin film generates a spin current that may be injected across an interface into an adjacent paramagnetic (PM) material in a process known as spin pumping. Here, the damping of magnetization precession induced by microwave excitation occurs in part due to the transfer of spin angular momentum from the local precession of spins in the ferromagnet to conduction electrons resulting in their polarization and the generation of a spin current that may then carry this angular momentum into an adjacent material and transfer it to that material's own conduction electrons. Once inside the paramagnetic material, the injected spin current may be converted into a transverse electromotive force inside the paramagnetic material by the ISHE and detected as a voltage [34]. This spin current emission and subsequent transfer of angular momentum also deprives the ferromagnet of magnetization, giving rise to an increase in the magnetization precession relaxation manifested by an increase in the Gilbert damping factor α.

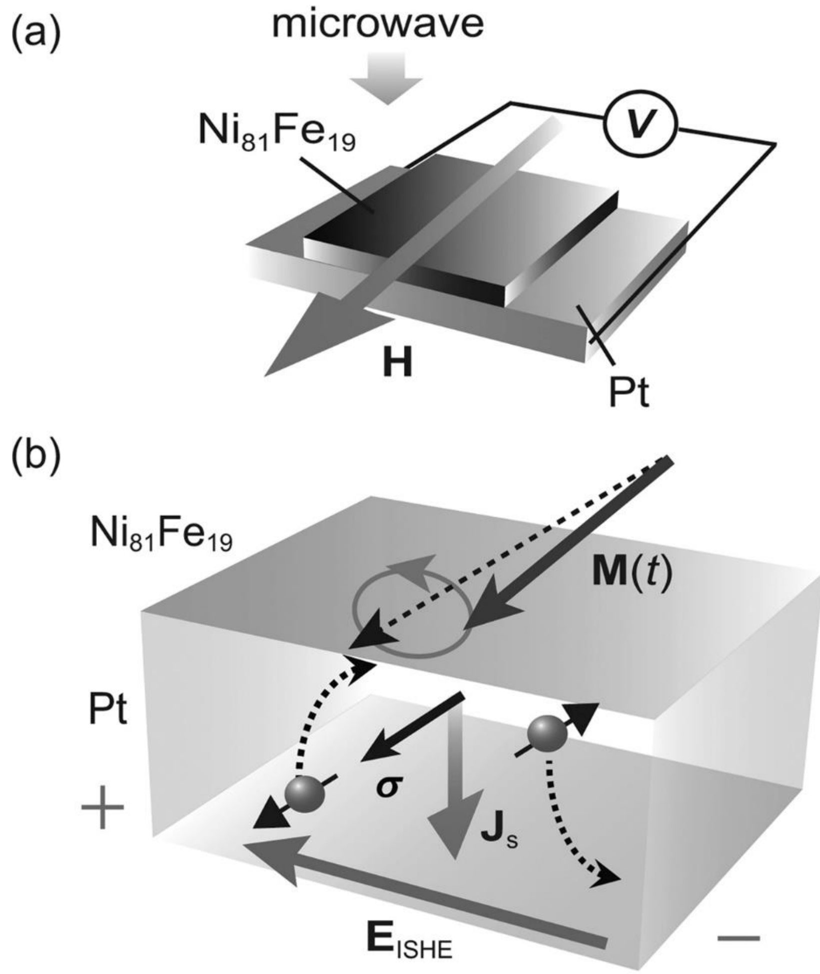

Figure 9. (a) Illustration of a $Ni_{81}Fe_{19}$/Pt bilayer device, where H is the external magnetic field. (b) Schematic depiction of spin pumping and the ISHE. M(t) is the magnetization of the ferromagnetic layer, E_{ISHE} is the electromotive force generated due to the ISHE, J_s is the diffusion direction of the spin current density, and σ is the spin polarization vector. This figure is taken from Ref. [15].

The spin current density created by spin pumping into a simple FM/PM bilayer system can be derived from the LLG equation and ultimately expressed as [15]:

$$j_s = \frac{g_r^{\uparrow\downarrow}\gamma^2 h^2 \hbar[4\pi M_s \gamma sin^2\theta_M + \sqrt{(4\pi M_s)^2\gamma^2 sin^4\theta_M + 4\omega^2}}{8\pi\alpha^2[(4\pi M_s)^2\gamma^2 sin^4\theta_M + 4\omega^2]}$$

where $g_r^{\uparrow\downarrow}$ is the real part of the spin mixing conductance - a parameter describing the efficiency of spin injection across the FM/PM interface, h is the microwave-generated *rf*-field, θ_M is the magnetization angle to the normal axis of the film plane, and $\omega = 2\pi f$ where f is the microwave frequency. Furthermore, understanding that the electric field produced by the ISHE has the relation $E_{ISHE} \propto j_s \times \sigma$, the voltage produced by this spin-to-charge conversion process will in turn be proportional to the spin current density and magnetization angle as $V_{ISHE} \propto j_s\ sin\theta_M$ resulting in the expression for the ISHE voltage as:

$$V_{ISHE} \propto \frac{g_r^{\uparrow\downarrow}\gamma^2 h^2 \hbar sin\theta_M [4\pi M_s \gamma sin^2\theta_M + \sqrt{(4\pi M_s)^2\gamma^2 sin^4\theta_M + 4\omega^2}}{8\pi\alpha^2[(4\pi M_s)^2\gamma^2 sin^4\theta_M + 4\omega^2]}$$

The spin current injected into the PM layer will undergo exponential decay as a result of spin relaxation, the magnitude of which is proportional to the material's spin-orbit coupling and spin diffusion length. Thus, the fractional spin current density present at any point in the PM layer is a function of the layer thickness. A coordinate system can be defined for the FM/PM bilayer where the FM magnetization is along the x-direction, the y-direction represents the orthogonal in-plane direction, and the spin current propagation is along the z-direction normal to the film plane. In this case, the spin current density present in the PM layer as a function of PM layer thickness can be expressed as:

$$j_s(z) = \frac{\sinh[\frac{d_N - z}{\lambda_N}]}{\sinh(\frac{d_N}{\lambda_N})} j_s^0$$

where d_N is the PM layer thickness, λ_N is the spin diffusion length of the PM material, and j_s^0 is the spin current density at the interface where z = 0. Previously, it was explained that the relation between charge and spin currents in the ISHE process is given by the relation $J_c = J_s\theta_{SH} \times \sigma$, which can be applied to the current coordinate system such that $j_c(z) = \theta_{SH}(\frac{2e}{\hbar}) j_s(z)$. The average charge current density generated during spin-to-charge conversion can be obtained by integrating over the thickness of the PM layer:

$$\langle j_c \rangle = \left(\frac{1}{d_N}\right) \int_0^{d_N} j_c(z) dz = \theta_{SH} \left(\frac{2e}{\hbar}\right) \frac{\lambda_N}{d_N} \tanh\left(\frac{d_N}{2\lambda_N}\right) j_s^0$$

Furthermore, if the bilayer system is assumed to operate based on an equivalent parallel circuit model, the relation between charge current and ISHE voltage is simply expressed as $V_{ISHE} = [R_F R_N/(R_F + R_N)] I_c = w[\sigma_N + (d_F/d_N)\sigma_F]^{-1} \langle j_c \rangle$, where R_F and R_N are the electrical resistance of the respective ferromagnetic and paramagnetic layers, I_c is the generated charge current, w is the width of the ferromagnet, σ_F and σ_N are the electrical conductivities of the ferromagnetic and paramagnetic layers, and d_F and d_N are the respective layer thicknesses. Combining this with the previous equation for average charge current density allows for the final relation between observed ISHE voltage and film thickness in the form of:

$$V_{ISHE} = \frac{w\theta_{SH}\lambda_N \tanh\left(\frac{d_N}{2\lambda_N}\right)}{d_N\sigma_N + d_F\sigma_F} \left(\frac{2e}{\hbar}\right) j_s^0$$

The importance of this mathematical determination is that it allows for the extraction of the spin Hall angle and spin diffusion length from measurements of the ISHE voltage as a function of PM film thickness using the spin pumping method. For example, in the prototypical system $Ni_{81}Fe_{19}$/Pt where the thickness of the Pt layer is systematically varied, the spin Hall angle of Pt in a spin pumping study by Ando et al. was found to be $\theta_{SH} = 0.04$, and the spin diffusion length $\lambda_N = 10\ nm$ [15]. This means that Pt is capable of converting an injected spin current into a corresponding charge current with an efficiency of about 4%, although it should be noted that this value varies significantly in the literature and is highly dependent on the material and interface properties and quality.

The spin diffusion length may be simply related to the spin relaxation time τ_s and spin diffusion constant D_s using the Einstein relation where $\lambda_N = \sqrt{D_s \tau_s}$ [14, 15]. Understanding the spin relaxation time in materials is critically important for device applications as it determines how long spin coherency, and thus information, may be retained. When the spin diffusion length is unknown and a thickness dependent study is not practical, it may also be useful to perform magnetic field angular dependent measurements of the ISHE voltage for its deduction in the PM material being studied using spin pumping. The basis for this measurement harkens back to the LLG equation described previously, where a magnetic field applied out-of-plane to the ferromagnetic thin film at an angle θ will result in a change of the angle of the magnetization-precession axis φ. In this situation, φ is not parallel to H due to the presence of a demagnetization field in the ferromagnetic layer. Since the spin polarization vector σ of an injected spin current during spin pumping is parallel to φ, the ISHE voltage measured with a constant transverse geometry will demonstrate an angular dependence where a maximum voltage will be obtained when $\theta = 0°$ and no voltage will be obtained when $\theta = 90°$ (i.e. the applied field is completely perpendicular to the film plane) as long as the spin lifetime in the material is comparable to or larger than the Larmor precession time.

The Larmor frequency of magnetization precession is given as $\omega_L = \gamma H_R$ (recalling that γ and H_R are the gyromagnetic ratio and resonant field, respectively) and the corresponding spin diffusion length at this frequency is $\lambda_\omega = \lambda_N / \sqrt{1 + i\omega_L \tau_s}$. The measured ISHE voltage is proportional to the applied magnetic field angle and now dependent on the spin relaxation time according to the expression [23]:

$$V_{ISHE} \propto j_s[cos\theta\cos(\theta - \varphi)\int_0^{d_N} e^{-z/\lambda_N} dz + sin\theta\sin(\theta - \varphi)\int_0^{d_N} Re\left[e^{-z/\lambda_\omega}\right] dz]$$

This method has been used for the determination of spin lifetime in p-type Si, as shown in Figure 10, finding that $\tau_s = 9\ ps$ which is significantly longer than that in the ferromagnetic $Ni_{81}Fe_{19}$ layer where $\tau_s = 9\ fs$. Later in this thesis, this methodology is applied to a single crystal hybrid perovskite semiconductor material ($MAPbBr_3/Ni_{81}Fe_{19}$) in order to observe a long spin lifetime of up to $\tau_s = 190\ ps$.

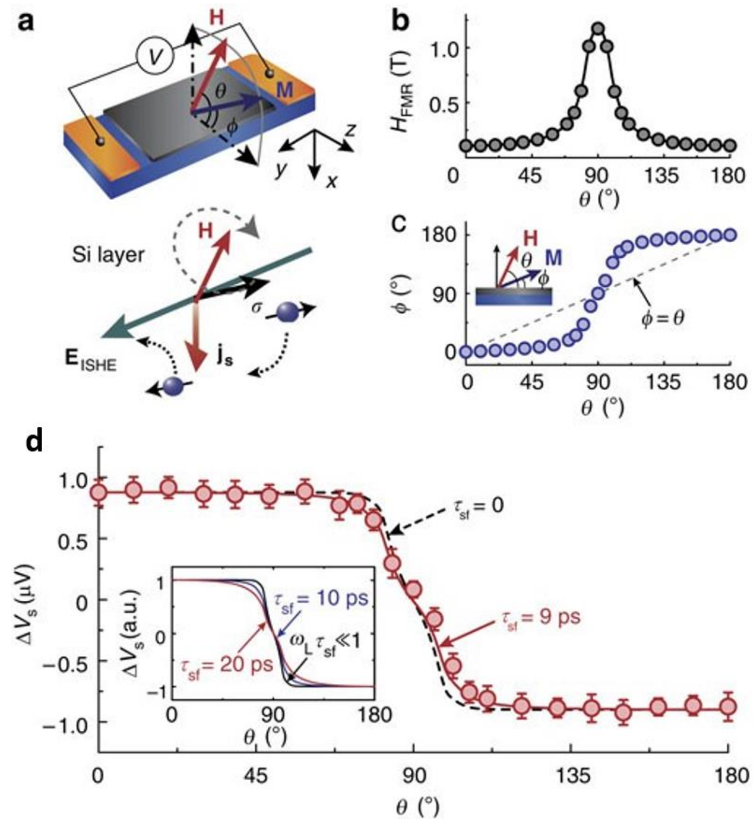

Figure 10. (a) Schematic illustration of $Ni_{81}Fe_{19}$/*p*-Si bilayer with external magnetic field H applied oblique to the film plane. M is the static component of the magnetization, θ is the magnetic field angle, and φ is the magnetization angle. (b) θ dependence of the resonant field H_{FMR}. (c) θ dependence of φ estimated using the LLG equation with measured values of H_{FMR}. (d) θ dependence of normalized ISHE voltage ΔV_s overlaid with theoretical curves for different spin relaxation times. This figure is taken from Ref. [23].

1.3.1 Ultrafast Demagnetization and Spin Current Generation

In 1996, E. Beaurepaire et al. revealed the first experimental demonstration of laser-induced demagnetization on ultrafast time scales where a ferromagnetic thin film of Ni was shown to rapidly demagnetize within 1-2 picoseconds of an incident 60 femtosecond 620 nm laser pulse [35]. This seminal work launched a flurry of subsequent experimental and theoretical efforts to understand and explain this phenomenon, which was surprising given the classical understanding of thermally and magnetically driven demagnetization that occurs on a nanosecond time scale. By 1999, J. Güdde et al. were already able to show that the process governing this ultrafast decay of magnetization in response to a fs laser pulse had an upper limit of 50 fs, which was still limited by their ability to generate shorter laser pulses [36]. Subsequent theoretical work by Zhang and Hübner provided the first comprehensive understanding of this effect whereby the laser-induced ultrafast demagnetization of a ferromagnetic metal occurs due to a cooperative effect of the external laser field and internal spin-orbit coupling of the material [37].

Advancements in the theory were proposed by M. Battiato et al. and A. Eschenlohr et al. describing the mechanism of ultrafast demagnetization in the superdiffusive regime [38], [39]. Here, absorption of photons from the incident femtosecond laser pulse by the metallic ferromagnet results in the spin-conserved excitation of electrons, primarily from the *d* band at the Fermi level to *s p*-like bands at higher energy, forming a non-equilibrium population of hot electrons. In the context of superdiffusive transport, not only do the excited electrons in *s p* bands have higher velocities (~ 1 nm/fs) but majority and minority spin carriers possess different relaxation times giving majority carriers a longer mean free path than minority ones. As the system evolves temporally this leads to a depletion of majority carriers and thus magnetization in the ferromagnetic film, which can be carried over into an adjacent material layer in the form of a superdiffusive spin current.

However, while the generation of non-equilibrium hot electrons by a ferromagnet's absorption of a fs laser pulse is agreed upon, whether or not the demagnetization can be explained by the superdiffusive model has been widely disputed in the literature. Studies presented by the group of David Cahill, among others, argue instead that this process can be understood entirely thermodynamically as a function of heat whereby differences in the temperatures between electrons, magnons, and phonons drive spin current generation and demagnetization [40]–[43].

Evidence for this thermally driven mechanism was provided by Choi et al. by using time-domain magneto-optical Kerr effect (TR-MOKE) to examine spin transfer torque (STT) effects at ultrafast time scales in a multilayer heterostructure consisting of Pt (30 nm) / FM1 / Cu (*h*) / FM2, where FM1 comprised a [Co/Pt] multilayer with perpendicular magnetization and FM2 consisted of a CoFeB layer with in-plane magnetization (see Figure 11) [40]. Given the extremely short inelastic mean free path of hot electrons in Pt (~5 nm), the 30 nm Pt layer is sufficiently thick to separate hot electrons generated from an incident fs laser pulse from the adjacent FM layer. Following laser excitation of the Pt, heat rapidly diffuses into the adjacent FM1 layer causing demagnetization and spin current generation due to electron-magnon coupling in conjunction with the transient differences in the temperatures of electron and magnon reservoirs. Since FM1 has a perpendicular magnetization, the generated spin current possesses a spin polarization perpendicular to the film plane as well. This spin current diffuses through the adjacent Cu layer, which has a relatively long spin diffusion length on the order of hundreds of

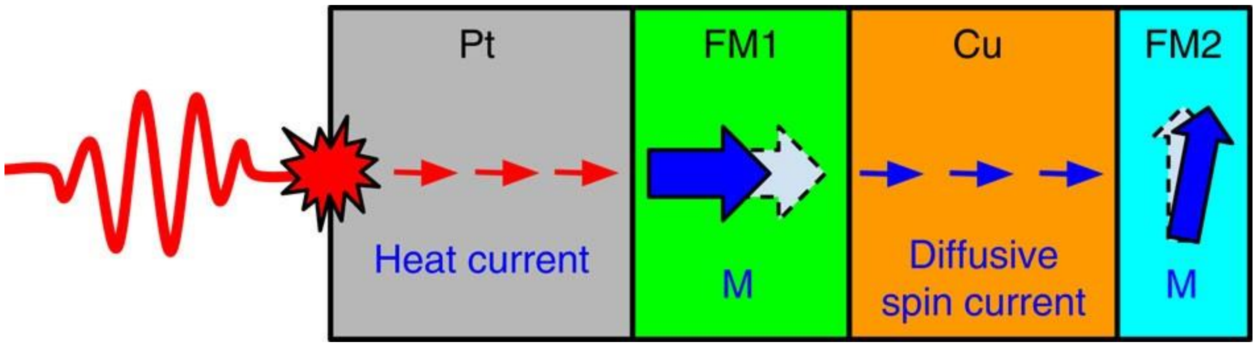

Figure 11. Multilayer heterostructure studied by Choi et al. A femtosecond pump laser incident on the Pt side generates and ultrafast temperature excursion. Thermal transport to the adjacent ferromagnetic layer drives demagnetization and subsequent generation of a diffusive spin current that leads to spin accumulation in the Cu layer. Spin transfer torque at the Cu/FM2 interface tilts the magnetization of FM2 out of plane and the magnetization of FM2 begins to precess. This figure is taken from Ref. [40].

nanometers due to its weak spin-orbit coupling, building up spin accumulation at the Cu/FM2 interface. This spin accumulation exerts a torque on the magnetization vector of FM2 due to the orthogonal relation of the spin polarization of the spin current and in-plane magnetization of FM2. The spin transfer torque results in transient precession of the FM2 layer, which is detected on an ultrafast time scale by the TR-MOKE. The results of this experimental study are consistent with diffusion based spin transport models, such as those described in previous sections of this thesis.

Regardless of the exact mechanism of spin current generation, it is clear that fs laser pulses can be used to create ultrafast bursts of spin current and raises the interesting prospect of how spin-to-charge conversion processes operate at this time scale. In 2013, T. Kampfrath et al. devised a scheme for the engineering and detection of ultrashort spin current bursts in metallic bilayer systems [44]. The authors in this study examined 10 nm thick Fe films capped by 2 nm of either Au or Ru, which they excited using fs laser pulses. As the ultrafast spin current bursts were injected into the heavy metal layer (Au or Ru), they were converted into a transient electric field by the ISHE. The resulting electromagnetic pulse generated by this spin-to-charge conversion process possessed a frequency in the terahertz range as detected through electrooptical sampling. Incredibly, this generated THz transient was ultra-broadband in nature, spanning from 0.3 – 4 THz in the case of Fe/Ru and 0.3 – >20 THz in the case of Fe/Au. The broader frequency emission from the Au-capped sample was attributed to much faster dynamics in Au as compared with Ru. Reversal of the magnetization direction of the Fe layer by reversing the direction of an applied external magnetic field resulted in phase-reversal of the emitted THz waveform. Not only did this provide critical evidence that the ISHE was responsible for the observed behavior, but it also showed that THz emission could be tuned via an external field – a key spintronic functionality. This seminal work opened the door to the study and design of spintronic THz emitters, with possible applications for wireless communications, ultrafast computing, and non-destructive examination. Additionally, it created a new avenue for the fundamental investigation of spin dynamics at ultrafast time scales in solid state materials.

Chapter 2

Experimental Methods

This chapter will briefly cover the experimental methods used to fabricate and characterize the spintronics devices described in this dissertation.

2.1 Sample Fabrication

Spintronics devices are typically comprised of thin films that may be created through various vacuum deposition methods. In the present work, physical vapor deposition was used for the thermal evaporation of ferromagnetic, metallic, and oxide films using electron beam evaporation and radiofrequency sputtering techniques. The substrate used for the deposition process consists of either an inert, rigid medium (i.e. glass, sapphire substrates, etc.) or an active material that serves a primary function in the ultimate device (i.e. semiconductor thin films or single crystals).

2.1.1 Physical Vapor Deposition

Physical vapor deposition describes a variety of processes that allow for the atomistic deposition of materials onto a suitable substrate in a vacuum environment. These processes involve the vaporization of a material from its solid or liquid form, and subsequent transportation of that gaseous matter along its mean free path. Vaporized material will condense onto a substrate in its path and form a thin film with thicknesses ranging from nanometers to micrometers. The rate of deposition here is typically on the order of 0.1 – 10 nanometers per second. A vacuum environment with pressures on the order of 10^{-5} – 10^{-9} Torr is utilized in order to reduce scattering of the vapor material from ambient gas molecules or atoms, thus increasing its mean free path [45].

Figure 12. Sun Lab glove box deposition system at NC State University. (Left) Front side of the instrument with N_2 filled glove box for handling air-sensitive samples. (Middle) Rear view of dual deposition chambers connected by a central load lock. (Right) Interior view of deposition chamber showing deposition sources, quartz crystal microbalance sensors, and samples stages with heating and cooling capabilities.

The Sun Lab at NC State University possesses a glovebox-integrated physical vapor vacuum deposition system with the capability of depositing a variety of metallic, organic, and ceramic materials in a controlled, inert environment (see Figure 12). The glovebox integration is particularly advantageous when working with materials that are sensitive to oxygen and humidity in ambient conditions. Two primary methods used for depositing thin films in this system are e-beam evaporation and *rf* sputtering, which are briefly detailed below.

2.1.2 Electron Beam Evaporation

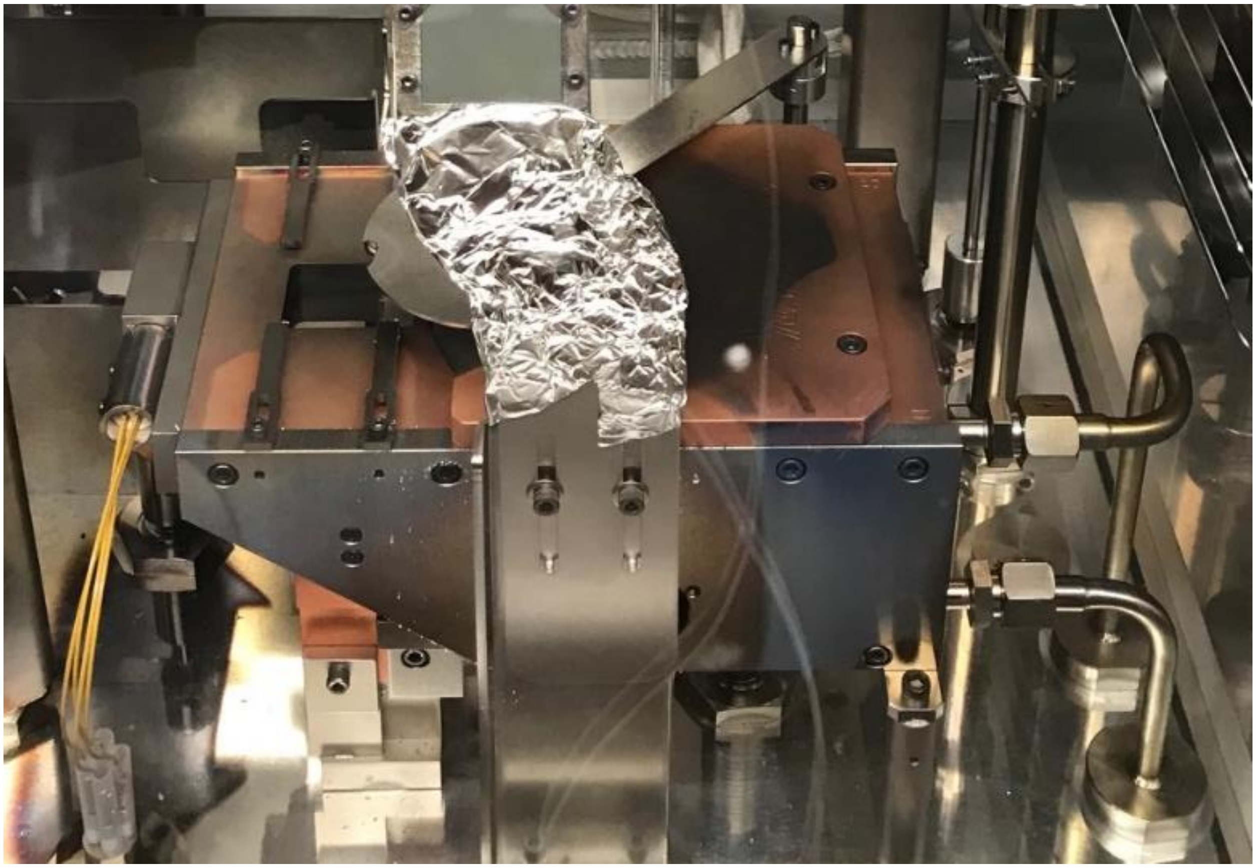

Figure 13. Electron beam evaporator used for deposition of ferromagnetic thin films, metallic electrodes, and oxide insulating and/or capping layers.

Electron beam, or e-beam, evaporation is a method for transferring energy from a beam of electrons into a target material causing it to evaporate or sublimate and then deposit onto a corresponding substrate. The electron beam is generated by passing electric current through a tungsten filament, resulting in resistive heating and thermal emission of electrons. A high voltage applied between the filament and target material directs the emitted electrons towards the target. Strong magnetic fields are used to both focus the electron beam and control its path such that it impacts the bulk of the material being evaporated. As the material absorbs energy from the incident electrons it is heated and either directly sublimates or melts into a liquid before evaporating. This deposition method may be used to evaporate an incredibly large library of materials ranging from refractory metals to ceramic oxides, that would be otherwise inaccessible to conventional resistive thermal evaporation.

2.1.3 RF Sputtering

Figure 14. An RF sputtering source is pictured in the bottom of the image. An adjacent QCM sensor is used for monitoring film thickness during deposition. A substrate shutter between the source and sample stage allows or prevents incoming vapor phase material hitting the substrate.

Sputtering is a physical, non-thermal vaporization process by which atoms are ejected from the surface of a target material due to the transfer of kinetic energy from bombarding, energetic ions accelerated from a nearby plasma. While reactive sputtering using a working gas such as oxygen or nitrogen is sometimes used in the deposition of certain materials, typically an inert, heavy gas such as argon is used for the plasma source. A plasma is sustained by the breakdown and ionization of this gas through the application of a strong bias voltage, as in the case of *dc* sputtering, or an alternating electric potential, as used in *rf* sputtering. This plasma is usually confined close to the target material being sputtered, which in turn is negatively charged and acts as a cathode. Positively charged argon ions bombard the negatively charged target material transferring their momentum to surface atoms in the target. A fine spray of atoms are subsequently emitted from the target which may travel through the vacuum chamber along their line-of-sight before condensing on a substrate.

The main advantage of *rf* sputtering over *dc* is that traditional *dc* sputtering can only be performed on electrically conductive materials, like metals, whereas *rf* sputtering can be performed on a wide variety of materials including semiconductors and dielectrics such as aluminum oxide, silicon oxide, etc. The reason for this is that dielectric materials accumulate charge on their surfaces and over time the buildup of positively charged ions at a dielectric surface can prevent the mechanism of action for sputtering to occur. By applying a radiofrequency alternating potential, the surface of the target material is effectively cleaned of accumulated ions at the end of each full cycle. The addition of an impedance analyzing network allows for automatic matching of the circuit impedance to a 50 Ohm load, thus providing optimal power transfer from the generator to the plasma chamber. The main drawback of this method is that deposition rates for metals are less than what can be achieved in a classic *dc* sputtering system.

3.1 Spin Pumping Measurements

Spin pumping measurements including FMR and ISHE are integral to understanding material properties in spintronics devices such as the spin Hall angle and spin diffusion length. Typically, a sample is mounted on a coplanar waveguide such that the ferromagnetic layer is close to the microwave field source emanating from the central conductor, although direct contact should be avoided to prevent possible short circuiting. Low temperature measurements are crucial for examining material systems that exhibit phase transitions below room temperature as it relates to magnetic ordering, superconductivity, structural ordering, etc. The Sun Lab at NC State possesses the technical capabilities to perform spin pumping measurements at room temperature in an open-air electromagnet, and from 1.8 – 300K in either a physical property measurement system or custom superconducting vector magnet.

3.1.1 Room Temperature Electromagnet

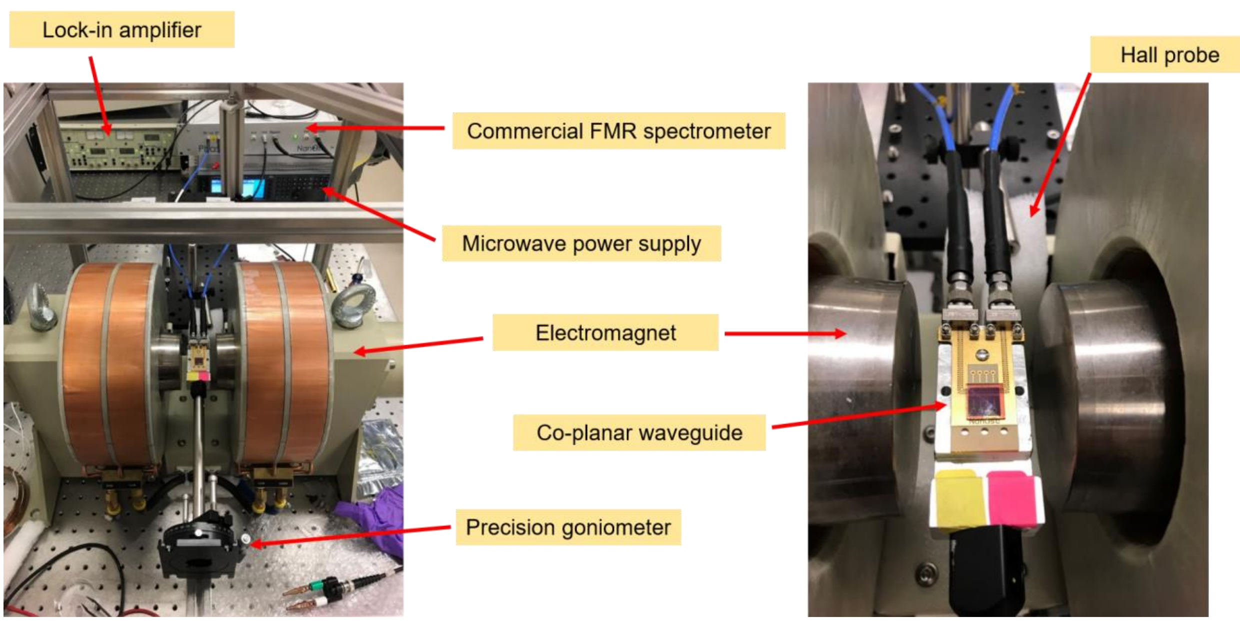

Figure 15. Experimental setup for measuring FMR and ISHE at room temperature using a benchtop electromagnet.

Room temperature spin pumping measurements in ambient conditions are done using the experimental setup pictured above in Figure X. A *dc* magnetic field is applied using a benchtop electromagnet, and the field angle with respect to the sample may be varied using a precision goniometer. The coplanar waveguide used here is composed of Au with a thickness of 44 μm. The central conductor has a width of 200 μm, with 150 μm ground spacings on either side. SMA cables connect the microwave source to the waveguide and allow for the transmission of microwave radiation. For FMR, a commercial spectrometer from NanOsc is used to measure microwave absorption in conjunction with their proprietary measurement software through a computer interface. For ISHE, a Keysight X-Series microwave signal generator is used to supply modulated microwave excitation while the voltage generated from the spin-to-charge conversion process is measured via a lock-in amplifier. A custom LabView program is used to read the voltage output and control the magnetic field.

3.1.2 Physical Property Measurement System

Figure 16. Quantum Design Physical Property Measurement System (PPMS) used for electronic and magnetic characterization from 2 K to 300 K.

Low temperature spin pumping measurements may be performed for both in-plane and out-of-plane directions using a Quantum Design Physical Property Measurement System (PPMS) and variable temperature FMR probe from NanOsc. The QD PPMS can be used to apply a magnetic field of up to 9 T and its cryostat can access temperatures ranging from 1.8 K to 300 K. The in-plane and out-of-plane coplanar waveguides allow for measurements of magnetic systems with planar or perpendicular magnetizations. The commercial NanOsc FMR spectrometer is used with this system to perform FMR measurements.

3.1.3 Superconducting Vector Magnet

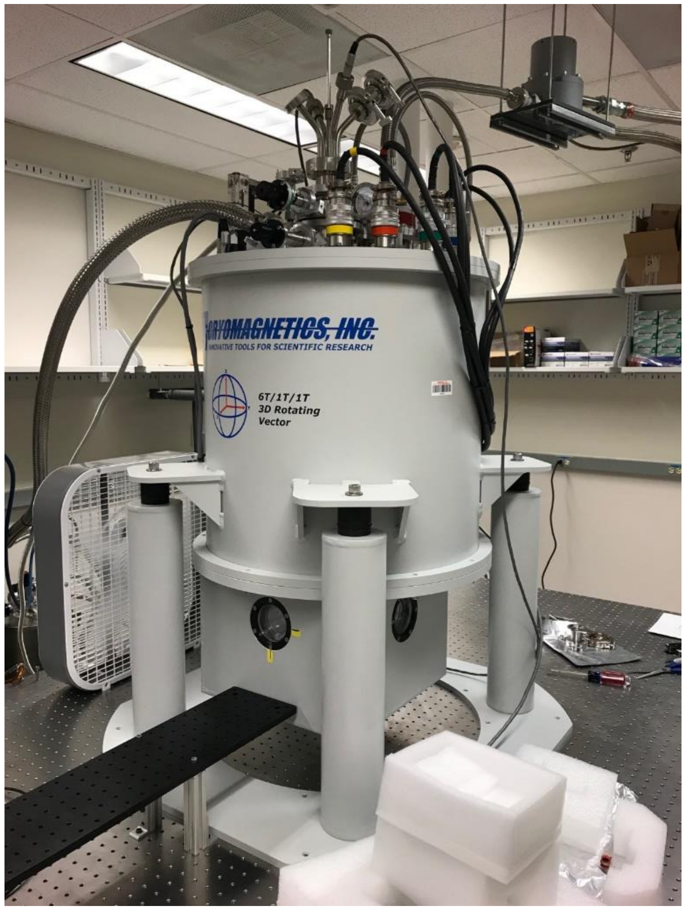

Figure 17. Superconducting vector magnet for magnetic, electronic, and optical characterization at cryogenic temperatures. A magnetic field of up to 1 T can be applied in three dimensions.

The Sun Lab is also equipped with a three-dimensional superconducting vector magnet made by Cryomagnetics, Inc. that can be used to apply a magnetic field in any arbitrary direction allowing for angular dependent spin pumping measurements. The maximum field limit for this instrument is 6 T in the Z-direction and 1 T in the X and Y directions. A custom probe contains both electrical and microwave connections enabling ISHE measurements.

Chapter 3

Semiconductor Spintronics

The integration of semiconductor materials into spintronic devices holds great promise for future devices and applications. Unlike their metallic counterparts, semiconductor material properties can be tuned in order to produce novel functionalities through mechanisms such as doping, electronic or optical gating, and band structure engineering, to name a few. This additional level of control creates the possibility for advanced device designs and exciting spintronics opportunities.

This chapter will discuss organic, inorganic, and hybrid semiconductor materials in the context of spintronics. The first sections will focus on spin transport and spin-orbit coupling in organic semiconductors, and include a publication discussing the effects of structural conformation on these properties. The following sections will detail spin transport and dynamics in inorganic semiconductors and include a manuscript examining the effects of carrier concentration on spintronic THz emission in NiFe/*n*-GaN bilayers. Finally, the last part of this chapter will discuss a promising class of hybrid organic-inorganic perovskite materials and contain a study on spin relaxation times in a single crystal of the prototypical $MAPbBr_3$.

3.1 Organic Semiconductor Spintronics

Organic semiconductors (OSCs) may possess many desirable traits for spintronics applications such as long spin relaxation times [46], [47], efficient spin injection [48]–[50], facile preparation methods [51], [52], mechanical flexibility [53], and a high degree of customizability through molecular and chemical modification.

Generally, organic semiconductors are primarily composed of light elements, such as carbon, hydrogen, nitrogen, and oxygen, and thus typically exhibit very weak spin-orbit coupling, large spin diffusion lengths, and weak to moderate hyperfine interaction (as a rule of thumb, SOC $\propto Z^4$ where Z is the effective atomic number [54], [55]). These properties make them interesting candidates for spin transport applications in the field of spintronics, where spin coherence may be retained over macroscopic length scales and for long periods of time. That being said, there are still many outstanding issues when it comes to device functionality and fabrication with these materials. Carrier mobilities are substantially lower in organic semiconductors (~10^{-8} – 10^{-2} cm^2/Vs) as compared with common inorganic semiconductors such as Si, Ge, or GaAs (~10^2 – 10^3 cm^2/Vs). Depending on the OSC thickness, operating temperature, and doping profile, conduction may occur either via direct tunneling, multistep tunneling, hopping via localized states, or even band-like conduction [56]. Additionally, while some of the beneficial characteristics of OSCs include their mechanical softness, flexibility, and solution processability, these same boons can present significant problems and challenges for device fabrication. Many of the standard semiconductor processing methods use strong organic solvents for lithographic and cleaning steps that are deleterious to and incompatible with OSCs. The surface profile of these organic materials may be much rougher than in inorganic semiconductors since their solid state comprises a disordered arrangement of polymeric units as opposed to close packed atoms with well-defined crystallographic planes. The ferromagnet/organic interface presents both challenges and opportunities for engineering OSC spintronics, as spin injection is highly sensitive to the hybridized bonding environment between the metallic ferromagnet and highest occupied molecular orbital (HOMO) or lowest unoccupied molecular orbital (LUMO) of the molecular material. Metal-organic bonds can modify the electronic configuration at the interface and induce strong modifications of the local spin-dependent electronic properties (e.g. spin filtering). The formation of this spin-dependent hybrid metal-organic interface is often termed the ‘spinterface’ in spintronics literature, and can be useful for controlling or enhancing spin injection into OSC-based devices [57], [58].

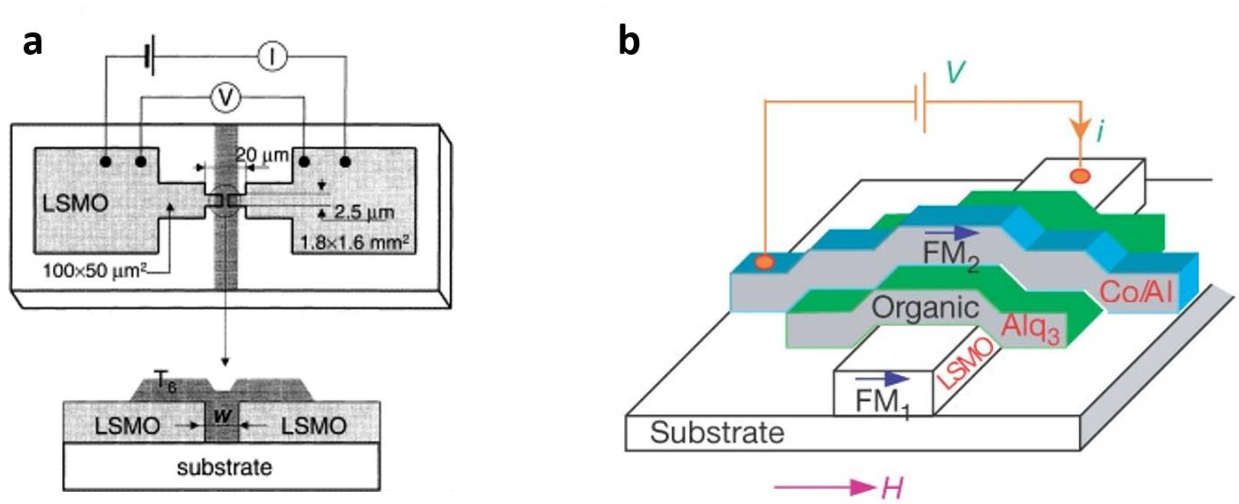

Figure 18. (a) Lateral organic spin valve used in the seminal observation of organic magnetoresistance in sexithienyl. Figure is taken from Ref. [59]. (b) Vertical spin valve used for measuring MR in an Alq_3 film. Figure is taken from Ref. [60].

The origin of organic semiconductors in spintronics can be traced to the discovery of giant organic magnetoresistance (OMAR) and spin polarized injection in sexithienyl (T_6), a prototypical π-conjugated molecule, by Dediu et al. in 2002 using a lateral spin valve configuration comprised of $La_{0.67}Sr_{0.33}MnO_3$ (LSMO) / T_6 / LSMO [59]. The authors in this study observed strong magnetoresistance of up to 30% at room temperature in ambient conditions and extracted a spin diffusion length of approximately 200 nm, indicating the promise of OSCs for spintronics applications and initiating a flurry of research activity in this area. Two years later, in 2004, Z. Xiong et al. investigated the small π-conjugated molecule 8-hydroxyquinoline aluminum (Alq_3), most commonly found in organic light-emitting diodes, using a vertical spin valve device structure to investigate spin injection and transport in this system as a function of temperature [60]. Here, the Alq_3 served as a spacer layer between a bottom ferromagnetic electrode of $La_{0.67}Sr_{0.33}MnO_3$ (LSMO) and top ferromagnetic layer of Co. Their report demonstrated significant spin-polarized carrier injection and a sizeable magnetoresistance of up to 40% at 11 K. Since these seminal studies were published, a great deal of research effort has been invested into understanding spin transport properties in organic spin valve and magnetic tunnel junction devices. However, issues related to spurious effects from electronic measurements and sample preparation have caused some confusion and conflicting results in the literature [61]. In order to circumvent these challenges, some studies have sought to utilize the spin pumping technique to examine organic semiconductors through the lens of pure spin currents, which are not subject to impedance mismatch problems commonly observed in electronic measurements.

In the first report of its kind, K. Ando et al. used spin pumping to investigate spin-to-charge conversion in the organic semiconductor PEDOT:PSS, a highly conductive conjugated polymer consisting of a mixture of polystyrene sulfonate (PSS) and poly(3,4-ethylenedioxythiophene) (PEDOT) [62]. The authors devised a bilayer structure consisting of $Y_3Fe_5O_{12}$ (YIG) / PEDOT:PSS, where the ferromagnetic insulator YIG was used in place of a typical metallic ferromagnet in order to reduce spurious spin rectification signals such as anisotropic magnetoresistance, anomalous Hall effect, spin backflow, or current shunting. FMR and ISHE experiments conducted with this system revealed a small, but detectable, spin-to-charge conversion occurring within the organic layer. The extracted spin Hall angle was determined to be $\theta_{SH} \approx 10^{-7}$, almost 6 orders of magnitude smaller than what is typically seen in a heavy metal such as Pt, and the spin diffusion length was approximately $\lambda_N = 22 - 31\ nm$ yielding a long spin relaxation time of $\tau_s = 5 - 11\ \mu s$ through the Einstein relation. These results showed that despite the weak spin-orbit coupling in organic systems, significant spin accumulation can be obtained aided by long spin lifetimes and thus OSCs may be eminently suitable for spintronics applications. Furthermore, while the overall spin Hall angle was remarkably low, a nuanced analysis of the results showed that this was in part due to a large conductivity anisotropy in the PEDOT:PSS system whereby spin injection was hampered by being present along the low mobility direction while the transverse charge current was generated along the high mobility direction. Accounting for this anisotropy factor provided a conversion efficiency comparable to that in Pt despite the weak SOC. This caveat in the understanding of spin-to-charge conversion in this particular organic system is representative of the broader challenges in organic spintronics, where the complex nature of disordered organic solids and their carrier transport properties makes it difficult to pin down an exact understanding of spin-dependent processes within them.

3.1.1 Spin Transport and Spin-Orbit Coupling in Organic Semiconductors

Spin transport in organic semiconductors is highly dependent on their carrier conduction mechanism. In conjugated polymers, charge carriers are typically present in the form of polarons due to the strong coupling of electrons and phonons, and they move through the material via hopping between localized states [63]. These spin-1/2 polarons may undergo spin relaxation via spin-flips from spin scattering centers promoted predominately by spin-orbit coupling or hyperfine interaction. In highly doped polymeric systems, where polaron concentrations are in excess of $10^{16} – 10^{17}$ cm^{-3}, an exchange-mediated spin diffusion regime may be accessed wherein exchange coupled spins on adjacent hopping sites may transmit angular momentum without requiring the physical movement of charges. Organic semiconductors characterized by such high spin densities correspondingly exhibit spin diffusion lengths one or more orders of magnitude higher than in those where exchange coupling is negligible [64].

While spin diffusion as it relates especially to spin-orbit coupling is relatively well understood in inorganic solids, in organic solids molecules and polymers are disordered and can possess different structural and conformational characteristics compared with their isolated forms. SOC in this type of system where molecular orbitals depend on a variety of factors, for example the torsion angle along a conjugated polymer's backbone, warrants unique scrutiny. As proposed theoretically by Z. G. Yu in 2011 [65], the spin diffusion length in an organic semiconductor may be expressed rather simply by the polaron hopping distance $\bar{R}$ normalized by a spin admixture parameter γ in the form of: $\lambda_s = \frac{\bar{R}}{4\gamma}$. The spin admixture parameter provides a measure of the organic system's spin-orbit coupling strength and is in turn dependent on conformational characteristics. Examination of a simple biphenyl molecule, for example, found that the introduction of torsion along the conjugated backbone increased the effective SOC by orders of magnitude as the respective phenyl rings and their π systems deviated from planarity and neared orthogonality. Additionally, an experimentally useful method for distinguishing the origins of spin relaxation between SOC and hyperfine interaction (HFI) was proposed through temperature dependent analysis of the spin diffusion length and spin diffusion constant, where spin relaxation time and diffusion length should be linear with D and increase rapidly with temperature if HFI is the dominant relaxation mechanism. A decrease in spin diffusion length as a function of temperature is indicative of SOC-dominated spin relaxation and can be thought of in the context of polaron hopping whereby the polaron hopping distance $\bar{R}$ is enhanced at low temperatures, where variable-range hopping is enabled, and reduced at high temperatures where hopping is confined to nearest neighbor sites. This hopping based theoretical model has been supported experimentally [66]–[68], and aids in the understanding of spin transport in organic semiconductors.

3.1.2 Conformational Effects on Spin Pumping in Organic Semiconductors

This section is adapted from published work in Ref. [68]. Additional information including supplementary materials may be found through this reference.

Tuning of Spin-Orbit Coupling in Metal-Free Conjugated Polymers by Structural Conformation

Eric Vetter[1,3], Ian VonWald[2], Shijia Yang[1], Liang Yan[2], Sanaz Koohfar[1], Divine Kumah[1], Zhi-Gang Yu[4,5], Wei You[2,6*], Dali Sun[1,6*]

[1] *Department of Physics, North Carolina State University, Raleigh, NC 27695 USA*

[2] *Department of Chemistry, University of North Carolina at Chapel Hill, Chapel Hill, NC 27599 USA*

[3] *Department of Material Science and Engineering, North Carolina State University, Raleigh, NC 27695 USA*

[4] *ISP/Applied Sciences laboratory, Washington State University, Spokane, WA 99202 USA*

[5] *Department of Physics and Astronomy, Washington State University, Pullman, WA 99164 USA*

[6] *Organic and Carbon Electronics Lab (ORaCEL), North Carolina State University, Raleigh, NC27695, USA*

Abstract

Manipulating spin-orbit coupling (SOC) is a key achievement for spin-orbitronic applications since SOC determines spin diffusion lengths and spin-to-charge conversion efficiencies. While in most organic semiconductors SOC is inherently very weak due to being composed of primarily light elements, the SOC in conjugated polymer systems is also intimately tied to the polymer's structural conformation and thus may be manipulated. Here we report a modification of SOC in conjugated polymers by altering torsion angle between conjugated units. Spin pumping experiments are performed on three poly(3-alkylthiophene) polymer films with

decreasing conjugation lengths and concomitantly increasing torsion angle. The more twisted polymer exhibits a shorter spin diffusion length and a giant spin mixing conductance (up to 10^{21} m^{-2}), which is attributed to an increased SOC by structural conformation. This work offers a new route for enhancing SOC and spin injection efficiency in organic materials for spintronic applications.

*Corresponding author: wyou@unc.edu, dsun4@ncsu.edu

I. INTRODUCTION

Spintronics embodies the concept of utilizing both the spin and charge degrees of freedom of carriers for new devices and applications, whose functions cannot be easily achieved in conventional electronic devices [69]. The recent emergence of novel spintronic studies focuses on the generation, transmission, and control of a 'pure spin current' by means of the spin-orbit coupling (SOC) in the material, which enables the conversion of a pure spin current into a charge current or vice versa [70]. This process has initiated a myriad of SOC-based spintronic applications, e.g., spin-to-charge convertors and spin-orbit torque devices, in a variety of materials including heavy-metals [71], two-dimensional electron gases [72], topological insulators [73], and inorganic semiconductors [23]. Tailoring SOC is typically achieved via heavy-metal doping [74], [75] and is integral to novel Rashba splitting states [76] and topological phases [77].

In order to measure SOC in a wide variety of materials, the spin pumping technique has emerged as a high fidelity method for determining SOC-dependent parameters such as the spin Hall angle and spin diffusion length [78]. Here, microwave excitation is used to drive ferromagnetic resonance (FMR) in a ferromagnetic thin film in the presence of an applied magnetic field, generating a pure spin current in an adjacent material with indeterminate SOC. Additionally, the spin current injected into this SOC material may be converted into a corresponding charge current via the inverse spin Hall effect (ISHE), with the conversion efficiency encapsulated by the spin Hall angle (θ_{SH}). Parametric studies utilizing both FMR and ISHE as a function of the SOC material's thickness allow for the direct determination of spin diffusion lengths and spin-to-charge conversion efficiencies, which ultimately relate back to the strength of SOC. This has been well established in a multitude of inorganic materials systems, including both metals and semiconductors [15], [23].

Recently, the spin pumping technique and its usefulness in determining the magnitude of SOC has also been applied to organic systems. Given that organic materials have on average a very low atomic number (Z) owing to the predominance of carbon and hydrogen, and that $\theta_{SH} \propto$ SOC $\propto Z^4$, it might be expected that SOC is generally very weak in organics with concomitantly low spin Hall angles. Indeed, this is borne out by fruitful spin pumping experiments in organic systems such as PBTTT [63], doped PEDOT:PSS [51], and polyaniline [79], where spin Hall angles are orders of magnitude lower than those in strong SOC heavy metals and spin diffusion lengths are accordingly orders of magnitude higher. The long spin diffusion lengths and spin lifetimes in organic materials generally makes them ideal candidates for spin transport materials. However, not all organic materials follow this trend, with some materials like C_{60} [80] and Alq_3 [81], exhibiting surprisingly high SOC on par with that in heavy metal systems.

Remarkably, there are differences in the nature of SOC in organic solids as compared to inorganic solids. SOC, by definition, enables the transfer of angular momenta between orbitals and spins, and in organic solids the molecular orbitals are strongly influenced by the materials' structural conformation. Theoretical models for SOC in these cases have been established where a large SOC may be obtained in conjugated organic systems when π orbitals are misaligned [65], [82]. This model can be used to explain the aforementioned discrepancies in SOC strength in Alq_3 molecules, where its three conjugated ligands are orthogonally arranged [82], and C_{60}, where the curvature of its spherical geometry prevents parallel alignment of the π orbitals [83], [84]. Since its recent inception, this model has also been supported experimentally through spin pumping experiments in conjugated polymers with varying degrees of planarity [63], [67], [85].

In this work, we experimentally verify that a tailored SOC can be achieved in conjugated polymers through structural conformation by varying the degree of torsion between conjugated units along the polymer backbone of polyalkylthiophenes. The strength of SOC in the 'twisted' conjugated polymer is probed by measuring the spin diffusion length and the effective spin mixing conductance in a $Ni_{81}Fe_{19}$/polymer/ITO trilayer heterostructure using a spin pumping approach, wherein the organic polymer constitutes either a grafted poly(3-methylthiophene) conjugated polymer brush (P3MT, 'twisted' case) or spin-coated poly(3-hexylthiophene) film (P3HT, 'planar' case; either regioregular (RRe-P3HT) or regiorandom (RRa-P3HT), defined by the side chain arrangement). The RRa-P3HT possesses a more twisted conformation than the RRe-P3HT, with planarization frustrated by the steric hindrance of the randomized side chains. Through a comparative study of ferromagnetic resonance (FMR) and inverse spin Hall effect (ISHE) measurements between these three types of polymers at room temperature as a function of polymer thickness, we find that P3MT exhibits a consistently higher spin mixing conductance and shorter spin diffusion length than that in P3HT, despite the similarities in their chemical structure and electronic properties. These differences are attributed to a stronger effective SOC in

P3MT as a result of the polymer's structural conformation, supported by recent theoretical treatments of SOC and its effects in disordered organic semiconductors [65], [82]. Remarkably, we observe a record high spin mixing conductance (up to 10^{21} m^{-2}) at the NiFe/P3MT interface that is two orders of magnitude higher than that in conventional inorganic bilayer heterostructures (in the range of 10^{18} to 10^{19} m^{-2}), suggesting a very efficient spin injection at the ferromagnet/polymer interface.

II. EXPERIMENTAL DETAILS

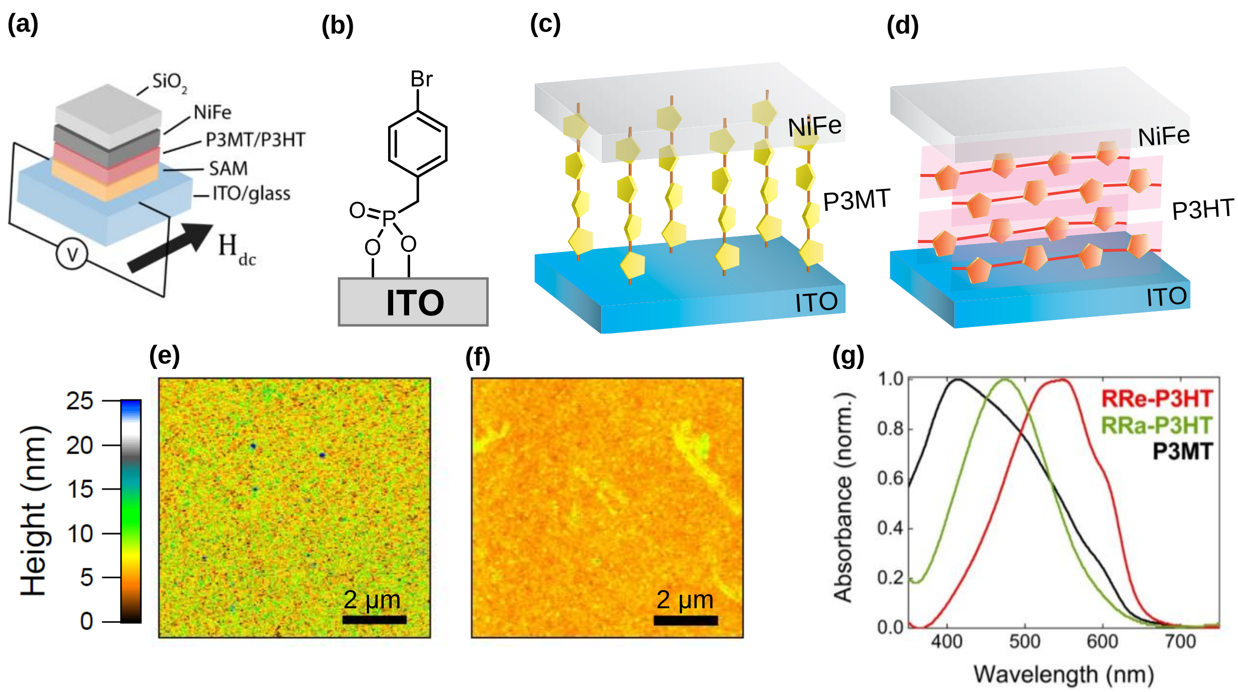

Figure 19. (a) Schematic representation of device structure (b) Structure of monolayer used to modify ITO prior to either (c) growth of poly(3-methylthiophene) (P3MT) polymer brush from the monolayer, or (d) deposition of poly(3-hexylthiophene) (P3HT) by spin casting. (e), (f) Respective characterization of P3MT polymer brush (6.3 nm average thickness, RMS roughness 2.6 nm) and spun-cast RRe-P3HT (6.5 nm average thickness, RMS roughness 0.7 nm) films by AFM. (g) Absorbance spectra for P3MT polymer brush and spuncast RReP3HT and RRa-P3HT films of 32 nm thickness.

Figure 19a shows a schematic of the fabricated device structures consisting of glass substrate/ITO (145 nm)/polymer (d_s)/NiFe (15 nm)/SiO_2 (50 nm), where the polymer layer constitutes a self-assembled monolayer (SAM) on top of the ITO film, followed by a spun-coat P3HT film or grafted P3MT polymer brush layer with thickness d_s, respectively. This tri-layer heterostructure design, where an organic semiconductor is sandwiched between a ferromagnetic top layer and bottom spin sink layer, allows for the facile measurement of these organic materials despite poor conductivities ($\sigma \approx 10^{-5} - 10^{-7} Scm^{-1}$ in undoped polyalkylthiophenes) and mobilities leading to the negligible generation of charge current within their layer, whereas for more conductive polymers (e.g. PEDOT:PSS $\sigma \approx 10^{3} Scm^{-1}$) a bilayer design may be used for the direct detection of charge current from the polymer [51].

The molecular structure of the SAM is shown in **Figure 19(b)**, with schematics of the two polymer heterostructures shown in **Figure 19(c-d),** highlighting their structural differences. For SAM preparation, the pre-treated ITO substrates (see the method in S.I. section I) were immersed in a 10 mM solution of (4-bromobenzyl)phosphonic acid in absolute ethanol overnight without stirring. The substrate was quickly dried under a stream of N_2 and annealed in an inert atmosphere at 150 °C overnight. Finally, the substrates were sonicated for several minutes in a 2:1 solution of ethanol/0.5 M aqueous K_2CO_3 to remove any physisorbed material, yielding monolayer-functionalized ITO.

Regioregular P3HT (Rieke Metals, M_n = 20 kg/mol, $Đ$ = 2.24) and regiorandom P3HT (Rieke Metals, M_n = 23 kg/mol, $Đ$ = 2.05) were spuncast at various speeds from chlorobenzene solutions of the appropriate concentrations onto monolayer-functionalized ITO substrates. P3MT brushes were synthesized by a surface-initiated Kumada catalyst transfer polycondensation, as described previously [86]. The films were used without annealing and stored in the dark under inert atmosphere (< 1 week). The resulting P3MT polymer brush and spun-cast P3HT film thicknesses were measured using atomic force microscopy (AFM) scratch profilometry. The film thickness was determined from ≥ 10 line-scans derived from ≥ 2 AFM scratch images. **Figures 19(e)** and **19(f)** show representative AFM scans for 6.3nm thick P3MT and 6.5nm thick RRe-P3HT films. It is evident from these images that the P3HT films exhibit a relatively smooth, homogenous surface while the P3MT films possess a densely packed columnar morphology with polymer columns oriented vertically out of the plane of the film, as we previously observed [86]. Absorbance spectra for 32 nm thick P3MT, RRa-P3HT, and RRe-P3HT films are shown in **Figure 19(g)** (see Supplemental Materials in Ref. [68]).

The prepared P3MT and P3HT films were directly transferred through a N_2 glovebox without exposure to air for the device fabrication. 15 nm of $Ni_{81}Fe_{19}$ (99.99% purity Angstrom Engineering) was deposited on top of the polymer films by e-beam evaporation (base pressure: ~5.0×10^{-8} Torr) at room temperature using a shadow mask, followed by a 50 nm SiO_2 (99.99%) capping layer. Ferromagnetic resonance (FMR) was performed at room temperature from 2 to 12 GHz using a commercial NanOSC PhaseFMR spectrometer with a coplanar waveguide, and an electromagnet was used for applying in-plane magnetic fields. For ISHE measurements, the microwaves are generated by a Keysight X-Series Microwave Analog Signal Generator at an excitation frequency of 9 GHz and microwave power of 50 mW. The ISHE voltage generated across the edges of the sample was measured using an EG&G 7260 DSP Lock-In Amplifier.

III. RESULTS AND DISCUSSION

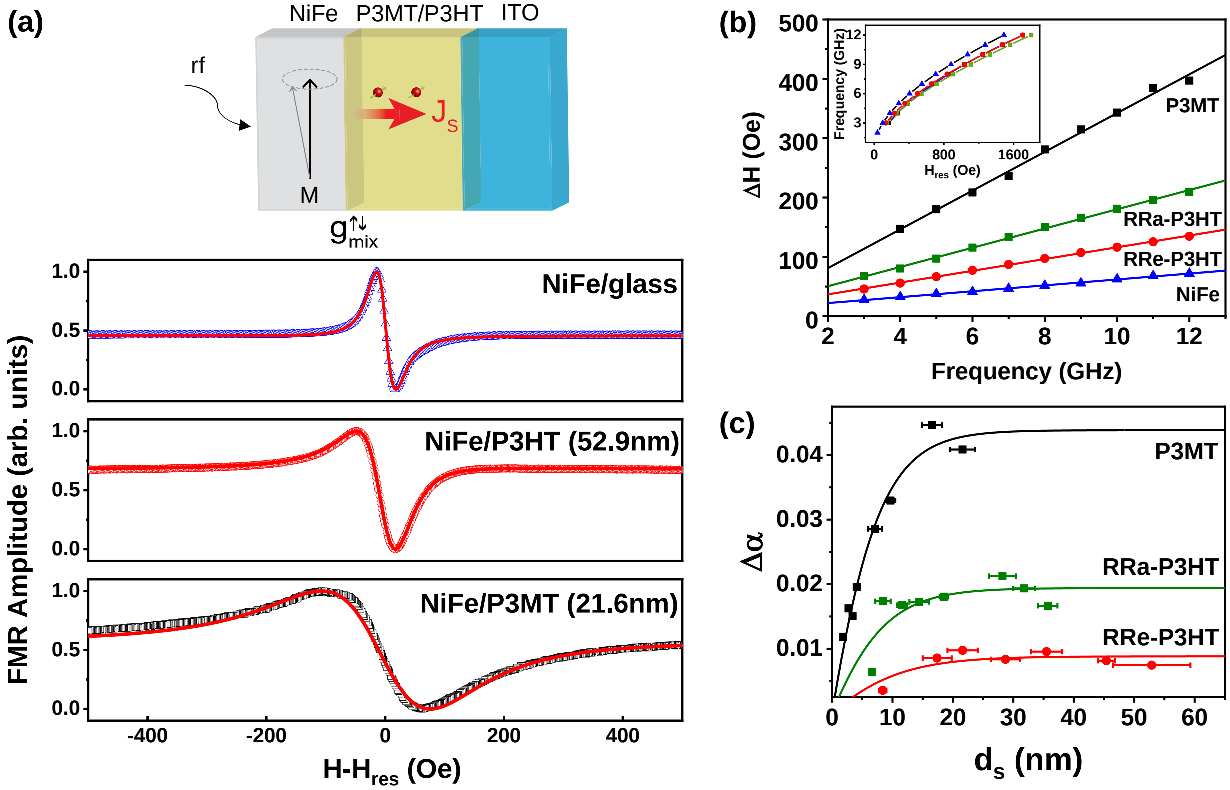

Figure 20. (a) Schematic representation of spin pumping during FMR and typical FMR spectra normalized by the resonant field (H_{res}) obtained at 9GHz for $Ni_{81}Fe_{19}$/glass, $Ni_{81}Fe_{19}$/RRe-P3HT(52.9nm)/ITO, and $Ni_{81}Fe_{19}$/P3MT(21.6nm)/ITO. (b) FMR linewidth (HWHM) versus microwave frequency for samples shown in (a), as well as RRa-P3HT, with linear fits for the derivation of the respective damping parameters. Inset shows microwave frequency plotted as a function of resonant field and associated fits to the Kittel equation. (c) Δα plotted as a function of thickness for P3MT, RRe-P3HT and RRa-P3HT series.

III.A Ferromagnetic resonance and spin mixing conductance

Figure 20(a) shows a schematic of the spin pumping process as well as typical FMR spectra measured at 9 GHz, from which values for α, the damping parameter, γ, the gyromagnetic ratio, and M_s, the saturation magnetization, are obtained. Damping factors are extracted using the relation $\alpha = \frac{\sqrt{3}\gamma}{4\pi f}\Delta H + H_0$ [15], as shown in **Figure 20(b)**, where ΔH is the FMR linewidth (HWHM) and f is the microwave frequency. H_0 is the frequency-independent linewidth contribution arising from inhomogeneities in the organic film and the ferromagnet. M_s and γ are obtained from the H_{FMR} versus f plots, shown in the inset of **Figure 20(b)**, by fitting to the Kittel equation: $(\frac{2\pi f}{\gamma})^2 = H_{FMR}(H_{FMR} + 4\pi M_s)$ [30], where H_{FMR} is the resonant field. Values for $4\pi M_s$ and γ for a bare NiFe reference sample are found to be 0.9609 T and 1.85×10^{11} $T^{-1}s^{-1}$, respectively, which are consistent with those reported in literature [15]. The intrinsic damping parameter, α_0, for the bare NiFe reference sample grown on top of the glass substrate is 7.2×10^{-3}, while the damping parameters of the NiFe/P3MT/SAM/ITO, NiFe/RRe-P3HT/SAM/ITO, NiFe/SAM/ITO, NiFe/ITO samples are equal to 4.8×10^{-2}, 1.8×10^{-2}, 8.7×10^{-3}, and 7.7×10^{-3}, respectively. This enhancement in the damping factor, α, has been attributed to spin-current dissipation across the ferromagnet/organic interface [51], [67], [79]. **Figure 20(c)** shows the enhancement of damping factor, $\Delta\alpha = \alpha - \alpha_0$, as a function of organic layer thickness in the NiFe/P3MT and NiFe/P3HT samples, respectively.

For the P3HT samples, $\Delta\alpha$ increases and then saturates as the thickness is increased above 20 - 30 nm, similar to the behavior observed in ferromagnet/non-magnetic metal bilayers [71]. For the P3MT samples, however, $\Delta\alpha$ increases at a much higher rate compared to the P3HT samples and exhibits no clear saturation even in the thickest film. We were unable to extract $\Delta\alpha$ from P3MT films with thickness > 30 nm due to roughness of the polymer brush film and low peak intensity (see SI for further details). The thickness-dependent enhanced damping factors were fit using a traditional spin pumping model [71]:

$$\Delta\alpha = \frac{\gamma\hbar}{4\pi M_s d_F} g_{eff}^{\downarrow\uparrow}$$

$$g_{eff}^{\downarrow\uparrow} = g^{\downarrow\uparrow} \frac{1}{1 + \left[2\sqrt{\varepsilon/3}\tanh(d_s/\lambda)\right]^{-1}}$$

where ħ, d_F, λ, and $g_{eff}^{\downarrow\uparrow}$ are the Planck constant, ferromagnetic layer thickness, spin diffusion length of the organic layer, and real part of the spin mixing conductance, respectively, and $g^{\downarrow\uparrow}$ represents $g_{eff}^{\downarrow\uparrow}(d_s \rightarrow \infty)$. ε is a dimensionless parameter proportional to the product of the atomic number and fine-structure constant in the nonmagnetic material and is fixed at ε = 0.1 (see section IV of S.I. for further discussion). We find that for the P3MT samples λ_s = 10.4 ± 1.1 nm and $g^{\downarrow\uparrow} = 1.06 \times 10^{21} \pm 5.1 \times 10^{19}$ m^{-2}, while for the RRe-P3HT samples λ_s = 15.0 ± 5.4 nm and $g^{\downarrow\uparrow} = 1.92 \times 10^{20} \pm 1.6 \times 10^{19}$ m^{-2} (For RRa-P3HT, λ_s = 11.7 ± 3.4 nm and $g^{\downarrow\uparrow} = 4.22 \times 10^{20} \pm 3.8 \times 10^{19}$ m^{-2}). Whereas the obtained spin diffusion lengths in both films are reasonable and consistent with most organic materials, the obtained spin mixing conductances, $g_{eff}^{\downarrow\uparrow}$ and $g^{\downarrow\uparrow}$, in the P3MT are surprisingly two orders of magnitude higher than that in the conventional metallic and semiconductor systems (in the range of 10^{18} to 10^{19} m^{-2}) despite containing predominantly light elements (i.e., mostly C and S in the polymer, minor amounts of Br, P, and O in the polymer and monolayer). This indicates an intensive spin current injection from the NiFe layer into the P3MT polymer (the injected spin current density at the interface, $J_S^0 \propto \frac{g_{eff}^{\downarrow\uparrow}\boldsymbol{\gamma}^2\boldsymbol{h}^2}{\boldsymbol{\alpha}^2}$, where $\boldsymbol{\gamma}$ is the gyromagnetic ratio, $\boldsymbol{h}$ is the B_1 field component of the MW excitation [15]), which is consistent with the enhanced electrical spin injection demonstrated previously in organic spin valves using P3MT polymer brushes [87].

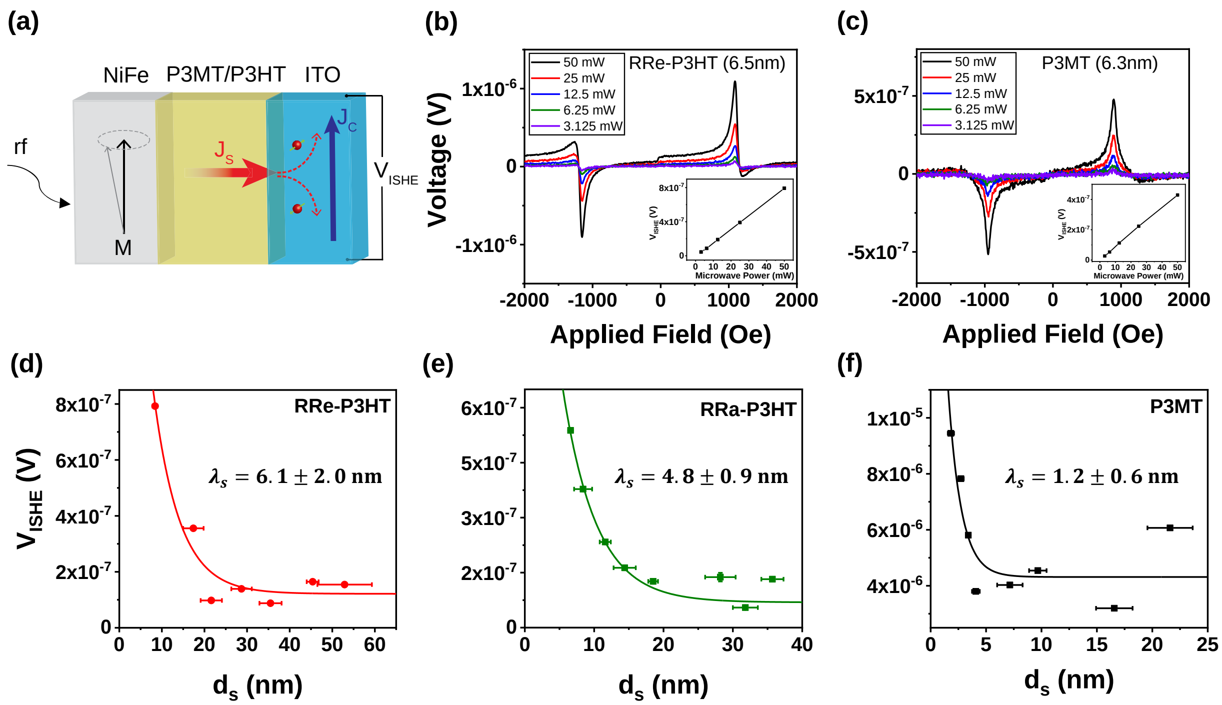

Figure 21. (a) Schematic representation of ISHE measurements. Total voltage containing both symmetric and antisymmetric contributions measured as a function of applied field for different microwave excitation powers at a frequency of 9 GHz is shown for (b) RRe-P3HT (6.5nm) and (c) P3MT (6.3nm), with insets showing the linear dependence of the extracted ISHE voltage (symmetric voltage contribution) versus microwave power. ISHE voltage plotted as a function of organic layer thickness is shown for (d) RRe-P3HT, (e) RRa-P3HT, and (f) P3MT, where the fitting curves represent a simple exponential decay function with $V_{ISHE} \propto V_0 e^{\frac{-d_s}{\lambda_s}}$.

III.B ISHE measurement

ISHE measurements were performed in a similar measurement setup used for FMR at room temperature. A sketch of the device structure used for the ISHE experiment is shown in **Figure 21(a)**. The pure spin current generated by the microwave dissipates into the polymer layer at the resonance field of FMR. By transmitting across the polymer spacer layer, the pure spin current (J_s) is converted into a transverse electric field (E_{ISHE}) via the inverse spin Hall effect in the ITO electrode [34]: $E_{ISHE} = \theta_{ISHE} J_s \times S$, where θ_{ISHE} is the spin Hall angle in the spin-to-charge converter (i.e., ITO electrode in this case) and S is the spin-polarization vector in the J_s along with the magnetization direction of the NiFe layer. We assume negligible spin-to-charge conversion occurring in the organic layers [θ_{ISHE} (Polymer) << θ_{ISHE} (ITO)]. The measured voltage is generated from the ITO layer, with a spin Hall angle on the order of θ_{ISHE} (ITO) = 0.0065 [88], which dominates the ISHE response. Consequently, this trilayer device is used as a sensitive detector of spin transport in the polymer film, thereby allowing for the facile extraction of the spin diffusion length, λ_s, in both P3MT and P3HT films.

Figures 21(b) and **21(c)** show typical spectra of the acquired voltage as a function of the applied magnetic field, obtained for different microwave excitation powers. The voltage signal can be decomposed into two parts, a symmetric and an antisymmetric voltage contribution given by $V(H) = V_0 + V_{Sym} \frac{\Delta H^2}{(H-H_{FMR})^2+\Delta H^2} - V_{Asym} \frac{\Delta H(H-H_{FMR})}{(H-H_{FMR})^2+\Delta H^2}$, where V_{Sym} is the voltage contribution stemming from the ISHE contribution in the ITO layer and V_{Asym} is the Anomalous Hall effect (AHE) contribution from the NiFe layer [15]. Flipping of the voltage polarity with reversal of the applied magnetic field from + H_{res} to – H_{res} provides strong evidence that the signal is indeed originating from the ISHE process. Here, we take the average of V_{Sym} for +H_{res} and -H_{res} as the actual V_{ISHE}, where $V_{ISHE} = [V_{Sym}(+H_{res}) - V_{Sym}(-H_{res})]/2$. Insets in **Figures 21(b) and 21(c)** show the linear dependence of the extracted V_{ISHE} as a function of applied microwave power. These tendencies are consistent with the expected behaviors of V_{ISHE} induced by the spin pumping and cancel out the possible thermal-induced ordinary Seebeck contribution that is field independent [89].

Figures 21(d-f) show the exponential decay behavior of V_{ISHE} as a function of organic layer thickness (d_s), which exhibit the expected monotonic decrease owing to the spin current transmission across the organic spacer layer between the ferromagnet and the spin sink [66]. By fitting the voltage thickness dependence to the exponential decay function, where $V_{ISHE}(d_s) \propto V_0 e^{\frac{-d_s}{\lambda_s}}$, we obtain values for the spin diffusion length, λ_s = 1.2 ± 0.6 nm in the P3MT layer at 300 K. Despite the P3MT having a higher conductivity than the P3HT layer ($\sigma_{RReP3HT} \sim 1 \times 10^{-7}$ S/cm < $\sigma_{P3MT} \sim 7 \times 10^{-6}$ S/cm) [86], [90], a longer spin diffusion length is obtained in the P3HT layer, with λ_s = 6.1 ± 2.0 nm for RRe-P3HT and λ_s = 4.8 ± 0.9 nm for RRa-P3HT. The P3MT layer has a consistently shorter spin diffusion length compared to that of the P3HT layer, in line with the results extracted from the FMR measurement ($\lambda_s \approx$ 15 nm for RRe-P3HT and ≈ 10 nm for P3MT).

It should be noted here that for spin pumping into organic materials, while the mechanism of spin current generation from FMR in the ferromagnetic thin film remains the same, there are key differences in the subsequent transmission of the spin current across the ferromagnet/organic interface, and in spin-to-charge conversion as it relates to the ISHE. Whereas in metallic systems and highly doped inorganic semiconductors spin transport is mediated primarily by free carriers, in organic semiconductors it is instead polarons that mediate spin transport as supported by spin pumping experiments performed in both local measurements using a vertical tri-layer system [66] and non-local measurements using a horizontal configuration [85]. A caveat to this is in highly doped conjugated polymers, where a sufficiently high spin density ($\sim 10^{20}$ cm^{-3}) results in an exchange-based spin diffusion regime allowing for the decoupling of spin and charge transport [85]. This is evidenced in the extracted λ_s of our undoped RRe-P3HT, which is two orders of magnitude shorter than the reported value in

F4TCNQ-doped P3HT (> 550 nm) [85]. A much lower conductivity and spin density in our undoped P3HT may greatly suppress the spin diffusion length, with spin transport mediated predominantly by polarons.

III.C Theoretical Model

There are two key findings from the results of the FMR and ISHE measurements. First, P3MT polymer brushes exhibit a shorter spin diffusion length and higher effective damping (i.e., spin mixing conductance) than that of P3HT films. The very short spin diffusion length (< 2 nm) suggests an additional spin-orbit coupling (SOC) contribution in the P3MT polymer brushes despite it containing the same elements with low atomic number as that in P3HT films with comparable hyperfine interaction. Second, the spin diffusion length obtained from fitting of the FMR data based on the spin backflow model is inconsistent with, and much larger than, that obtained through ISHE response with almost an order of magnitude variation in the case of P3MT (1.2 nm vs. 10.0 nm). This discrepancy has been observed in ISHE devices based on inorganic semiconductors such as in metal-silicon-metal vertical structures [91]. To address these two points, we need to revisit the origins of SOC in conjugated polymers. We note that the conventional spin pumping model, originally developed for metals, does not consider the heterogeneous interface and junction nor the band alignment between metals and organic semiconductors. Thus we next examine whether these equations used to derive the aforementioned parameters can be appropriately applied to our case with reasonable modifications.

Spin-orbit coupling (SOC) in polymers.

The origins of the SOC in organic materials have been examined theoretically [65]. It was found that, in comparison to inorganic systems, the SOC in disordered organic materials for spintronics can be conveniently characterized by a

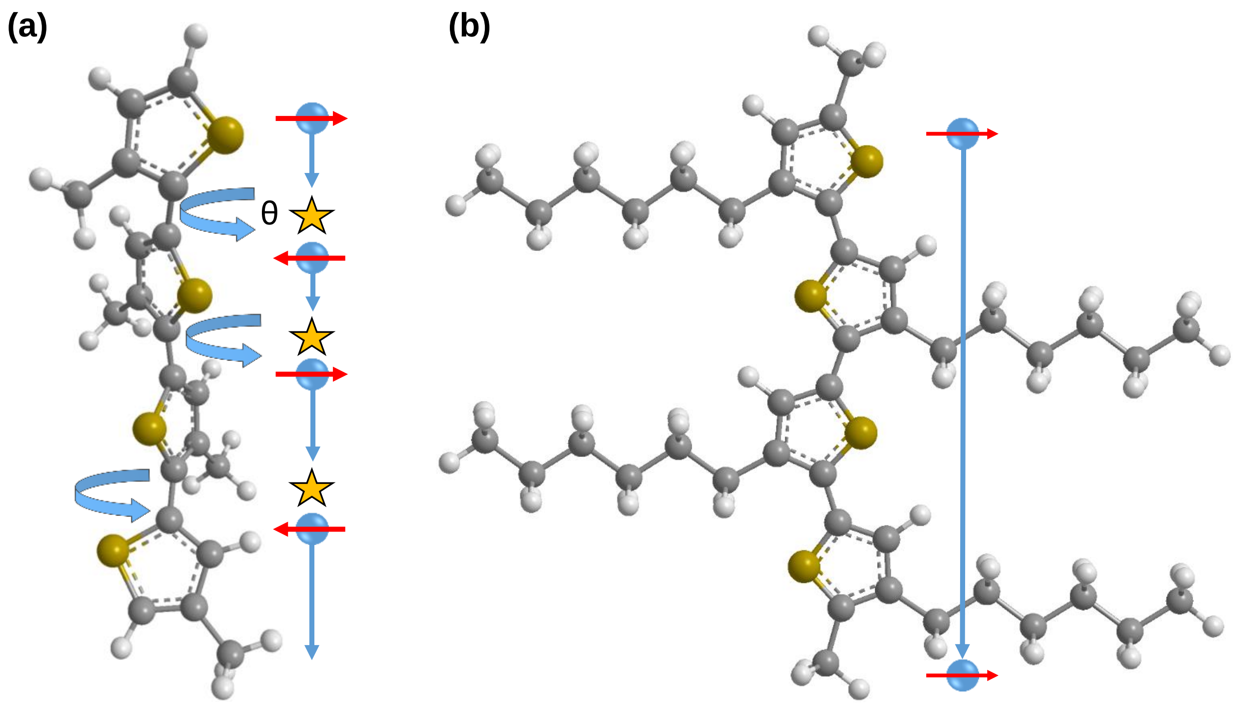

Figure 22. Schematic representations of (a) P3MT in which the thiophene backbone is twisted by an angle θ and (b) RRe-P3HT in a planar configuration. Blue spheres and red arrows represent electrons and their spin polarization direction, respectively, with spin flip scattering events located at torsion sites in the case of P3MT.

dimensionless spin-mixing parameter γ, and that the spin diffusion length can be expressed concisely as

$$\lambda = \frac{R}{4\gamma}$$

where R is the carrier hopping distance. For sexithiophene (T_6), which is a typical planar system comparable to the conjugated thiophene backbone of P3HT and P3MT, γ for electrons is ~ 6.7×10^{-3} [82]. Using this value along with a reported hopping distance R = 0.38 nm for P3HT [92], [93], we obtain a spin diffusion length of λ = 14.2 nm for P3HT. For P3MT, we must also consider the effect of the polymers' structural conformation on γ. P3HT has a relatively planar lamellar morphology, where polymer chains lie in the plane of the film with vertically oriented π-π stacking between adjacent chains (**Figure 22b**). The P3MT polymer brushes, on the other hand, are oriented vertically out of the film plane and possess a significant torsion angle between repeat units due to the nature of the growth method (**Figure 22a**), causing shorter average conjugation in P3MT and a blue shift in the P3MT absorbance spectrum compared to P3HT as seen in **Figure 19(g)**. The effect of torsion on the spin-mixing parameter γ can be expressed as

$$\gamma^2 = \gamma_0^2(1 + \alpha tan^2\theta)$$

where γ_0^2 is the SOC of the planar structure, θ is the torsion angle, and α is a numerical constant ranging from 0.135 to 0.5 according to modeling of biphenyl. As θ approaches 90°, and the π orbitals of the conjugated system are increasingly misaligned, γ^2 increases sharply. This structural conformational dependence of the SOC has been previously employed to explain the abnormally large SOC in Alq_3 molecules despite its lack of heavy elements, due to the nearly orthogonal relationship between aromatic ligands in the molecule [82]. By considering an example of a torsion angle for P3MT of θ = 65°, with α = 0.16 and $\gamma_0 = 6.7 \times 10^{-3}$, γ would be increased from 6.7×10^{-3} to 8.9×10^{-3}, resulting in a decrease of the spin diffusion length from 14.2 nm (calculated for the 'planar' P3HT) to 10.7 nm (calculated for the 'twisted' P3MT).

In addition, given constant but distinct SOC's for P3HT and P3MT, we would expect the FMR damping parameter for both polymers to saturate above a certain film thickness. Saturation of Δα is clearly observed with spuncast P3HT films thicker than ~20 nm, but not in the thickness range of measured P3MT films (**Figure 20c**). There are at least two possible explanations for non-saturating $\Delta\alpha$ behavior for P3MT: (i) saturation occurs in P3MT films thicker than can be measured with the experimental setup used here, or (ii) the SOC in P3MT changes with thickness. As noted previously, P3MT films possess more and more short conjugation units as they grow, evidenced by an increasingly strong blue-shifted feature in their absorbance spectra. An increase in the prevalence of short conjugation units in P3MT films may in turn cause an increase in the SOC with thickness and the observed non-saturating behavior in $\Delta\alpha$. In contrast, pre-synthesized P3HT has an average conjugation length that is primarily determined before film deposition, yielding a constant SOC with film thickness.

IV. CONCLUSION

FMR and ISHE measurements of P3MT polymer brushes and spun-cast P3HT films showed that the former has a significant enhancement in spin mixing conductance and reduction in spin diffusion length compared with the latter, despite their similar chemical structures. We attribute the observed large increase in damping with increasing P3MT film thickness to a torsion induced SOC, based on a model of spin pumping in disordered organic semiconductors. This study offers a new route for intrinsically tailoring SOC in organic semiconductors and achieving efficient spin injection for future spin-to-charge converter applications through manipulation of the structural conformation of conjugated polymers.

Acknowledgments

E.V. and D.S. are grateful for support from the startup funds provided by North Carolina State University and National Science Foundation Grant No. ECCS 1933297. Z.G.Y was supported by the US Army Research Office under contract No. W911NF-17-0511. I.V.W. was supported by the National Science Foundation Graduate Research Fellowship under Grant No. DGE-1650116. I.V.W and W.Y. were supported by NSF Grant No. DMR-1610879. Parts of this work were performed in part at the Chapel Hill Analytical and Nanofabrication Laboratory, CHANL, a member of the North Carolina Research Triangle Nanotechnology Network, RTNN, which is supported by the National Science Foundation, Grant ECCS-1542015, as part of the National Nanotechnology Coordinated Infrastructure, NNCI. DPK acknowledges support from the National Science Foundation (DMR-1751455).

Author contribution

D.S. and W.Y. conceived this study and the experiment. E.V., I.V. and L.Y. fabricated the devices. E.V. and S.Y. measured the FMR, spin pumping, and calibrated rf field. I.V. measured the AFM and XRD. S.K. and D.K. assisted in sample preparation. Z.G.Y. provided the theoretical model. E.V., I.V., and D.S. wrote the text. D.S. and W.Y. were responsible for the project planning and group managing. All authors discussed the results, worked on data analysis and manuscript preparation. The authors declare no competing financial interests.

3.2 Inorganic Semiconductor Spintronics

In conventional electronics, inorganic semiconductors have played a central role in the unparalleled technological advancements seen over the past few decades. Since the inception of the very first working transistor made of a Ge crystal in 1947 [94], for which Bardeen, Brattain, and Shockley received the 1956 Nobel Prize in Physics, inorganic semiconductors have transformed every aspect of modern technology. The reason for their success lies in their unique material and electronic properties, which can be manipulated to produce an almost limitless range of behaviors and controls.

In the field of spintronics, semiconductors are similarly important albeit less well understood. Perhaps the holy grail of semiconductor spintronics research would be the achievement of a functional, high-fidelity spin field effect transistor. First proposed by Datta and Das in 1990 [95], such a device would encode information in the two-state quantum system of the electron spin and not require the direct application of a charge current, potentially overcoming physical constraints of conventional MOSFETs as Moore's Law reaches its limit. While a robust spin-FET has yet to be realized, its creation would herald a critical advance with exciting prospects for quantum computation and memory storage.

Semiconductors also offer other benefits for many spintronics applications such as their ability to be electrically or optically gated, chemically doped, and fabricated with atomic precision. For instance, gating may be used to modify the effective spin-orbit coupling strength in a semiconductor material, which allows for control over spin and charge interconversion efficiency; a key control for manipulating spin in devices. Additionally, semiconductors may be engineered to form interesting electronic structures such as quantum wells [96], [97], two-dimensional electron or hole gases [98]–[100], and Rashba-type interfaces [101] that offer unique spin-dependent properties inaccessible to simple metallic systems. This chapter will provide a cursory overview of spin injection, transport, and dynamics in inorganic semiconductor materials and detail a study examining ultrafast spintronic capabilities in the widely researched wide bandgap semiconductor GaN.

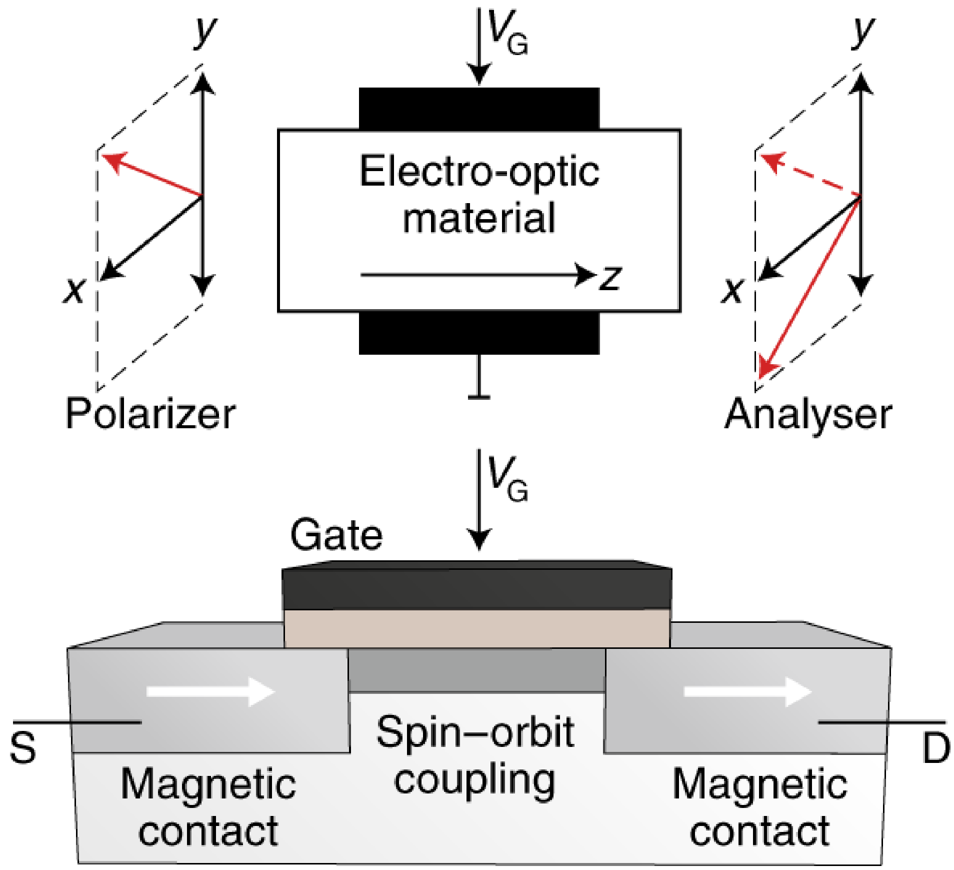

Figure 23. Concept of spin transistor originated by Datta and Das. (Top) Electro-optic modulator and its (Bottom) electron-wave analog. Image taken from Ref. [102].

3.2.1 Spin Injection in Inorganic Semiconductors

One of the key challenges faced at the outset of semiconductor spintronics was the problem of impedance mismatch at the interface between a ferromagnetic electrode and semiconductor material in the context of electrical spin injection [103], [104]. While spin polarized current transmission across a FM/PM metallic interface is highly efficient, the spin polarization is strongly reduced when the resistance of the respective materials differs substantially. This is particularly evident in the case of a FM/semiconductor interface where the semiconductor resistance is much higher than that of the ferromagnetic metal.

One method for circumventing this issue of impedance mismatch is to utilize ballistic electron transport such as in tunneling through Schottky barriers. In 2001, H. J. Zhu et al. observed spin injection from Fe into GaAs at room temperature with an efficiency of about 2% [105]. These results seemingly contradicted the predicted spin injection efficiency limit of 0.1% by Schmidt et al. in the absence of a 100% spin-polarized magnetic injector (i.e. an ideal half-metal). However, the authors explained their observations by way of the Schottky barrier formed at the Fe/GaAs interface, where electrons could tunnel through the energy barrier under appropriate bias conditions. Since the tunneling process is not subject to resistance mismatch, a higher spin injection efficiency could be achieved than what was predicted for conventional electronic transport. For electrical spin injection into semiconductors, the introduction of a spin-dependent tunneling barrier (usually an oxide) has allowed for enhanced spin injection efficiencies [106].

Alternatively, spin injection into semiconductors can also be attained through optical means. Georges Lampel first reported the generation of spin polarized carriers in response to optical pumping of a semiconductor with circularly polarized light in 1968 [107]. A decade later, Pierce and Meier built on a body of literature surrounding spin polarized photoemission in magnetic and nonmagnetic materials to describe how (110) GaAs could produce spin polarized electrons with a polarization maximum of 50% in response to circularly polarized illumination at the bandgap energy due to optical selection rules, as measured by Mott scattering [108]. Here, the strong spin-orbit coupling present in GaAs lifts the spin degeneracy of the band structure and, combined with its direct bandgap, allows for well-defined spin specific optical transitions depending on the polarization direction of incident illumination. Theoretically, it has been shown that through specific semiconductor surface construction and modification, along with varying the energy of polarized light excitation, spin polarizations of up to 100% can be achieved [109]. Experimentally, F. Pezzoli et al. achieved a spin polarization of ~85% for heavy holes in Ge/SiGe multiple quantum well heterostructures by taking advantage of phonon-induced intervalley scattering [110].

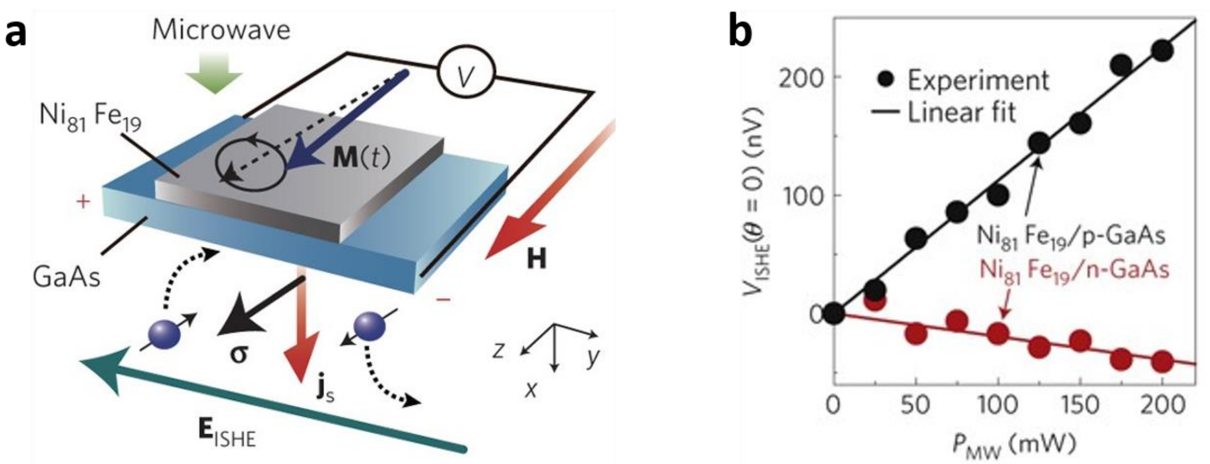

Figure 24. (a) Schematic illustration of $Ni_{81}Fe_{19}$/GaAs bilayer device used to study impedance-free spin injection via spin pumping. (b) Power dependence of the ISHE voltage generated from spin pumping into *n*-GaAs and *p*-GaAs showing opposite polarity. Figure taken from Ref. [111].

The spin pumping technique may also be used for direct spin injection into semiconductor materials, and is widely applicable. Ando et al. used this method to probe spin injection into n-GaAs and p-GaAs films interfaced with the ferromagnetic metal $Ni_{81}Fe_{19}$ [111]. They found that a dynamical exchange interaction between the localized spins of the FM and those of carriers in the semiconductor allowed for the direct transfer of angular momentum unaffected by impedance mismatch. The amplitude of spin currents injected in such a manner were observed to be several orders of magnitude higher than those typically observed through electrical spin injection methods using tunneling barriers. Additionally, it was found that application of a bias voltage between the ferromagnet and semiconductor in the $Ni_{81}Fe_{19}$/p-GaAs system, which formed a Schottky interface, controlled the magnitude of the exchange interaction and correspondingly the spin mixing conductance and spin Hall voltage. This result was explained in the context of interfacial band structure where the applied bias modified the depletion region and potential barrier of the Schottky contact and thus increased/reduced spin exchange at the interface. Since spin pumping only requires that the ferromagnetic material be excited at ferromagnetic resonance in order to generate and transfer spin current into the adjacent material, it has been used to study spin injection into a wide variety of inorganic semiconductors. For example, J. B. S. Mendes et al. studied spin-to-charge conversion in the two-dimensional semiconductor MoS_2 by spin pumping from the ferromagnetic insulator yttrium iron garnet [112]. Such atomically thin, reduced dimensional semiconductors are particularly interesting for their ability to form 2D electronic states that can exhibit spin-momentum locked band structures and potentially be modified by a bias field. The authors found that spin current injected into a four atomic layer thick MoS_2 sample was converted into a corresponding transverse charge current via the IREE with an efficiency comparable to many metallic systems and topological insulators, and two orders of magnitude larger than in graphene. Further demonstrating the versatility of the spin pumping technique, E. Lesne et al. probed spin currents injected from a $Ni_{81}Fe_{19}$ layer under the FMR condition into an adjacent oxide heterostructure consisting of $LaAlO_3/SrTiO_3$, which form a two-dimensional electron system (2DES) at their interface [113].

A very large spin-to-charge conversion efficiency in the 2DES was found, assigned to the IREE as a result of Rashba coupling at the interface. Remarkably, the application of a gate voltage was able to modulate the charge current density by over an order of magnitude and even reverse its polarity. This bias response was attributed to modification of the multiband nature of the 2DES where a shift in the Fermi level in response to a gate voltage changed the relative carrier occupancies of those bands, which in turn possess varying Rashba splitting strengths and conversion coefficients.

Finally, another intriguing mechanism for spin injection into inorganic semiconductors is to use femtosecond laser pulses to induce ultrafast demagnetization and spin current generation in an adjacent ferromagnetic metal, as described previously. In 2019, L. Cheng et al. used this technique to trigger "giant" spin injection into a monolayer of the popular transition metal dichalcogenide semiconductor MoS_2 and observe the generation of broadband THz radiation [114]. By analyzing the intensity of the emitted THz waveform, the authors were able to extract an injected spin density on the order of $10^6 – 10^8$ A cm^{-2}, which is several orders of magnitude higher than that obtained through either electrical spin injection (~ 10^0 A cm^{-2}) or spin pumping (~$10^2 – 10^3$ A cm^{-2}). It was proposed that the band gap of the semiconductor used here is able to act as a spin filter for the injected ultrafast spin current bursts. High energy majority and minority-spin electrons generated during laser excitation in the adjacent ferromagnet are subject to spin-dependent scattering rates. Minority spins decay rapidly in energy as they reach the FM/semiconductor interface due to their relatively high scattering rate and are filtered by the semiconductor's bandgap, unable to overcome the high energy barrier. Majority spins, on the other hand, are able to reach the interface while still maintaining significant energy sufficient to overcome the bandgap and traverse the interface. This unique effect is very promising for the application of inorganic semiconductor materials to ultrafast spintronics, offering not only a way to increase spin injection efficiencies but also to possibly control them through additional bias fields.

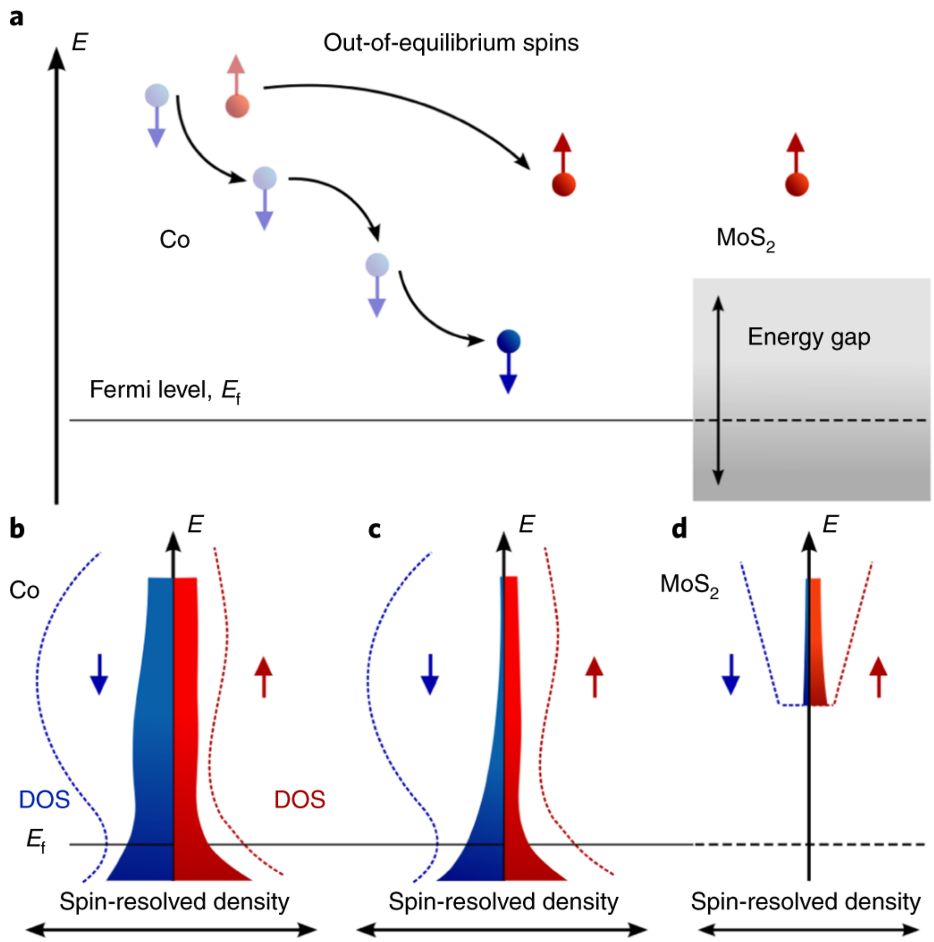

Figure 25. Schematic illustration of spin injection from Co into monolayer MoS_2. High-energy electrons, generated by the fs laser, have spin-dependent scattering rates. Minority electrons (blue) quickly decay to low energy and are consequently prevented by the bandgap from entering the MoS2. E, energy. b–d, Electron population during spin-injection process. b, Initial out-of-equilibrium electronic distribution generated by the laser absorption. c, Due to the lower scattering rates, the majority-spin channel (red) retains an out-of-equilibrium distribution, while the minority-spin electrons (blue) have already decayed to a Fermi–Dirac distribution. d, The MoS2 bandgap acts as a filter and allows only high-energy electrons from Co to cross the interface, leading to a high spin polarization of the injection. DOS, density of states. This figure is taken from Ref. [114].

3.2.1 Spintronic Terahertz Emission in $Ni_{81}Fe_{19}$ / *n*-GaN Heterostructures

The following section is adapted from published work in Ref [115].

Observation of carrier concentration dependent spintronic terahertz emission from *n*-GaN/NiFe heterostructures

Eric Vetter[1,3 †], Melike Biliroglu[1†], Dovletgeldi Seyitliyev[1], Pramod Reddy[2], Ronny Kirste[2], Zlatko Sitar[3], Ramon Collazo[3], Kenan Gundogdu[1,4*], Dali Sun[1,4*]

[1]*Department of Physics, North Carolina State University, Raleigh, NC 27695, USA*

[2]*Adroit Materials, Inc., 2054 Kildaire Farm Rd., Cary NC 27518, USA.*

[3]*Department of Materials Science and Engineering, North Carolina State University, Raleigh, NC 27695, USA*

[4]*Organic and Carbon Electronics Lab (ORaCEL), North Carolina State University, Raleigh, NC 27695, USA*

[†]These authors contributed equally to this work

*Author to whom correspondence should be addressed: kgundog@ncsu.edu, dsun4@ncsu.edu

Abstract

The development of terahertz (THz) spintronics has opened a new paradigm for the generation of THz radiation through the combination of ultrafast magnetism and spin-based electronics. However, research in this area has primarily focused on all-metallic devices comprising a ferromagnetic thin film adjacent to a non-magnetic heavy metal. Here, we report the experimental observation of spintronic THz emission from an n-doped wide bandgap semiconductor, *n*-GaN. We found that the amplitude of THz emission strongly depends on the

carrier concentration of the semiconductor layer, which could be attributed to the tunable Rashba state occurring at the *n*-GaN/ferromagnet interface. Our work offers exciting prospects for pursuing wide bandgap semiconductor-based spintronic THz devices and demonstrating their intriguing spin Hall physics at the ultrafast timescale.

Introduction

The generation and detection of terahertz (THz) radiation is of immense technological importance for a variety of current and future applications such as non-destructive examination [116]–[120], wireless communication [121]–[123], and ultrafast computing [124], [125]. Recently, a new mechanism for the generation of THz radiation via ultrafast spintronics has opened the door to search for novel material classes and devices, and offered the possibility for new THz device functionalities [44], [126], [127]. These devices are all-metallic in nature, and comprise a ferromagnetic thin film adjacent to a non-magnetic heavy metal with strong spin-orbit coupling (e.g. $Ni_{81}Fe_{19}$/Pt) [127]–[129]. Here, the principle of operation is based on ultrafast demagnetization of the ferromagnetic thin film in response to an incident, femtosecond laser pulse, followed by conversion of the resulting superdiffusive spin current into a transient THz electric field via spin-to-charge conversion processes (e.g., inverse spin Hall effect [15]) in the adjacent heavy metal. These spintronic THz emitters may outperform most semiconductor-based THz emitters in terms of ultrabroadband THz emission up to 20 THz [130], comparably cheap and facile production, and the ability to be manufactured on flexible substrates [128]. Their spintronic nature also allows for additional functional controls, such as phase reversal of the emitted THz waveform by reversal of the polarity of an applied magnetic field [44]. However, these metallic-based devices lack certain desirable attributes of their semiconductor counterparts such as the ability to be electronically doped or electrically gated, providing a barrier to further device optimization and functionalities.

Besides the metallic materials systems, spintronic THz generation has also been recently reported in a two-dimensional semiconductor, MoS_2 [114], showing the ability to convert a 'giant' ultrafast spin current injected across the metal/semiconductor interface owing to a sizable bandgap in the semiconductor. Upon femtosecond laser excitation, only the spin-polarized electrons with excitation energy higher than the semiconductor's conduction band minimum can be transmitted through the metal/semiconductor interface, resulting in a highly spin-polarized current in the semiconducting layer [114]. It is thus anticipated that a high bandgap semiconductor forming a larger Schottky barrier may act as a more efficient spin filter by which a higher intensity spintronic THz emission can be generated.

Gallium nitride (GaN) is a well-known wide bandgap (3.4 eV) semiconductor lauded for its remarkable optoelectronic properties that make it an ideal candidate for high-power and high-frequency devices and applications [131], [132]. Intriguingly, due to its non-centrosymmetric, polar wurtzite crystal structure, it has also been shown to possess a spin-split electronic band structure due to the bulk inversion asymmetry of the crystal lattice, i.e., a Rashba state (α_R = (4.5 ± 1) meV·A [133]), allowing for large spin-to-charge conversion efficiencies for spintronic applications [76]. Taken together, these remarkable properties make bulk GaN a prime material candidate for use in ultrafast THz spintronics. The convergence of spintronic THz generation and these robust wide bandgap semiconductor materials would result in next generation of spintronic THz emitters with advanced semiconductor-based capabilities.

Here, we present a wide bandgap semiconductor-based spintronic THz emitter comprising a ferromagnetic thin film ($Ni_{81}Fe_{19}$) interfaced with an n-doped, wide bandgap semiconductor (*n*-GaN). We conduct THz time-domain spectroscopic measurements of the emitted THz electric fields as a function of carrier concentration in the semiconductor material. We found that the emitted THz field amplitude is strongly dependent on the carrier concentration in the *n*-GaN layer, pointing to an exciting convergence of wide bandgap semiconductors and ultrafast spintronics both for fundamental spintronic physics and THz device functionalities.

Results and Discussion

All *n*-GaN samples studied here were grown on sapphire substrates in a vertical, cold-walled, RF-heated, low pressure MOCVD reactor [134]. Systematic variation of the carrier concentration was achieved through doping with either Si or Ge. The doped carrier concentration and electron mobility in the *n*-GaN layers were determined through room temperature Hall effect measurements in a van der Pauw configuration [134]. The morphology of the prepared n-GaN surface is characterized by Atomic Force Microscopy (AFM). A top $Ni_{81}Fe_{19}$ (NiFe) layer is deposited using electron beam evaporation onto a 10 × 10 mm area of the *n*-GaN film, with a thickness of 5 nm. THz experiments are carried out using the output of a 1 kHz repetition rate Ti:sapphire amplifier (Quantronix Integra-C). The central wavelength is 800 nm and pulse duration is 120 femtosecond [130]. The E_y and E_x components of THz radiation were recorded using a pair of wire-grid polarizers. A 300 mT in-plane external magnetic field is applied to the THz samples, which is sufficient to magnetize the NiFe layer along the in-plane direction during the measurements (**Figure 26**). All measurements are taken at room temperature.

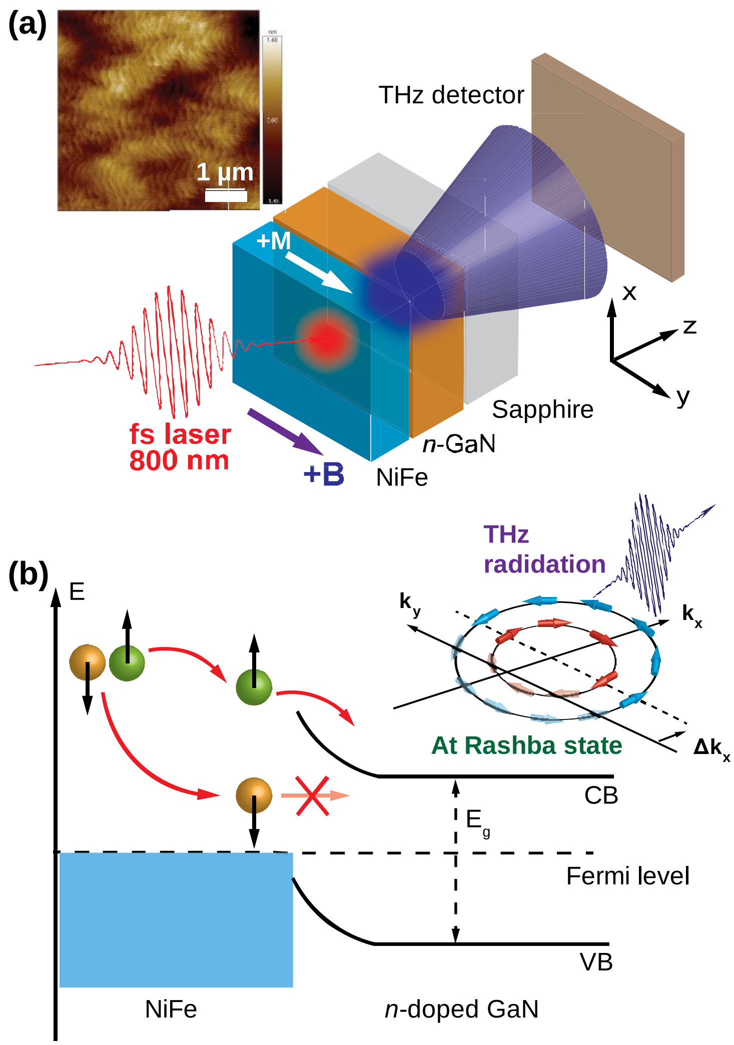

Figure 26. (a) A sketch of spintronic THz radiation generated from a doped wide bandgap semiconductor, n-GaN, via an efficient spin-to-charge conversion process upon excitation from ultrafast laser pulses. The top left inset shows a representative AFM image of a fabricated n-GaN film, showing a smooth and uniform morphology with RMS less than 1.48 nm. (b) Schematic of spin injection from NiFe into the wide bandgap n-GaN semiconductor, where majority spin polarized electrons are able to enter into the semiconductor's conduction band while minority spin polarized electrons rapidly decay and are blocked from entering by the high Schottky barrier formed at the NiFe/n-doped GaN interface.

Figure 26(a) shows a schematic illustration of the sample devices and THz emission process, with a representative AFM image of the prepared *n*-GaN film prior to deposition of the NiFe layer shown in the top left inset. Here, a femtosecond laser pulse is used to excite the ferromagnetic NiFe layer, whose magnetization direction is controlled by an external permanent magnet, resulting in ultrafast demagnetization [37]. Subsequently, a high energy, superdiffusive spin current is generated [38]–[40] and injected across the interface into the adjacent non-magnetic *n*-GaN film where it is converted into a transient THz electric field via a spin-to-charge conversion processes [44]. Since *n*-GaN has a non-centrosymmetric wurtzite structure and the presence of Rashba states in this system has been well documented [135], [136], it is expected that the spin-to-charge conversion process here is dominated by the Inverse Rashba Edelstein Effect (IREE) rather than the Inverse Spin Hall Effect (ISHE) given the weak spin-orbit coupling provided by light elements comprising the material. The emitted THz waveform is then electro-optically detected using a 1 mm thick [110] ZnTe crystal. **Figure 26(b)** schematically depicts the spin injection process whereby spin polarized minority carriers decay rapidly in energy and are filtered by the high Schottky barrier formed at the NiFe/*n*-GaN interface, while majority spin carriers are able to enter into the conduction band of the semiconductor [114], [137].

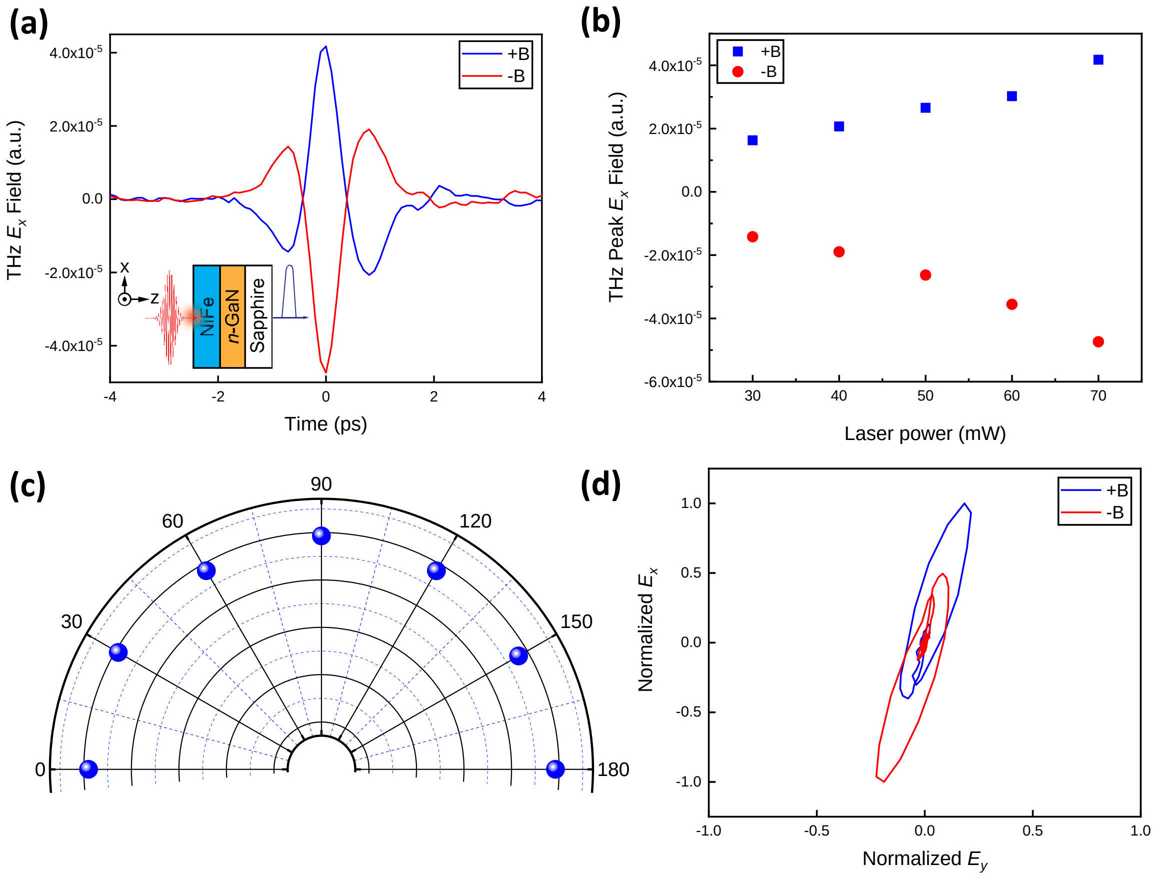

Figure 27. **(a)** Typical time trace of measured THz-electric field from the *n*-GaN (n=5×10^{16})/NiFe heterostructure under positive (+*B*) and negative (-*B*) magnetic fields, respectively. The emitted THz pulse changes phase with applied magnetic field. **(b)** Dependence of the peak-to-peak THz-electric field amplitude on the pump laser power. **(c)** Normalized peak amplitude of the generated THz-electric field as a function of the rotation of the laser polarization. **(d)** Parametric plot of THz-electric field amplitudes, which are both polarized along the x-direction, confirming their spintronic nature.

In **Figures 27 and 28**, a series of control experiments has been performed in order to confirm the spintronic origin of the emitted THz pulse. A typical spintronic-THz emission waveform is shown in **Figure 27(a)** under both positive and negative applied magnetic fields, demonstrating the spintronic nature of the emission process in which the phase of the THz waveform is inverted with a reversal of the magnetic field polarity. Laser power dependence of the peak THz intensity is depicted in **Figure 27(b)**, showing that the THz electric field scales nearly linearly at low laser pump fluences. A pronounced superlinear power dependence indicates a possible high-order effect caused by multi-excitation mechanism [138]. **Figure 27(c)** plots the peak THz intensity as a function of linear polarization angle (θ_p) of the incident laser. Absence of significant angular dependence is consistent with literature reports of spintronic THz emission [138]. A parametric plot of the THz electric field shows the polarization of emitted THz pulse is mainly along the x-direction as a cross product of the NiFe magnetization along the y-direction (M_{+y}) and the spin diffusion direction ($J_{+z}(s)$) along the z-direction (i.e., $E_{-x} \propto J_{+z}(s) \times M_{+y}$) [44].

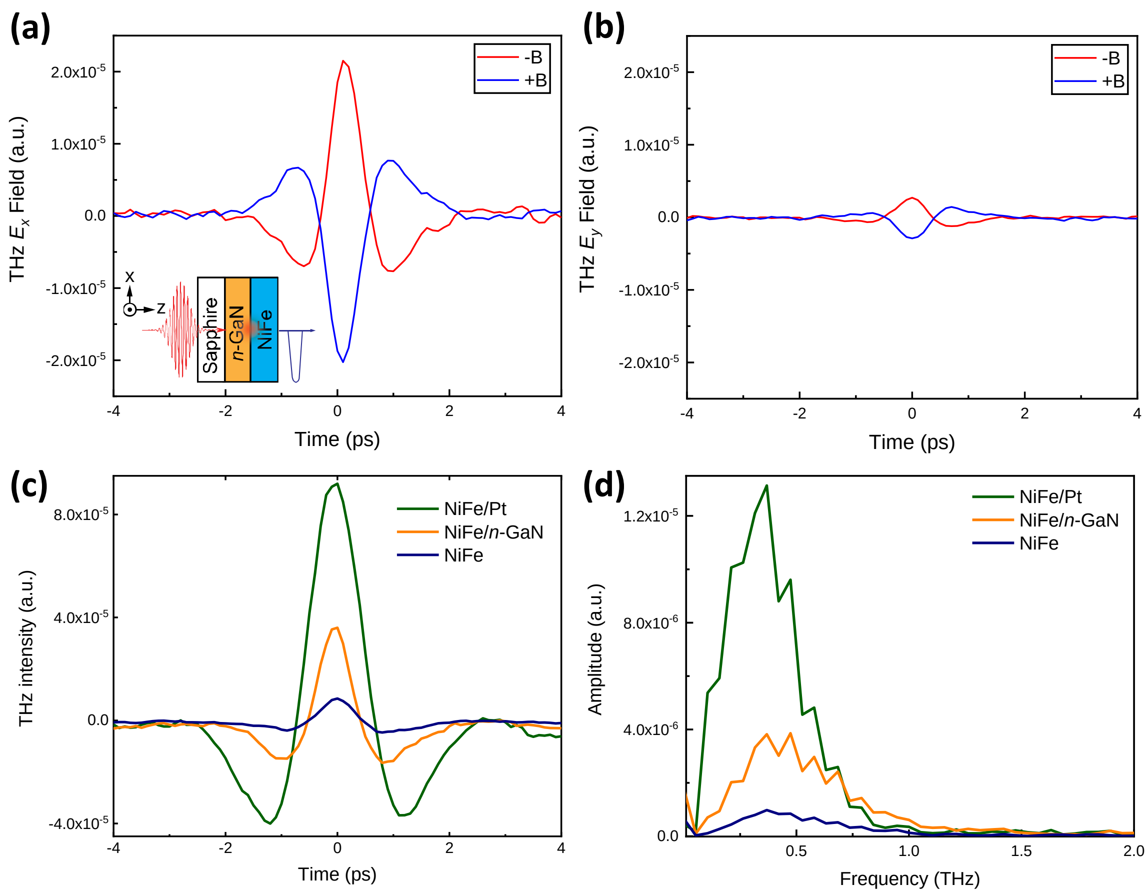

Figure 28. Time traces of E_x **(a)** and E_y **(b)** components of the generated THz-electric field in the same NiFe/n-GaN sample using a back-pump configuration, i.e., ultrafast laser pulse is excited through the sapphire substrate. The position of zero time is chosen arbitrarily. **(c)** and **(d)** Comparison of the time- and frequency-domain of the THz-electric field along the x-direction for NiFe(5nm)/Pt(5nm), NiFe(5nm)/*n*-GaN(300nm), and bare NiFe(5nm) samples, respectively.

The E_x and E_y components of the linearly polarized THz emission when excited from the back side of the sample are shown in **Figure 28(a)** and **(b)**, respectively. In this inverted measurement geometry, the excitation laser pulse is incident first upon the sapphire substrate before transmitting across the *n*-GaN layer (~300 nm-thick), and then ultimately reaching the

NiFe layer. The 800 nm laser pump pulse is transparent to both the sapphire substrate and the *n*-GaN film given their wide bandgaps. Thus, the THz emission process is still the same as in the case of normal measurement geometry as shown in **Figure 27**. However, while the orientation of the external magnetic field (i.e., magnetization of the NiFe layer along the +y direction) remains the same, the spin current vector, $J_{-z}(s)$ is reversed in the back-pump configuration (i.e., the spin current is still injected from NiFe into the n-GaN but along the -z direction), resulting in an inverted phase of the emitted THz waveform as observed in both E_x and E_y components of **Figure 28(a)** and **28(b)**. This sample orientation dependence experiment unambiguously confirms the spintronic origin of the THz emission from the NiFe/*n*-GaN heterostructure.

Figure 28(c) compares the THz emission from *n*-GaN with that from NiFe/Pt and NiFe-only control samples, with their corresponding Fourier transforms shown in **Figure 28(d)**. The bandwidth of the THz emission spectra extends up to 1 THz, which is limited in part by the use of the ZnTe crystal in the THz detection setup [127]. It is noted here that the overall THz intensity for NiFe/Pt is roughly two times greater than that in the NiFe/*n*-GaN. While this may be related in part to differences in spin-to-charge conversion efficiencies between the two materials, there are additional contributing factors such as Fabry-Pérot interference that should be taken into account when making comparisons [127], [128], [139]. The lack of significant THz emission from the NiFe-only control sample rules out the possible THz generation stemming from nonlinear optical or interfacial-related ISHE process in the NiFe layer, which has been reported before in the pure Co films [138], [140]. All the control experiments confirm that the origin of the emitted THz radiation is from the ultrafast spin-to-charge conversion occurring in the *n*-GaN layer.

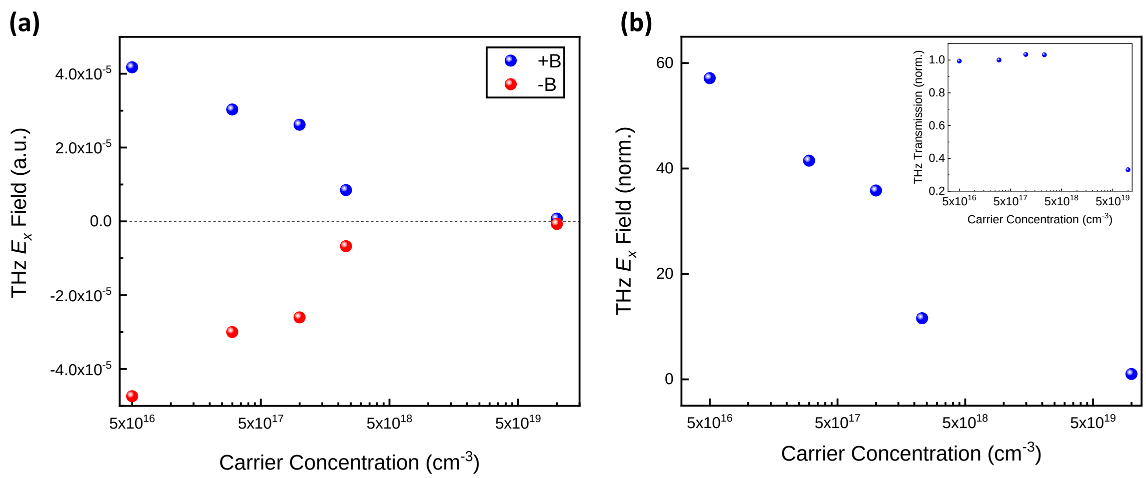

Figure 29. **(a)** Peak amplitude of the THz-electric field as a function of carrier concentration in the NiFe/*n*-GaN samples under two magnetic fields. **(b)** Carrier concentration dependent amplitude of THz radiation normalized by the THz transmission through the device structure. The inset shows the measured THz transmission (0.2 – 2 THz) as a function of carrier concentration.

Figure 29(a) shows the dependence of the peak THz emission intensity on the doped carrier concentration in the *n*-GaN layer under 1mJ/cm^2 (i.e., 70 mW, 3mm spot size) laser excitation in the normal incidence measurement geometry, which represents the main finding of our work. Remarkably, we found that the emitted THz intensity drops logarithmically as the semiconductor layer is doped to successively higher carrier concentrations. It is noteworthy that this decrease cannot be explained by the influence of effective spin mixing conductance formed at the metal/semiconductor interface which is not subject to the impedance mismatch problem as reported in the Fe/doped-GaAs system under microwave excitations in the GHz range [111]. By reversing the applied magnetic field, the inverted phase of roughly symmetric THz intensity confirms that the generated THz emission is still dominated by the ultrafast spin-to-charge conversion process in the *n*-GaN film as discussed before.

One possible explanation for this decrease could be a simple reduction in THz transmission through the entire sample structure as a function of carrier concentration. According to the Drude model, the dielectric permittivity of a material is dependent on its free electron density. An increase in carrier density may result in a decrease in the dielectric permittivity of the material in the THz frequency regime, and a concomitant increase in the plasma energy. This combined effect may work to suppress the transmission of the THz electric field [141]. To verify this possibility, a normalized plot of the THz transmission (0.2 – 2 THz) as a function of carrier concentration is presented in **Figure 29(b)**, with the inset showing peak THz intensity normalized by the transmission for different carrier concentrations. It is shown that the THz transmission is relatively constant across a wide range of carrier concentrations, and even though it decreases by a factor of 3 in the highest concentration sample (1×10^{20} cm^{-3}), the THz emission intensity by this point has already decreased by a factor of 60 and thus cannot solely account for the observed behavior.

A second possibility that may play a role in the observed carrier concentration dependence of the THz emission intensity is related to the Schottky barrier that forms at the metal/semiconductor interface when the metallic NiFe layer is put in contact with the semiconducting *n*-GaN layer, given the difference in work functions between the two materials (NiFe = 4.8 [142], GaN = 4.1 [143]). This results in the formation of a depletion region at the metal-semiconductor interface, the width of which is inversely proportional to the square root of the doping concentration in the semiconductor. In addition, the resulting electric field at the interface, according to Gauss's Law, is linearly proportional to the square root of the doping concentration and will have a fixed electrical polarization. A tuning of this interface electric field as a function of carrier concentration may affect the spin-to-charge conversion efficiency of the Rashba state by shifting the spin-split bands in reciprocal space, similar to what has been observed through gating experiments in Rashba-split 2DEG systems [72]. Since only n-doped GaN was investigated in this study, the polarity of the electric field in the depletion region is fixed and thus would be akin to gating with only one voltage polarity. Further experiments in order to elucidate the exact mechanism behind the observed behavior are warranted.

In conclusion, we report the first observations of the spintronic THz emission from NiFe/*n*-GaN heterostructure as a function of carrier concentration in the semiconductor layer. Not only do we observe THz emission even in a wide bandgap semiconductor, owing to the superdiffusive nature of the operating spin current, but also we found that THz emission intensity decreases exponentially with increasing n-type carrier concentration. Several possible explanations for the observed behavior related to the Rashba spin-splitting state are offered. This work offers exciting prospects for both the development of new semiconductor-based spintronic THz devices and fundamental physics.

Acknowledgements

E.V. and D.S. acknowledge the support from National Science Foundation, ECCS-1933297, and NC State University-Nagoya Research Collaboration Grant. M.B. D.S., and K.G. acknowledge the support from ROI from UNC system. P.R., R.K., Z.S. and R.C. acknowledge the partial support from National Science Foundation, (ECCS-1916800, ECCS-1610992, and ECCS-1653383) and by the Air Force Office of Scientific Research (AFOSR) (No. FA-95501710225).

3.2 Hybrid Organic-Inorganic Perovskite Semiconductor Spintronics

Hybrid organic-inorganic perovskite semiconductors have garnered an immense amount of research interest in recent years, primarily related to their application in high efficiency solar cells. The combination of a metal halide framework with organic ligands leads to a myriad of interesting properties that may be intermediate to those of the respective inorganic or organic materials themselves. Spin behavior in this class of materials is particularly interesting since at first glance the inorganic and organic components seem to possess competing effects. On the one hand, the metal halide framework is typically composed of heavy elements where the metal cation is Pb or Sn and the halide anion is Br or I. As discussed previously, these heavy elements possess very strong spin-orbit coupling and can be expected to interact strongly with electron spin. On the other hand, the organic ligands in these compounds are composed of light elements like C, N, O, and H and therefore possess relatively weak spin-orbit coupling and may allow for longer spin relaxation rates and spin lifetimes. Additionally, these hybrid metal halides are often optically and electronically active as a result of their band structure allowing for the potential of gating as a means of modifying their spin-dependent properties. Therefore, it is interesting to examine spin injection, spin transport, and spin-to-charge conversion in these materials in order to determine their spintronic functionalities.

3.2.1 Spin Dependent Phenomena in Hybrid Organic-Inorganic Perovskites

The first examination of hybrid perovskite spintronics devices were performed by J. Wang et al. in 2019, where the authors measured a spin light emitting diode and vertical spin valve using methylammonium lead bromide ($MAPbBr_3$) as the active semiconductor material [144]. While previous studies had reported interesting magnetic field effects [145], optical spin selection rules [146], [147], and Rashba-split band structures [148], [149], this report was the first to integrate these hybrid semiconductor materials into functional spintronics devices and measure relevant spin-dependent properties such as the optical and electrical Hanle effects, circularly polarized electroluminescence, and giant magnetoresistance.

Here, the authors first verified the existence of optical spin selection rules in $MAPbBr_3$ that allow for spin injection via circularly polarized light excitation, as was described in Section 3.2.1 with regards to GaAs. At 10 K, an $MAPbBr_3$ thin film excited by a 532 nm circularly polarized laser resulted in the emission of circularly polarized photoluminescence. The degree of circular polarization obtained in this manner was approximately 3.1%. Additionally, the optical Hanle effect was measured by applying a magnetic field perpendicular to the light propagation direction. This oblique field causes spin precession to occur within the film that reduces the degree of polarization in the emitted PL. By fitting the oblique field-dependent PL data, an effective exciton spin lifetime of $\tau_s \approx 500$ ps was obtained, which is remarkable given the material's presumably large spin-orbit coupling.

For the measurement of circularly polarized electroluminescence (EL), the authors constructed a spin-LED comprised of LSMO / $MAPbBr_3$ / TPBi / Al, where the LSMO serves as a ferromagnetic anode for the injection of spin-polarized holes into the hybrid perovskite layer, the TPBi molecular thin film serves as an electron transport layer, and the Al is a capping layer cathode. When an external magnetic field was applied in the direction perpendicular to the plane of the film, and the device was biased at voltages greater than 5 V, a circularly polarized EL emission was observed whose handedness depended on the polarity of the applied field. By taking the ratio of the degrees of circular polarization obtained from EL compared with PL, a spin injection efficiency of 26% at 10K was determined. This highly efficient spin injection is somewhat surprising considering the large conductivity mismatch between the metallic LSMO electrode and semiconducting $MAPbBr_3$, and may be attributed to the formation of spin-split surface Rashba states.

The final device considered in this report was a vertical spin valve consisting of an LSMO bottom ferromagnetic electrode, an $MAPbBr_3$ thin film spacer layer, and a Co top ferromagnetic electrode capped with a thin layer of Au. By varying the in-plane magnetic field from +250 mT to -250 mT at 10 K, a giant magnetoresistance of up to 25% was observed. In addition, the application of a perpendicular magnetic field allowed for the measurement of the electrical Hanle effect, a critical test for the unambiguous demonstration of spin injection and transport occurring in the semiconductor layer. Using this technique, a very long spin lifetime of τ_s = 940 ps was extracted which is notably longer than that for excitons. Accordingly, a spin diffusion length of approximately 220 nm was determined using the Einstein relation. The long spin lifetime and spin diffusion lengths in this hybrid perovskite material are eminently remarkable considering the dominance of heavy elements in its structure, and provide a unique opportunity for next generation spintronic devices to utilize a semiconductor material that simultaneously possesses strong spin-orbit coupling and favorable spin transport properties.

Perhaps the most intriguing property of hybrid perovskite semiconductors with respect to spintronics is the presence of Rashba spin-split band structures at the interfaces formed with common ferromagnetic electrodes. Aided by the strong spin-orbit coupling of the metal halide framework and breaking of inversion symmetry at the interface, these materials may potentially possess giant spin-to-charge conversion efficiencies. However, research in this area and the nature of these interfacial states are still being investigated in the literature.

In 2015, M. Kepenekian et al. published a study using symmetry analysis, density function theory, and k-p modeling to examine Rashba and Dresselhaus effects in hybrid organic-inorganic halide perovskites [149]. Their theoretical results indicated that in a reduced dimensional form, materials such as $MAPbBr_3$ and $MAPbI_3$ could exhibit significant Rashba spin splitting. This finding has important implications for spintronics since it offers the possibility of controlling spin precession in this semiconductor material class via a gate voltage, which could open the door to the realization of a spin-FET, for example. J. Yin et al. confirmed this result with their own DFT calculations, and extended the analysis to include Ruddelsden-Popper phase hybrid perovskites as well [150]. They demonstrated that the Rashba effect in typical 3D and 2D hybrid perovskites is strongly dependent on structural distortions associated with the respective surface terminations of the materials, in addition to the number of layers (n = 1, 2, 3 etc.) in the 2D case.

Experimentally, Niesner et al. used angle-resolved photoelectron spectroscopy to measure the valence band dispersion of a single crystal of $MAPbBr_3$ [148].Using their valence band dispersion data, they were able to estimate an incredible Rashba parameter of $\alpha_0 \approx 7eV\mathring{A}$ in the low-temperature orthorhombic crystal phase and $\alpha_0 \approx 11eV\mathring{A}$ in the room temperature cubic phase. These are some of the strongest Rashba splittings reported and are indicative of very strong spin-orbit coupling in this material. Yaxin et al. reported similar results through an all-optical examination of the 2D perovskite $(C_6H_5C_2H_4NH_3)_2PbI_4$ using ultrafast transient and nonlinear optical spectroscopies [151]. The authors in this study found a giant Rashba splitting of ~ 40 meV and Rashba parameter of $\alpha_0 \approx 1.6\ eV\mathring{A}$ by studying the optical characteristics of excitons and free carriers generated by photoexcitations in thin films of this 2D hybrid perovskite.

However, there is some skepticism in the literature about the reported Rashba effects in hybrid perovskite materials. M. Sajedi et al. examined single crystals of $MAPbBr_3$ using ARPES in order to verify the findings of Niesner et al. [152]. Unfortunately, they were not able to replicate the giant spin splitting that was previously observed. Furthermore, they did not find *any* detectable Rashba effects either statically or dynamically in this material nor in a control sample of $CsPbBr_3$. Thus, the nature of Rashba effects in hybrid metal-halide perovskites is still in question and additional research is warranted to elucidate these conflicting findings.

3.2.1 Spin Lifetime at the Rashba Interface of NiFe/$MAPbBr_3$

The following section is adapted from published work in Ref. [153].

Observation of long spin lifetime in $MAPbBr_3$ single crystals at room temperature

Shijia Yang[1§], Eric Vetter[1§], Tonghui Wang[2], Aram Amassian[2], Dali Sun[1*]

[1]Department of Physics, North Carolina State University, Raleigh, NC 27606 USA

[2]Department of Materials Science and Engineering, North Carolina State University, Raleigh, NC 27606 USA

[§]These authors equally contributed to this work.

*Corresponding author: dsun4@ncsu.edu

Abstract

The emergence of hybrid metal halides (HMH) materials, such as the archetypal $CH_3NH_3PbBr_3$, provides an appealing material platform for solution-processed spintronic applications due to properties such as unprecedented large Rashba spin-splitting states and highly efficient spin-to-charge (StC) conversion efficiencies. Here we report the first study of StC conversion and spin relaxation time in $MAPbBr_3$ single crystals at room temperature using a spin pumping approach. Microwave frequency and power dependence of StC responses are both consistent with the spin pumping model, from which an inverse Rashba-Edelstein effect coherence length of up to ~ 30 picometers is obtained, highlighting a good StC conversion efficiency. The magnetic field angular dependence of StC is investigated and can be well-explained by the spin precession model under oblique magnetic field. A long spin relaxation time of up to ~190 picoseconds is obtained, which can be attributed to the surface Rashba state formed at the $MAPbBr_3$ interface. Our oblique Hanle effect by FMR-driven spin pumping

technique provides a reliable and sensitive tool for measuring the spin relaxation time in various solution processed HMH single crystals.

I. INTRODUCTION

The ability to transduce and manipulate an electric charge current into a corresponding spin current, and vice versa, is central to the field of spin-orbitronics [70], [154]. To this end, a great deal of research has focused on the generation [155]–[158], manipulation [159]–[163], and detection [71], [164] of the electron spin by means of spin-orbit coupling (SOC). Interconversion between electron spin and charge is typically accomplished via the spin Hall effect (SHE) and inverse spin Hall effect (ISHE), in which a three-dimensional (3D) charge current (j_c^{3D}) is injected into a nonmagnetic material with strong SOC, resulting in the generation of a transverse 3D spin current (j_s^{3D}) with orthogonal spin polarization direction S [165]. The efficiency of this conversion is proportional to the strength of the SOC in the nonmagnetic material, and is represented by the spin Hall angle (θ_{ISHE}), where $E_{ISHE} = \theta_{ISHE} J_s \times S$ and $\theta_{ISHE} = j_c^{3D}/j_s^{3D}$ [166]. Recently, a more efficient spin-to-charge (StC) conversion mechanism has also been discovered in strong SOC materials that lack inversion symmetry, known as the Rashba-Edelstein effect (REE) and inverse Rashba-Edelstein effect (IREE) [20], [76], [167]. This process occurs due to the formation of an interfacial ‘Rashba splitting state’, wherein spin degenerate bands are split in the presence of both strong SOC and the local breaking of inversion symmetry. Unlike the bulk 3D spin-to-charge conversion that occurs in ISHE, under the IREE a 2D charge current (j_c^{2D}) is generated when there is a sufficient presence of spin accumulation injected from an adjacent ferromagnet into the Rashba interface. In direct analogue to the ISHE conversion relation, the IREE process could be described by $j_c^{3D} \propto \lambda_{IREE}(\frac{2e}{\hbar}) j_s^{2D} \times S$ [168], wherein λ_{IREE} is the IREE ‘coherence length’ that determines the conversion efficiency through the relation $\lambda_{IREE} = j_c^{2D}/j_s^{3D} = \alpha_R \tau_p/\hbar$ where α_R is the Rashba coefficient and τ_p is the momentum scattering time at the Fermi contour [169]. These Rashba states have been studied in two-dimensional electron gas (2DEG) systems [72] and 3D topological insulators [24], showing great promise for next generation spin-to-charge transduction applications at room temperature.

The recent debut of spintronic studies using hybrid metal halide (HMH) materials [147], [149], [170]–[172], such as the prototypical material methylammonium lead bromide ($CH_3NH_3PbBr_3$, $MAPbBr_3$), have attracted an immense amount of research interest beyond their exciting optoelectronic properties for applications in solar cells [173]–[177], light-emitting diodes [178]–[180], lasers [181]–[183], and photodetectors [184]–[187] etc. They are remarkably defect tolerant, and the presence of heavy elements such as Pb in their inorganic framework leads to exceptionally strong SOC. In addition, they possess broad chemical tunability through chemical substitution of the halide anions and organic cations [188], allowing for synthetic control of the SOC strength, lattice constant, dimensionalities, bandgap, as well as emergent Rashba splitting states [148], [189]–[191]. These advantageous properties have made the family of HMHs a prime solution-processed material candidate for StC transduction applications. However, the exact description of the Rashba effect in these materials has remained elusive as most studies have utilized thin films whose polycrystalline nature [190], where inversion symmetry is broken not only at film surfaces but also at grain boundaries, complicates the data analysis [192].

One way to unravel the role of the Rashba state in HMH materials is through measurements of the spin lifetime. For this, it is best to study them in their single crystalline form as it is the most pristine embodiment of crystalline matter where properties are more directly related to the presence of SOC from the heavy elements or spin-momentum relations induced by the Rashba state, and less related to the presence of defects such as grain boundaries. A precise and reliable technique for measuring this parameter in HMH materials is the electrical 'Hanle' effect [169]. However, it is impractical to apply the traditional nonlocal magnetoresistance and electrical Hanle measurements in metals, which require solvent-based photo-/e-beam lithography procedures [193], to HMH materials. For this reason, no conventional electrical Hanle measurement has been demonstrated in HMHs at room temperature except for the ultrafast magneto-optical studies that is severely limited to cryogenic temperature operation for the clear demonstration of the Hanle precession in a handful of HMH materials [146]. Measuring the spin lifetime in such HMH materials without the aid of cryogenic environment is an extremely arduous endeavor. The electrical detection of the oblique Hanle effect by a ferromagnetic resonance-driven spin pumping technique — the change of StC conversion corresponds to a suppression of spin accumulation via spin precession under an oblique magnetic field [23] — enables us to obtain the crucial information about spin lifetime at room temperature and convincing proof of spin accumulation without involving destructive nanofabrication processes, and is particularly suitable for the HMH single crystal samples.

Here we demonstrate for the first time a complete spin pumping study on a macroscopic $MAPbBr_3$ single crystal using ferromagnetic resonance (FMR) and spin pumping techniques. The obtained StC signals change as a function of field orientation angle because of the spin-precession under the oblique magnetic field, enabling a first-order estimate of the spin lifetime in the $MAPbBr_3$ single crystal and providing strong evidence for the presence of a surface Rashba state. The application of oblique Hanle spin pumping provides a reliable metrology to study the spin lifetime in the family of solution processed HMH materials, which has been technically challenging for the conventional electrical Hanle measurement due to the inevitable conflicts between solution-based material preparation and nanofabrication procedures.

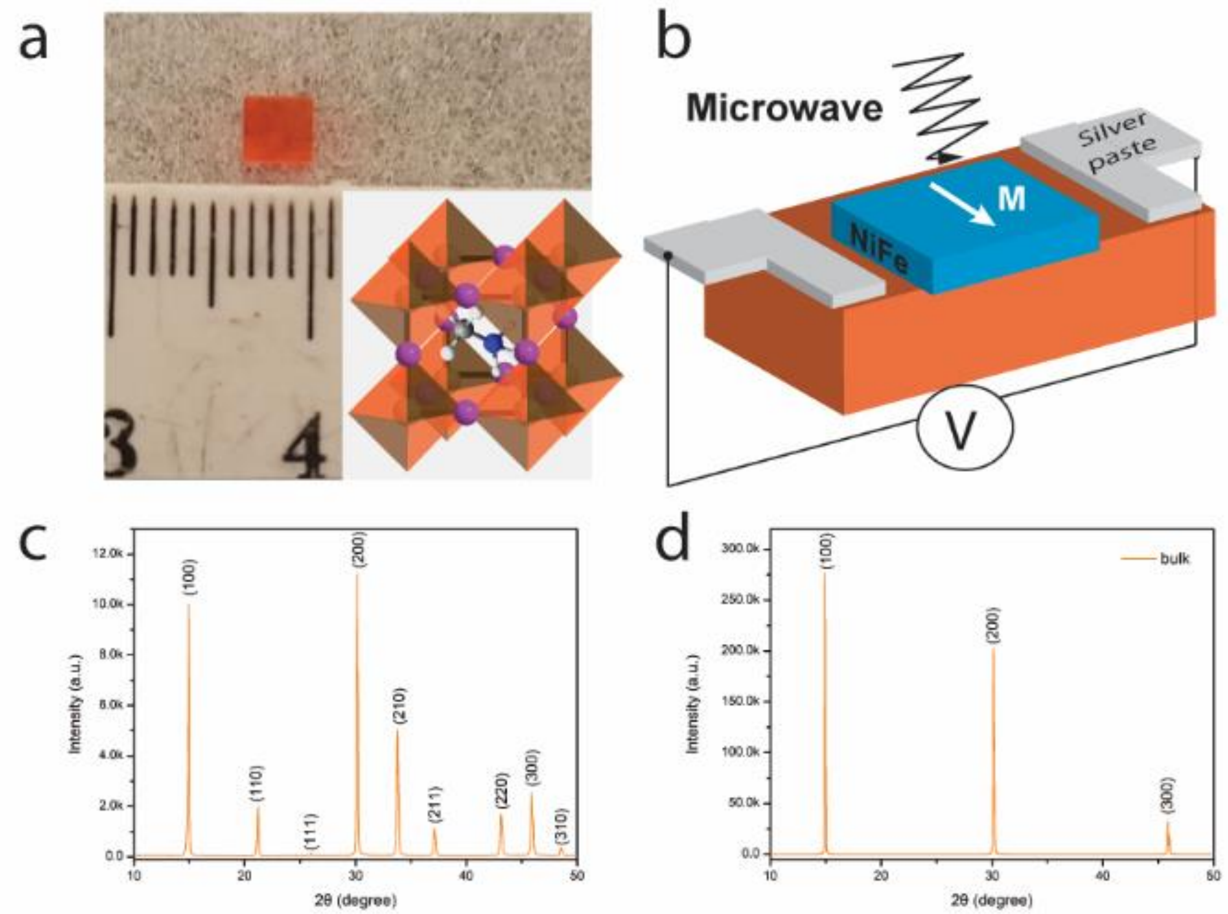

Figure 30. **(a)** Optical image of a $MAPbBr_3$ single crystal with ruler for scale. The sample size is approximately 3 x 3 x 2.5 mm. **(b)** Schematic illustration of the NiFe/$MAPbBr_3$ single crystal device used for spin pumping measurements, where M denotes the magnetization direction and V is the measured voltage. **(c)** and **(d)** X-Ray diffraction spectra obtained for $MAPbBr_3$ in both powder and bulk single crystal forms, respectively.

II. EXPERIMENTAL DETAILS

Figure 30a shows an optical image of the $MAPbBr_3$ single crystal used for spin pumping measurements. The crystal was grown using an inverse temperature crystallization technique

[194] and has approximate dimensions of 3 x 3 x 2.5 mm. 15 nm of $Ni_{81}Fe_{19}$ (99.99% purity, Angstrom Engineering) was deposited on the top surface of the single crystal using electron beam evaporation with a base chamber pressure of 1×10^{-7} Torr and deposition rate of 0.2 Å/s. Silver paste (Ted Pella, Inc.) was applied to the both sides of the crystal to provide electrical contacts for spin pumping voltage measurements, as shown schematically in **Figure 30b**. X-ray diffraction was used to check the phase purity of the prepared single crystal. **Figure 30c** and **30d** show the diffraction patterns obtained for both the single crystal and its powdered form, respectively, revealing a high quality single crystallinity.

Ferromagnetic resonance (FMR) was performed at room temperature from 2 to 16 GHz using a commercial NanOSC PhaseFMR spectrometer with a coplanar waveguide, while an GMW electromagnet was used for applying an external magnetic fields. For the spin pumping measurements, microwaves are generated by a Keysight X-Series Microwave Analog Signal Generator at an excitation frequency of 2-16 GHz and microwave power of 50 mW. A transverse dc voltage is electrically detected between two silver paste contacts at opposite ends of the single crystals, recorded by a Stanford SRS530 Lock-In Amplifier. Oblique Hanle effect measurements are performed by rotating the sample and coplanar waveguide with respect to the applied magnetic field using a precision goniometer, by which both the transverse dc voltage and FMR signal can be recorded simultaneously. All the measurements were taken at room temperature.

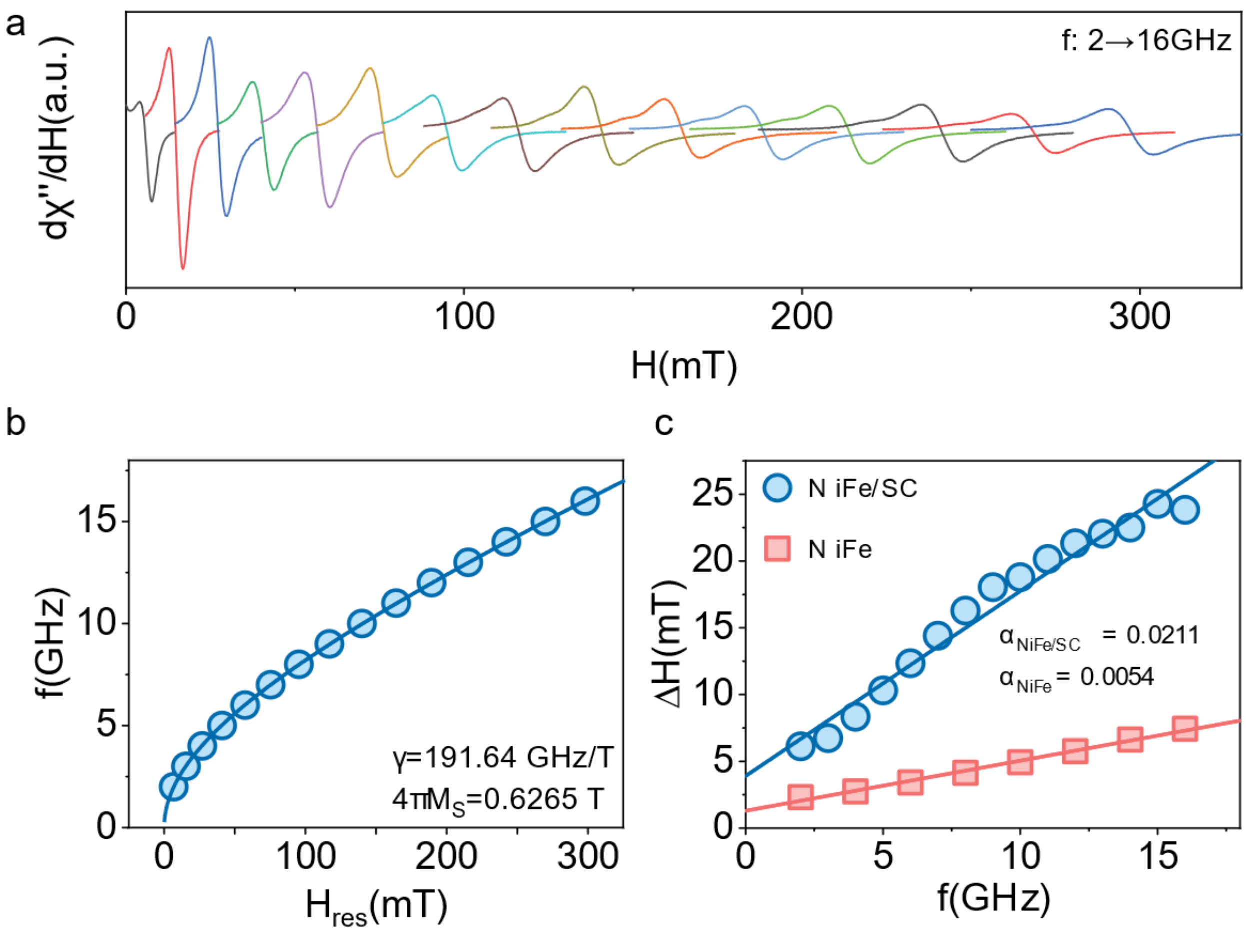

Figure 31. **(a)** FMR spectra of the NiFe/$MAPbBr_3$ bilayer obtained between 2 – 16 GHz. **(b)** Microwave frequency f plotted as a function of the resonant field H_{FMR}, where the solid curve represents a fit to the Kittel formula. **(c)** FMR linewidth plotted as a function of microwave frequency for the NiFe/$MAPbBr_3$ (blue) and NiFe reference sample (red).

III. RESULTS

Broadband ferromagnetic resonance and spin pumping

Figure 31a shows the typical FMR spectra obtained at different microwave frequencies for the $Ni_{81}Fe_{19}$/$MAPbBr_3$ single crystal device, from which values for α, the damping factor, γ, the gyromagnetic ratio, and M_s, the saturation magnetization, are derived. M_s and γ are obtained from the H_{FMR} versus f plots shown in **Figure 31b**, by fitting to the Kittel equation: $(\frac{2\pi f}{\gamma})^2 = H_{FMR}(H_{FMR} + 4\pi M_s)$ [30], where H_{FMR} is the resonant field. Values for $4\pi M_s$ and γ for a bare $Ni_{81}Fe_{19}$ reference sample deposited on a glass substrate are found to be 0.627 T and 191.64 GHz/T, respectively, which are consistent with those reported in the literature [15]. Damping factors are extracted using the relation, $\alpha = \frac{\sqrt{3}\gamma}{4\pi f}\Delta H + H_0$, where ΔH is the FMR linewidth (HWHM) and f is the microwave frequency. H_0 is the frequency-independent linewidth contribution arising from inhomogeneities in the ferromagnetic film and single crystal surface. The intrinsic damping parameter, α_0, for the bare NiFe reference sample is found to be 5.4×10^{-3}, while the damping parameter of the $Ni_{81}Fe_{19}/MAPbBr_3$ is found to be 2.1×10^{-2}, as shown in **Figure 31c**.

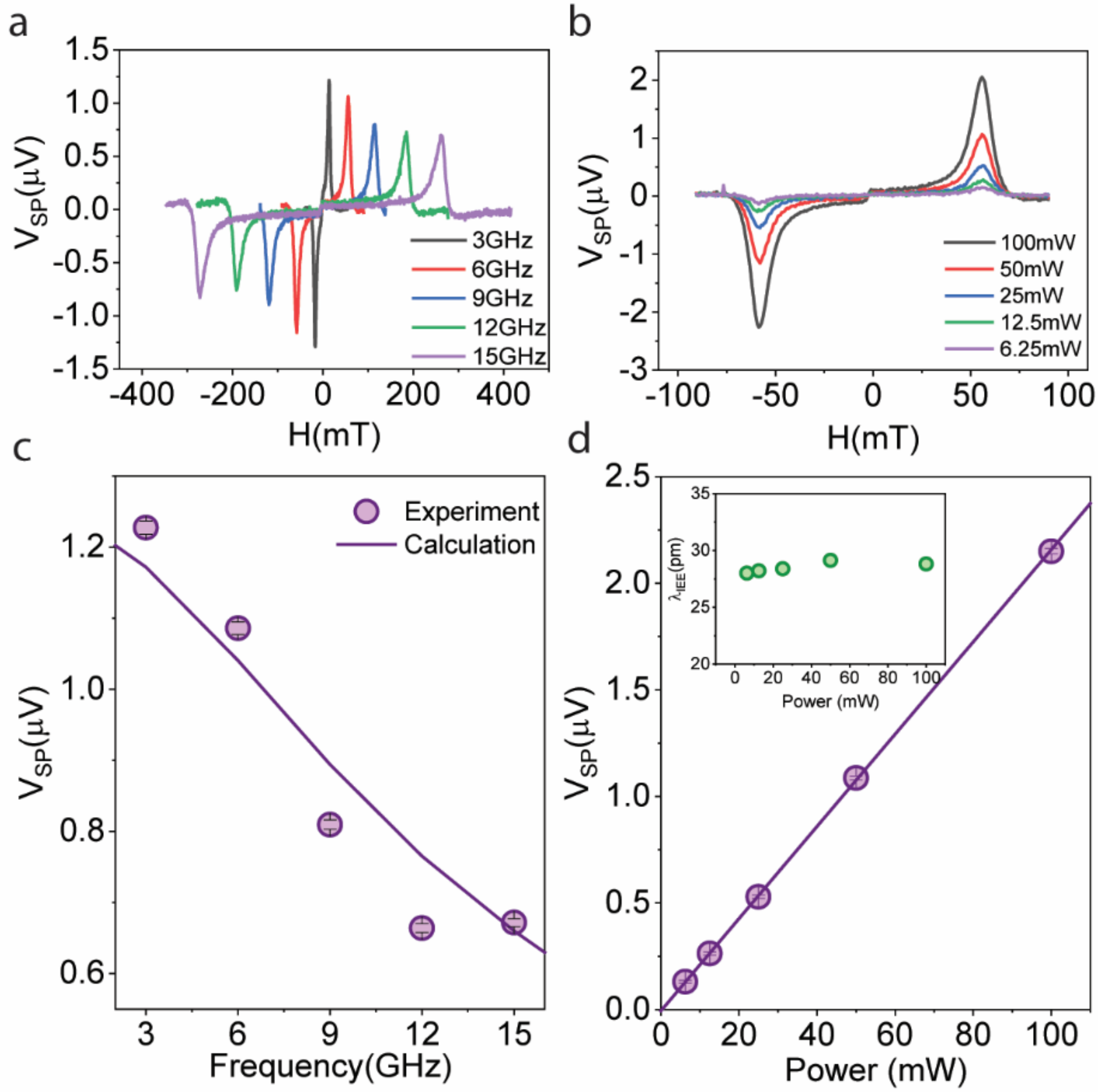

Figure 32. **(a)** Spin pumping voltage V_{SP} measured as a function of external magnetic field H for different microwave frequencies **(b)** V_{SP} measured as a function of H for different microwave excitation powers at a frequency of 6 GHz. **(c)** Data (symbols) and theoretical fit (line) for V_{SP} measured as a function of microwave frequency. **(d)** Data (symbols) and theoretical fit (line) for V_{SP} measured as a function of microwave power. The inset shows the calculated IREE length vs. microwave power.

When an in-plane magnetic field is applied, the vertical spin current density (j_s^{3D}) that is injected into the NiFe/$MAPbBr_3$ interface under the ferromagnetic resonance may be calculated via the relation [15]:

$$j_s^{3D}(\varphi_M = 0) = \frac{g_{eff}^{\downarrow\uparrow}\gamma^2 h_{rf}^2 \hbar}{8\pi\alpha_{eff}^2}\left[\frac{\mu_0 M_{eff}\gamma cos^2(\varphi_M)+\sqrt{(\mu_0 M_{eff}\gamma)^2 cos^2(\varphi_M)+4\omega^2}}{(\mu_0 M_{eff}\gamma)^2 cos^2(\varphi_M)+4\omega^2}\right]\cdot\frac{2e}{\hbar} \tag{1}$$

where $g_{eff}^{\downarrow\uparrow}$ is the spin mixing conductance at the interface determined by $\Delta\alpha = \frac{\gamma\hbar}{4\pi M_s d_F} g_{eff}^{\downarrow\uparrow}$ where d_F is the thickness of the ferromagnetic layer, h_{rf} is the microwave field, $\mu_0 M_{eff}$ is the effective saturation magnetization of NiFe, $\omega = 2\pi f$, e is the electron charge, and ħ is the Planck constant.

Spin pumping measurements are performed at room temperature using the same experimental setup used for the FMR measurement. The voltage generated across the $Ni_{81}Fe_{19}$/$MAPbBr_3$ device is measured as a function of applied magnetic field at different microwave frequencies and microwave powers, as shown in **Figure 32a** and **32b,** respectively. The obtained dc voltage signal can be decomposed into two parts, a symmetric and an antisymmetric voltage component given by [71]: $V(H) = V_0 + V_{Sym}\frac{\Delta H^2}{(H-H_{FMR})^2+\Delta H^2} - V_{Asym}\frac{\Delta H(H-H_{FMR})}{(H-H_{FMR})^2+\Delta H^2}$, where V_{Sym} is the spin pumping voltage generated from the StC conversion and V_{Asym} is the Anomalous Hall effect (AHE) contribution from the $Ni_{81}Fe_{19}$ layer [71]. Flipping of the voltage polarity upon the reversal of the applied magnetic field from + H_{res} to – H_{res} provides a strong evidence that the signal is indeed originated from the spin pumping process rather than that from the heating induced artifact which is magnetic field independent[55]. Here, we take the average of V_{Sym} for $+H_{FMR}$ and $–H_{FMR}$ as the actual V_{SP}, where $V_{SP} = [V_{Sym}(+H_{FMR}) - V_{Sym}(-H_{FMR})]/2$. **Figure 32c** shows the microwave frequency dependence of

V_{SP} can be fitted with the equation $V_{SP} \propto [(M_{eff}\gamma)^2 + (4\pi f)^2]^{-1/2}$, in good agreement with spin pumping model [23]. The decrease in the magnitude of V_{SP} with increasing microwave excitation frequency further proves that the observed V_{sp} signal does not stem from heating induced artifact, but rather the actual spin pumping induced signals. **Figure 32d** shows the linear dependence of V_{SP} with microwave power, consistent with the spin pumping model in the linear-response regime [195].

Figure 33. **(a)** Schematic illustrations of the NiFe/$MAPbBr_3$ bilayer during spin pumping experiments when the external field H is applied out-of-plane by an angle θ. *M* and V_{sp} denote the magnetization vector for NiFe and spin pumping voltage, respectively. **(b)** FMR spectra normalized by resonant field plotted for different magnetic field angles θ. **(c)** Spin pumping voltage V_{SP} normalized by resonant field plotted for different magnetic field angles θ. **(d)** H_{FMR} plotted as a function of θ **(e)** Magnetization angle φ plotted as a function of θ according to the Landau–Lifshitz–Gilbert equation with the measured H_{FMR} values. **(f)** V_{SP} plotted as a function of θ. Fit curves with four different spin-relaxation times (τ_{sf}) are shown using Eq. (4). The solid circles represent experimental data while the solid curve represents the best fit obtained with τ_{sf} = 189 ps. The inset shows the same fitting applied to a sample of NiFe (15 nm)/SiO_2 where τ_{sf} ~ 18 ps.

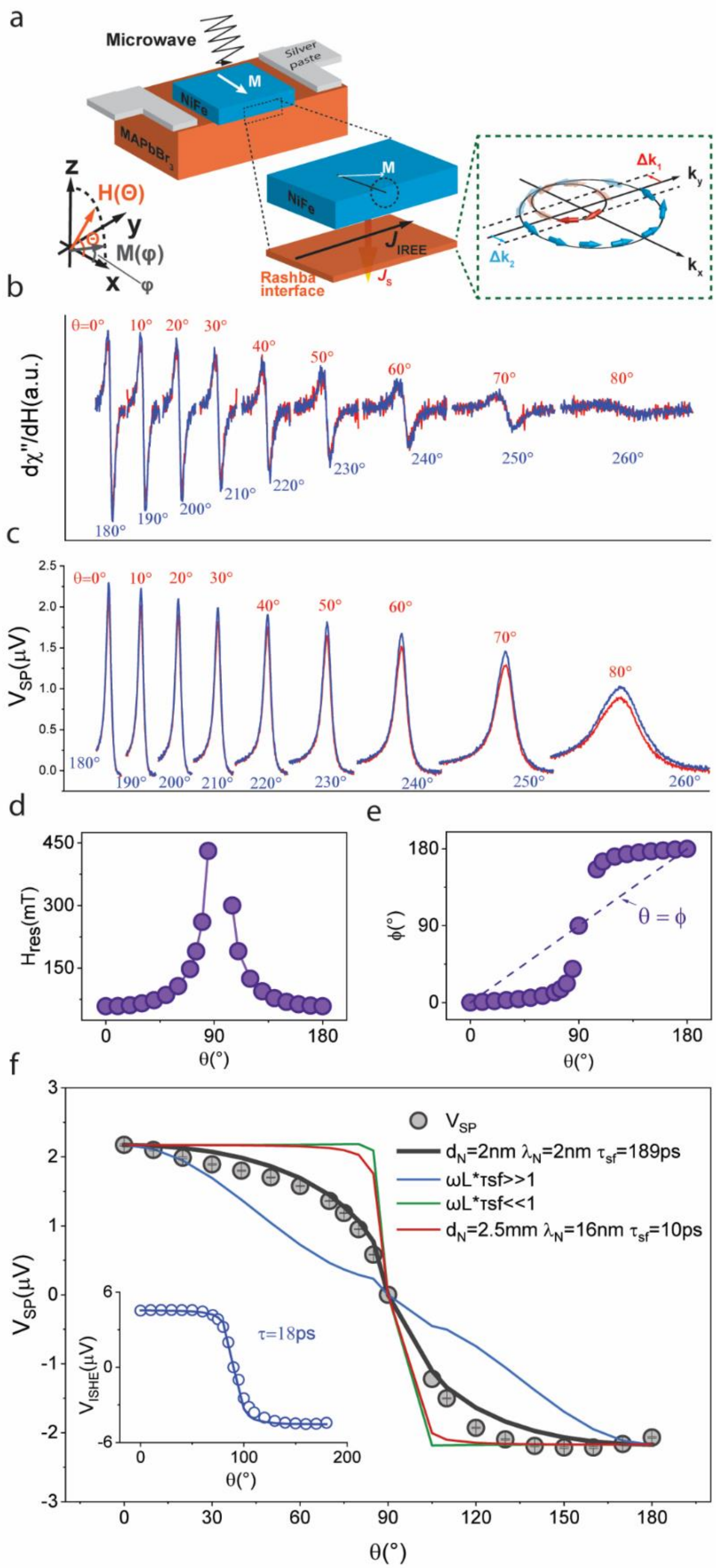
a
Microwave
Silver paste
NiFe
M
MAPbBr3
z
H(Θ)
y
Θ
M(φ)
x
φ
NiFe
M
J_IREE
Rashba interface
J_s
Δk1
k_y
Δk2
k_x
b
dχ"/dH(a.u.)
θ=0°
10°
20°
30°
40°
50°
60°
70°
80°
180°
190°
200°
210°
220°
230°
240°
250°
260°
c
V_SP(μV)
θ=0°
10°
20°
30°
40°
50°
60°
70°
80°
180°
190°
200°
210°
220°
230°
240°
250°
260°
d
H_res(mT)
θ(°)
e
ϕ(°)
θ = ϕ
θ(°)
f
V_SP
d_N=2nm λ_N=2nm τ_sf=189ps
ωL*τsf>>1
ωL*τsf<<1
d_N=2.5mm λ_N=16nm τ_sf=10ps
V_SP(μV)
θ(°)
τ=18ps
V_ISHE(μV)
θ(°)

Oblique Hanle spin precession

We have conducted both field angular dependent FMR and spin pumping measurements, namely performing the spin pumping measurement when applied external magnetic field, H is applied oblique to the film plane by an angle θ_H from 0° to 180°, as shown schematically in **Figure 33a**. Under the oblique magnetic field, the relation between the external magnetic field angle θ_H and the angle of the magnetization–precession axis φ_M is calculated using the Landau–Lifshitz–Gilbert equation, which can be described by [23], [196]:

$$2H_{FMR} sin(\theta_H - \varphi_M) + 4\pi M_{eff} \sin 2\varphi_M = 0 \quad (2)$$

$$\left(\frac{\omega}{r}\right)^2 = \left[H_{FMR} \cos(\theta_H - \varphi_M) - 4\pi M_{eff} \cos(2\varphi_M)\right] \times \left[H_{FMR} \cos(\theta_H - \varphi_M) - 4\pi M_{eff} cos^2(\varphi_M)\right] \quad (3)$$

where H_{FMR} is the applied magnetic field strength under the resonance condition. **Figure 33b** and **33c** presents the obtained angular dependence of the FMR and V_{SP} signals, respectively. The resonant fields, H_{FMR}, from the FMR spectra are plotted as a function of θ_H in **Figure 33d**. The relation between θ_H and φ_M calculated from Eq. (2) with the measured value of H_{FMR} is shown in **Figure 33e** [23].

The oblique magnetization M(φ_M) of the NiFe film at the ferromagnetic resonance injects the pure spin current $S(t)$ into the $MAPbBr_3$ layer of which spin polarization direction follows the oblique magnetization direction (**Figure 33a**). Due to the misalignment between θ_H and φ_M, the injected $S(t)$ in the $MAPbBr_3$ layer under the oblique static external magnetic field precesses and results in a decrease of transverse IREE voltage because of the suppressed spin accumulation via spin precession and dephasing, i.e., the Hanle effect [197], [198]. By increasing the angle of the applied magnetic field, the in-plane component of $S(t)$ senses a larger out-of-plane field strength that further suppress the spin accumulation, giving rise to a typical characteristic of field angular dependence of the spin pumping voltage [23] if the spin relaxation time, τ_{sf} is considerably comparable to or larger than the Larmor precession time $1/\omega_L$ ($\omega_L = g_L\mu_B(\mu_0 H)/\hbar$ is the Larmor frequency under the oblique magnetic field). The spin pumping voltage, V_{SP}, is plotted as a function of out-of-plane angle, θ_H in **Figure 33f**, allowing us to determine the spin lifetime, τ_{sf}, in the $MAPbBr_3$ layer using the Hanle precession model with both ISHE and IREE contributions [23], [199]:

$$V_{SP} \propto j_s^{3D}(\varphi_M)(\lambda_{IREE} + \theta_{ISHE}\lambda_N)[cos\theta\cos(\theta - \varphi)\int_0^{d_N} e^{-x/\lambda_N}dx + sin\theta\sin(\theta - \varphi)\int_0^{d_N} Re[e^{-\frac{x}{\lambda_\omega}}]dx] \quad (4)$$

where $j_s^{3D}(\varphi_M \neq 0)$ is the angular dependent injected spin current density at the interface under the oblique FMR condition given by Eq. (1) [15], d_N is the thickness of $MAPbBr_3$ single crystal (i.e., 2.5mm) for the bulk ISHE contribution or the nominal thickness of the Rashba surface state (taken as 2 nm) [200], λ_N is the spin diffusion length in the $MAPbBr_3$ crystal, and $\lambda_\omega = \frac{\lambda_N}{\sqrt{1+i\gamma H_{res}\tau_{sf}}}$[51].

It is noteworthy that Eq. (4) was originally derived from an equivalent circuit model for the interpretation of field angular dependent ISHE measurements [23]. For simplicity, here both bulk ISHE contribution and surface Rashba induced IREE contribution share the same Hanle precession model but with different nominal thickness and spin diffusion length parameters. The reasoning is that in ISHE, the entire thickness of the NM (i.e., d_N can be up to 2.5 mm for the thickness of single crystal) contributes to the generated transverse dc voltage: the spin current at a certain depth into the material is related to the spin diffusion length, resulting in a gradual increase of StC conversion when the thickness increases until it saturates [201]. In contrast, at a Rashba surface state, the StC conversion occurs with a constant conversion efficiency only at the surface state as detailed in previous reports [201], [202]. Thus, a constant StC conversion coefficient in the form of IREE coherence length will be assumed. Specifically, at the surface state, the produced 3D spin diffusion will be limited at the 2D surface state, in which the spin diffusion length is simply equivalent to the value of the nominal thickness of the surface state as used in other topological insulator systems [203], i.e., d_N (surface) $\approx \lambda_N$(surface) $= 2\ nm$.

Four fit curves using different spin-relaxation times (τ_{sf}) are shown in **Figure 33f** to illustrate how the fitted model curve changes with $\omega\tau_{sf} \ll 1$, $\omega\tau_{sf} \gg 1$, IREE contribution, and only bulk ISHE contribution with expected low spin lifetime at room temperature ($\tau_{sf}(bulk) < 10\ ps$ [23]), respectively. The best fit curve with produced with τ_{sf} = 189 ps that determines that the spin lifetime for the $Ni_{81}Fe_{19}/MAPbBr_3$ single crystal with only IREE contribution. For comparison, a similar measurement for the $NiFe/SiO_2$ control sample was performed (the inset of **Figure 33f**). A much smaller spin lifetime of τ_{sf} = 18 ps is obtained in stark contrast to the long spin lifetime observed in the $MAPbBr_3$ sample, indicating that the magnetoresistance artifacts from the NiFe layer do not play a dominant role in our measurement.

IV. DISCUSSION

Bulk $MAPbBr_3$ forms a disordered cubic structure at room temperature with an average space group symmetry of $Pm\bar{3}m$. This centrosymmetric structure possesses inversion symmetry, and thus should lack any bulk Rashba type effects. However, at the surface or interface this inversion symmetry is necessarily broken and therefore allows for the formation of a surface Rashba state. Indeed, it has been proposed that the giant Rashba splitting previously observed in $MAPbBr_3$ stems from this surface state and not the bulk [149], [204], [205] and recently experimentally proven in the MAPbrBr3 polycrystalline thin film [201]. It is thus tremendously advantageous to utilize single crystals in the analysis of the surface Rashba state, where a single material surface may be isolated and probed and the effects of defects such as grain boundaries is minimized.

In our spin pumping experiments, we use microwave excitation of the NiFe thin film at its ferromagnetic resonance for the generation of a 3D spin current that is subsequently injected into the adjacent $MAPbBr_3$ single crystal. If the predicted surface Rashba state is present at this interface, the spin current may be converted into a corresponding 2D charge current by the IREE process. For FMR measurements, this should manifest as spin current dissipation across interface, namely spin sink behavior resulting in an increase in the damping factor of the bilayer with respect to the isolated ferromagnetic film. This expected phenomenon is confirmed in **Figure 31c**, where we see that the damping factor obtained for NiFe/$MAPbBr_3$ (2.1×10^{-2}) is almost four times larger than that of the bare NiFe film (5.4×10^{-3}). This large increase in damping for the bilayer system is indicative of the presence of a strong spin to charge conversion process, which is further reinforced by IREE measurements. The transverse charge current generated at the interface in response to the injected spin current can be estimated by the relation $j_c^{2D} = V_{SP}/Rl$ where l is the length of the device (3 mm) and R is the total device resistance calculated as $R = \frac{1}{[\sigma_{MAPbBr3} d_{MAPbBr3} + \sigma_{NiFe} d_{NiFe}]}$, where $\sigma_{MAPbBr3}$ is the conductivity of the $MAPbBr_3$ single crystal, σ_{NiFe} (1.17×10^{-5} Ω·cm) is the conductivity of the NiFe layer, $d_{MAPbBr3}$ is the thickness of the $MAPbBr_3$ single crystal and d_{NiFe} (15nm) is the thickness of the NiFe layer. As described by the relation $\lambda_{IREE} = {j_c^{2D}}\big/{j_s^{3D}}$, by comparing the j_s^{3D} obtained from FMR and j_c^{2D}obtained from IREE, we may extract the IREE coherence length which we find to be $\lambda_{IREE} = 28.5\ pm$ that remains constant as a function of microwave power (inset of **Figure 32d**). This value is comparable to the coherence lengths found in YIG/Bi_2Se_3 (~35 pm) and

$NiFe/Bi_2Se_3$ (60 pm), although it is much smaller than those found in systems such as Bi/Ag (100-400 pm) and α-Sn (2100 pm) [76], [113], [168], [206].

To provide further evidence for the presence of an interfacial Rashba state in our $NiFe/MAPbBr_3$ bilayer, we directly determine the spin lifetime τ_{sf} and compare it to other systems. We accomplish this by performing both FMR and IREE measurements as a function of external magnetic field angle θ. By plotting the obtained spin pumping voltage as a function of θ and fitting the result to Equation 2, we are able to extract a numerical value for the spin carrier relaxation time at the interface. The spin relaxation time of τ_{sf} = 189 ps obtained for the $NiFe/MAPbBr_3$ system is much larger than that in the NiFe sample (SiO_2/NiFe) alone, where τ_{sf} = 18 ps (see the inset of **Figure 33f**), or even in the NiFe/Pt bilayer sample, where τ_{sf} = 33 ps. Whereas a larger spin relaxation time in the NiFe film is probably ascribed to the self-ISHE response originated from the potential surface state formed between the NiFe and SiO_2 substrate (τ_{sf} (NiFe only)= 0.025 ps would be expected for the pure NiFe film [23]), the results from these control samples further confirm that the obtained transverse voltage signals in the $NiFe/MAPbBr_3$ is unlikely originated from the self-ISHE response from the NiFe film or from spin-rectification effects [207]–[209].

The large increase in spin relaxation time for $NiFe/MAPbBr_3$ can be attributed to the presence of a surface Rashba state formed at the $NiFe/MAPbBr_3$ interface where the breaking of inversion symmetry leads to the formation of two degenerate spin contours with opposite helicity. A spin carrier injected into this environment is unable to undergo rapid spin relaxation when a strong correlation between momentum and spin is locked within these helical contours. In contrast to a usually short spin lifetime if the spin flip increases with the scattering rate increasing following the Elliott-Yafet mechanism [3], a long spin lifetime would be anticipated if the Rashba state dominates the StC interconversion where the spin lifeime is likely to be inversely proportional to the momentum scattering time (τ_p) via the D'yakonov-Perel mechanism [210]. Therefore, the spin lifetime in HMHs obtained by both the FMR-driven spin injection is much longer than the momentum relaxation time τ_p ~0.5 fs [211]. This comparison also provides additional support for the presence of an interfacial Rashba state, where we would expect similar relaxation times if the signal were coming from a pure ISHE process. We note that this spin relaxation time is also much longer than what would be expected if the relaxation process was dominated by SOC from Pb atoms in the perovskite's inorganic framework, where ultrafast optical measurements have estimated values of $\tau_{sf} < 4\ ps$ [147], [200].

We are unaware of any other reports on the spin lifetime in $MAPbBr_3$ single crystals at room temperature with which we could compare our experimentally obtained value of τ_{sf} = 189 ps. However, there have been some reports on polycrystalline $MAPbBr_3$ thin films measured at low temperature as well as several recent theoretical studies on $MAPbBr_3$ and $MAPbI_3$ single crystals [149], [204], [205], [212], [213]. R. Wang et al. used partial circularly polarized photoluminescence (CPL) to measure spin lifetime via the optical Hanle effect in $MAPbBr_3$ thin films at low temperature, with measured relaxation times of τ_{sf} = 240 ps at 77 K that reduces by an order of magnitude at 110K [213]. J. Wang et al. similarly measured optical Hanle responses in $MAPbBr_3$ thin films at low temperature using CPL, finding that τ_{sf} = 491 ps at 10K [144]. In addition, they measured electrical Hanle responses for the thin film in a spin valve configuration to obtain a spin relaxation time of τ_{sf} = 936 ps at 10 K [144]. The large reduction in spin lifetime with increasing temperature has also been considered theoretically [205], where it is shown that τ_{sf} may be reduced by over two orders of magnitude between 10-300 K. Thus, our obtained value of τ_{sf} = 189 ps for $MAPbBr_3$ at 300 K is eminently remarkable. Please note this estimated value could be larger since the dynamical spin injection method used in this paper, the spin lifetime may be reduced by coupling of the spins at the surface of the $MAPbBr_3$ single crystal to the adjacent NiFe layer [214], [215].

By considering the presence of a surface Rashba state where the signals measured during spin pumping experiments will be coming from the dominant IREE process, the corresponding Rashba coefficient α_R could be calculated by combining the obtained IREE length ($\lambda_{IREE} = 28.5\ pm$) with a previously calculated value for the spin-momentum scattering time at the Fermi contour ($\tau_p \approx 0.5\ fs$) [214] using the relation $\lambda_{IREE} = \alpha_R \tau_p / \hbar$. Using these parameters, we derive a value for the Rashba coefficient of $\alpha_R = 0.34\ eV \cdot \text{Å}$. This value is comparable in magnitude to the $\alpha_R = 0.33\ eV \cdot \text{Å}$ obtained from previous spin pumping measurements performed on polycrystalline $MAPbBr_3$ films measured at room temperature [201], although is s lower than the massive $\alpha_R = 11\ eV \cdot \text{Å}$ previously reported based on ARPES measurements of $MAPbBr_3$ single crystals [148].

V. CONCLUSION

In summary, we report the first spin pumping study on the NiFe/$MAPbBr_3$ single crystal device at room temperature. The obtained IREE coherence length $\lambda_{IREE} = 28.5\ pm$ is comparable in order of magnitude to IREE lengths measured in several topological insulator and 2D systems by similar spin pumping approaches [168], [203], [216]–[218]. By measuring both FMR and spin pumping signals as a function of out-of-plane external magnetic field angle, an unprecedentedly long spin lifetime τ_{sf} = 189 ps at room temperature is obtained, exceeding the presumable short spin lifetime induced by heavy elements in HMH materials. The enhanced spin lifetime is attributed to the presence of an interfacial Rashba state at the NiFe/$MAPbBr_3$ interface. We hope that these results will initiate additional studies of interfacial Rashba effects in various HMH single crystals for future solution-processed spin-to-charge transduction applications.

Acknowledgments

S.Y., E.V. and D.S. are grateful for support from the startup funds provided by North Carolina State University and NSF Grant No. ECCS-1933297. Sample preparation and characterization were partially supported by NC State University-Nagoya Research Collaboration grant.

Author Contribution

D.S. and A.A. conceived this study and the experiment. S.Y. and E.V. fabricated the devices, measured the FMR, spin pumping, oblique Hanle effect, and calibrated rf field. T.W. provided the single crystals. E.V., S.Y., and D.S. wrote the text. D.S. and A.A. were responsible for the project planning and group managing. All authors discussed the results, worked on data analysis and manuscript preparation. The authors declare no competing financial interests.

Chapter 4

Conclusion and Future Outlook

This thesis examined spintronics devices comprised of organic, inorganic, and hybrid semiconductor materials. Each type of semiconductor possesses unique spin-related properties that can be advantageous or deleterious depending on the device in which it is being integrated and its end-use application. The future outlook for these three classes of semiconductors with respect to their spintronic utility will be briefly discussed here.

Organic semiconductors are incredibly promising materials for spintronics in the long term due to their almost limitless chemical and structural versatility. However, in the short term there are still many issues surrounding their practical use at the device level. The disordered nature of organic solids and their microstructural sensitivity to processing conditions makes it difficult to pin down the exact material properties that produce certain device behaviors. Spin-orbit coupling in these materials is also much different than that in crystalline solids, and highly dependent on structural conformation due to the key role of molecular orbital orientation. Furthermore, carrier mobility is typically quite low in these materials as compared with their inorganic counterparts. Promising progress has been made, for example by the groups of Zhi-Gang Yu and Henning Sirringhaus, in elucidating the cause-and-effect relation of polymer properties on spin transport and relaxation, which may pave the way for their use in the coming years. Spin transport in planar, highly doped conjugated polymer semiconductors is particularly promising given their ability to achieve very long spin diffusion lengths (> 1μm) with fast transit times. Once the fundamentals of spin behaviors in these carbon-based semiconductors are better understood, their favorable processability, mechanical flexibility, and synthetic chemical versatility make them prime candidates for future spintronics devices.

Inorganic semiconductors have enjoyed unparalleled success in electronic devices over the past few decades, and it is highly likely that this will be mirrored in the realm of spintronics in the short term. Spin-orbit coupling, spin dynamics and spin transport have been relatively well studied in this class of semiconductor and there is an extensive body of research related to material properties and synthesis as a function of their commercial use. One of the primary barriers with inorganic semiconductor spintronics historically has been the issue of impedance mismatching between the semiconductor and ferromagnetic contacts preventing efficient spin injection. However, the advent of microwave-induced spin pumping, ultrafast laser and optical excitation methods now allow for highly efficient spin injection into these materials. Precise control over material interfaces in relation to two-dimensional carrier gases, quantum well heterostructures, and other Rashba-active structures with spin-dependent band structures enables exciting spintronics devices that may be tuned by electric and optical gating methods for advanced functionalities. In particular, spintronic THz emitters based on inorganic semiconductors are likely to see increased research interest as they stand to offer a high degree of control over ultrafast spin-to-charge conversion and waveform emission, with key applications in ultrafast computing, high bandwidth communications, and non-destructive examination.

Hybrid organic-inorganic perovskite semiconductors are in an early stage of development for spintronics applications, but hold tremendous promise due to their intermediate properties between pure organic and inorganic semiconductors. They are synthetically versatile, allowing for the facile substitution of both organic ligands and ions within their metal halide framework for the variation of material properties. They also can be synthesized through low-temperature, solution-based processing, which is tremendously advantageous for commercial adoption, although their primary dependence on Pb as the metal cation can be problematic. In terms of spin properties, hybrid perovskite semiconductors typically exhibit relatively long spin diffusion lengths and coherence times given the strong spin-orbit coupling of their framework elements. Additionally, many compounds within this material class exhibit spin-dependent band structures and Rashba states that give rise to highly efficient spin-to-charge conversion. Many of the same properties that have motivated the use of these materials in solar cell applications, such as synthetic bandgap control and optical activity, may be considered advantages in spintronics as well. While perhaps not as immediately applicable to device integration in the short term as inorganic semiconductors stand to be, hybrid perovskites offer a great degree of flexibility and favorable material properties that ensure their ultimate adoption in spintronics in the near future, especially for spin-optoelectronics.

Much work still needs to be done before semiconductor-based spintronics reach their full potential, though the ideas and results presented here in this thesis offer a small step in the right direction. Further development in the understanding of spin dynamics, spin transport, and spin-to-charge conversion in semiconductor materials will be crucial towards their successful implementation in spintronics and enable the next generation of spin-based devices.

REFERENCES

[1] N. Dombey, "The Nobel prize in physics," *Nature*, vol. 300, no. 5888, pp. 106–107, 1982.

[2] M. Julliere, "Tunneling between ferromagnetic films," *Phys. Lett. A*, vol. 54, no. 3, pp. 225–226, Sep. 1975.

[3] I. Žutić, J. Fabian, and S. Das Sarma, "Spintronics: Fundamentals and applications," *Rev. Mod. Phys.*, vol. 76, no. 2, pp. 323–410, Apr. 2004.

[4] H. M. Shen, L. Hu, and X. Fu, "Integrated giant magnetoresistance technology for approachable weak biomagnetic signal detections," *Sensors (Switzerland)*, vol. 18, no. 1. 2018.

[5] M. N. Baibich *et al.*, "Giant magnetoresistance of (001)Fe/(001)Cr magnetic superlattices," *Phys. Rev. Lett.*, vol. 61, no. 21, pp. 2472–2475, Nov. 1988.

[6] G. Binasch, P. Grünberg, F. Saurenbach, and W. Zinn, "Enhanced magnetoresistance in layered magnetic structures with antiferromagnetic interlayer exchange," *Phys. Rev. B*, vol. 39, no. 7, pp. 4828–4830, Mar. 1989.

[7] B. Huang *et al.*, "Layer-dependent Ferromagnetism in a van der Waals Crystal down to the Monolayer Limit," *Nat. Publ. Gr.*, vol. submitted, no. 7657, pp. 270–273, 2017.

[8] C. Day, "Discoverers of giant magnetoresistance win this year's physics nobel," *Phys. Today*, vol. 60, no. 12, pp. 12–14, Dec. 2007.

[9] M. I. Dyakonov and V. I. Perel, "Current-induced spin orientation of electrons in semiconductors," *Phys. Lett. A*, vol. 35, no. 6, pp. 459–460, Jul. 1971.

[10] J. E. Hirsch, "Spin hall effect," *Phys. Rev. Lett.*, vol. 83, no. 9, pp. 1834–1837, Aug. 1999.

[11] S. Zhang, "Spin Hall effect in the presence of spin diffusion," *Phys. Rev. Lett.*, vol. 85, no. 2, pp. 393–396, Jul. 2000.

[12] N. S. A. and M. I. Dyakonov, “Current due to non-homogeneous spin orientation in semiconductors,” *Sov. Phys. JETP Lett.*, vol. 35, no. 4, p. 196, 1983.

[13] A. Bakun, B. Zakharchenya, A. Rogachev, M. Tkachuk, and V. Fleĭsher, “Observation of a surface photocurrent caused by optical orientation of electrons in a semiconductor,” *Sov. J. Exp. Theor. Phys. Lett.*, vol. 40, p. 1293, 1984.

[14] M. N. Tkachuk, B. P. Zakharchenya, and V. G. Fleisher, “Resonant photovoltaic effect in the NMR of nuclei in a semiconductor lattice,” *Sov. Phys. JETP Lett.*, vol. 44, p. 59, 1986.

[15] K. Ando *et al.*, “Inverse spin-Hall effect induced by spin pumping in metallic system,” *J. Appl. Phys.*, vol. 109, no. 10, 2011.

[16] G. Vignale, “Ten years of spin hall effect,” in *Journal of Superconductivity and Novel Magnetism*, 2010, vol. 23, no. 1, pp. 3–10.

[17] Y. K. Kato, R. C. Myers, A. C. Gossard, and D. D. Awschalom, “Observation of the spin hall effect in semiconductors,” *Science (80-.).*, vol. 306, no. 5703, pp. 1910–1913, Dec. 2004.

[18] J. Wunderlich, B. Kaestner, J. Sinova, and T. Jungwirth, “Experimental observation of the spin-hall effect in a two-dimensional spin-orbit coupled semiconductor system,” *Phys. Rev. Lett.*, vol. 94, no. 4, p. 047204, Feb. 2005.

[19] V. M. Edelstein, “Spin polarization of conduction electrons induced by electric current in two-dimensional asymmetric electron systems,” *Solid State Commun.*, vol. 73, no. 3, pp. 233–235, Jan. 1990.

[20] G. Bihlmayer, O. Rader, and R. Winkler, “Focus on the Rashba effect,” *New J. Phys.*, vol. 17, no. 5, p. 050202, May 2015.

[21] D. C. Vaz, A. Barthélémy, and M. Bibes, “Oxide spin-orbitronics: New routes towards

low-power electrical control of magnetization in oxide heterostructures," *Japanese Journal of Applied Physics*, vol. 57, no. 9. Japan Society of Applied Physics, p. 0902A4, 01-Sep-2018.

[22] G. Dresselhaus, "Spin-orbit coupling effects in zinc blende structures," *Phys. Rev.*, vol. 100, no. 2, pp. 580–586, Oct. 1955.

[23] K. Ando and E. Saitoh, "Observation of the inverse spin Hall effect in silicon," *Nat. Commun.*, vol. 3, pp. 626–629, 2012.

[24] R. Sun *et al.*, "Large Tunable Spin-to-Charge Conversion Induced by Hybrid Rashba and Dirac Surface States in Topological Insulator Heterostructures," *Nano Lett.*, vol. 19, no. 7, pp. 4420–4426, Jul. 2019.

[25] Y. Li *et al.*, "Large spin to charge conversion in the topological superconductor β-PdBi2 at room temperature," *Phys. Rev. B*, vol. 102, no. 1, p. 014420, Jul. 2020.

[26] R. Gans and R. G. Loyarte, "Die Permeabilität des Nickels für schnelle elektrische Schwingungen," *Ann. Phys.*, vol. 369, no. 3, pp. 209–249, Jan. 1921.

[27] J. Dorfmann, "Einige Bemerkungen zur Kenntnis des Mechanismus magnetischer Erscheinungen," *Zeitschrift für Phys.*, vol. 17, no. 1, pp. 98–111, Dec. 1923.

[28] T. L. Gilbert and J. M. Kelly, "Anomalous rotational damping in ferromagnetic sheets," in *Conference on Magnetism and Magnetic Materials*, 1955, pp. 253–263.

[29] J. H. E. Griffiths, "Anomalous high-frequency resistance of ferromagnetic metals [13]," *Nature*, vol. 158, no. 4019. Nature Publishing Group, pp. 670–671, 1946.

[30] C. Kittel, "On the theory of ferromagnetic resonance absorption," *Phys. Rev.*, vol. 73, no. 2, pp. 155–161, 1948.

[31] C. Kittel, "Ferromagnetic resonance," *J. Phys. le Radium*, vol. 12, no. 3, pp. 291–302,

Mar. 1951.

[32] M. Sharma, S. Pathak, and M. Sharm, "FMR Measurements of Magnetic Nanostructures," in *Ferromagnetic Resonance - Theory and Applications*, 2013, pp. 93–110.

[33] O. Yalçın, Ed., *Ferromagnetic Resonance: Theory and Applications*. Intech, 2013.

[34] E. Saitoh, M. Ueda, H. Miyajima, and G. Tatara, "Conversion of spin current into charge current at room temperature: Inverse spin-Hall effect," *Appl. Phys. Lett.*, vol. 88, no. 18, pp. 15–18, 2006.

[35] E. Beaurepaire, J. C. Merle, A. Daunois, and J. Y. Bigot, "Ultrafast spin dynamics in ferromagnetic nickel," *Phys. Rev. Lett.*, vol. 76, no. 22, pp. 4250–4253, May 1996.

[36] J. Güdde, U. Conrad, V. Jähnke, J. Hohlfeld, and E. Matthias, "Magnetization dynamics of ni and co films on cu(001) and of bulk nickel surfaces," *Phys. Rev. B - Condens. Matter Mater. Phys.*, vol. 59, no. 10, pp. R6608–R6611, Mar. 1999.

[37] G. P. Zhang and W. Hübner, "Laser-induced ultrafast demagnetization in ferromagnetic metals," *Phys. Rev. Lett.*, vol. 85, no. 14, pp. 3025–3028, Oct. 2000.

[38] M. Battiato, K. Carva, and P. M. Oppeneer, "Superdiffusive spin transport as a mechanism of ultrafast demagnetization," *Phys. Rev. Lett.*, vol. 105, no. 2, p. 027203, Jul. 2010.

[39] A. Eschenlohr *et al.*, "Ultrafast spin transport as key to femtosecond demagnetization," *Nat. Mater.*, vol. 12, no. 4, pp. 332–336, Apr. 2013.

[40] G. M. Choi, B. C. Min, K. J. Lee, and D. G. Cahill, "Spin current generated by thermally driven ultrafast demagnetization," *Nat. Commun.*, vol. 5, no. 1, pp. 1–8, Jul. 2014.

[41] B. Vodungbo *et al.*, "Indirect excitation of ultrafast demagnetization," *Sci. Rep.*, vol. 6, no. 1, pp. 1–9, Jan. 2016.

[42] A. J. Schellekens, W. Verhoeven, T. N. Vader, and B. Koopmans, "Investigating the

contribution of superdiffusive transport to ultrafast demagnetization of ferromagnetic thin films,” *Appl. Phys. Lett.*, vol. 102, no. 25, p. 252408, Jun. 2013.

[43] G. Salvatella, R. Gort, K. Bühlmann, S. Däster, A. Vaterlaus, and Y. Acremann, “Ultrafast demagnetization by hot electrons: Diffusion or super-diffusion?,” *Struct. Dyn.*, vol. 3, no. 5, p. 055101, Sep. 2016.

[44] T. Kampfrath *et al.*, “Terahertz spin current pulses controlled by magnetic heterostructures,” *Nat. Nanotechnol.*, vol. 8, no. 4, pp. 256–260, Mar. 2013.

[45] D. M. Mattox, *Handbook of Physical Vapor Deposition (PVD) Processing*. Elsevier, 2007.

[46] S. Pramanik *et al.*, “Observation of extremely long spin relaxation times in an organic nanowire spin valve,” *Nat. Nanotechnol.*, vol. 2, no. 4, pp. 216–219, Mar. 2007.

[47] J. Tsurumi *et al.*, “Coexistence of ultra-long spin relaxation time and coherent charge transport in organic single-crystal semiconductors,” *Nat. Phys.*, vol. 13, no. 10, pp. 994–998, Oct. 2017.

[48] M. Cinchetti *et al.*, “Determination of spin injection and transport in a ferromagnet/organic semiconductor heterojunction by two-photon photoemission,” *Nat. Mater.*, vol. 8, no. 2, pp. 115–119, Nov. 2009.

[49] C. Barraud *et al.*, “Unravelling the role of the interface for spin injection into organic semiconductors,” *Nat. Phys.*, vol. 6, no. 8, pp. 615–620, Jun. 2010.

[50] Y. Zhan *et al.*, “Efficient spin injection through exchange coupling at organic semiconductor/ferromagnet heterojunctions,” *Adv. Mater.*, vol. 22, no. 14, pp. 1626–1630, Apr. 2010.

[51] K. Ando, S. Watanabe, S. Mooser, E. Saitoh, and H. Sirringhaus, “Solution-processed

organic spin-charge converter," *Nat. Mater.*, vol. 12, no. 7, pp. 622–627, 2013.

[52] S. Mooser, J. F. K. Cooper, K. K. Banger, J. Wunderlich, and H. Sirringhaus, "Spin injection and transport in a solution-processed organic semiconductor at room temperature," *Phys. Rev. B - Condens. Matter Mater. Phys.*, vol. 85, no. 23, p. 235202, Jun. 2012.

[53] X. Sun, A. Bedoya-Pinto, R. Llopis, F. Casanova, and L. E. Hueso, "Flexible semi-transparent organic spin valve based on bathocuproine," *Appl. Phys. Lett.*, vol. 105, no. 8, p. 083302, Aug. 2014.

[54] H. L. Wang, C. H. Du, Y. Pu, R. Adur, P. C. Hammel, and F. Y. Yang, "Scaling of spin hall angle in 3d, 4d, and 5d metals from Y3Fe5 O12 /metal spin pumping," *Phys. Rev. Lett.*, vol. 112, no. 19, p. 197201, May 2014.

[55] C. Du, H. Wang, F. Yang, and P. C. Hammel, "Systematic variation of spin-orbit coupling with d -orbital filling: Large inverse spin Hall effect in 3d transition metals," *Phys. Rev. B - Condens. Matter Mater. Phys.*, vol. 90, no. 14, p. 140407, Oct. 2014.

[56] Z. V. Vardeny, *Organic spintronics*. CRC Press, 2010.

[57] S. Sanvito, "Molecular spintronics: The rise of spinterface science," *Nat. Phys.*, vol. 6, no. 8, pp. 562–564, Jun. 2010.

[58] M. Cinchetti, V. A. Dediu, and L. E. Hueso, "Activating the molecular spinterface," *Nature Materials*, vol. 16, no. 5. Nature Publishing Group, pp. 507–515, 25-Apr-2017.

[59] V. Dediu, M. Murgia, F. C. Matacotta, C. Taliani, and S. Barbanera, "Room temperature spin polarized injection in organic semiconductor," *Solid State Commun.*, vol. 122, no. 3–4, pp. 181–184, Apr. 2002.

[60] Z. H. Xiong, D. Wu, Z. V. Vardeny, and J. Shi, "Giant magnetoresistance in organic spin-

valves," *Nature*, vol. 427, no. 6977, pp. 821–824, Feb. 2004.

[61] C. Boehme and J. M. Lupton, "Challenges for organic spintronics," *Nature Nanotechnology*, vol. 8, no. 9. Nature Publishing Group, pp. 612–615, 04-Sep-2013.

[62] K. Ando, S. Watanabe, S. Mooser, E. Saitoh, and H. Sirringhaus, "Solution-processed organic spin-charge converter," *Nat. Mater.*, vol. 12, no. 7, pp. 622–627, Jul. 2013.

[63] S. Watanabe *et al.*, "Polaron spin current transport in organic semiconductors," *Nat. Phys.*, vol. 10, no. 4, pp. 308–313, Mar. 2014.

[64] S. J. Wang *et al.*, "Long spin diffusion lengths in doped conjugated polymers due to enhanced exchange coupling," *Nat. Electron.*, vol. 2, no. 3, pp. 98–107, Mar. 2019.

[65] Z. G. Yu, "Spin-orbit coupling, spin relaxation, and spin diffusion in organic solids," *Phys. Rev. Lett.*, vol. 106, no. 10, pp. 1–4, 2011.

[66] S. Watanabe *et al.*, "Polaron spin current transport in organic semiconductors," *Nat. Phys.*, vol. 10, no. 4, pp. 308–313, 2014.

[67] A. Wittmann *et al.*, "Tuning Spin Current Injection at Ferromagnet-Nonmagnet Interfaces by Molecular Design," *Phys. Rev. Lett.*, vol. 124, no. 2, p. 027204, Jan. 2020.

[68] E. Vetter *et al.*, "Tuning of spin-orbit coupling in metal-free conjugated polymers by structural conformation," *Phys. Rev. Mater.*, vol. 4, no. 8, p. 085603, Aug. 2020.

[69] S. a. Wolf *et al.*, "Spintronics: A Spin-Based Electronics Vision for the Future," *Science (80-.).*, vol. 294, no. 5546, pp. 1488–1495, 2001.

[70] S. D. Bader and S. S. P. Parkin, "Spintronics," *Annu. Rev. Condens. Matter Phys.*, vol. 1, no. 1, pp. 71–88, 2010.

[71] H. Nakayama *et al.*, "Geometry dependence on inverse spin Hall effect induced by spin pumping in Ni 81Fe 19/Pt films," *Phys. Rev. B - Condens. Matter Mater. Phys.*, vol. 85,

no. 14, pp. 1–7, 2012.

[72] Q. Song *et al.*, "Observation of inverse Edelstein effect in Rashba-split 2DEG between SrTiO3 and LaAlO3 at room temperature," *Sci. Adv.*, vol. 3, no. 3, Mar. 2017.

[73] S. Zhang and A. Fert, "Conversion between spin and charge currents with topological insulators," *Phys. Rev. B*, vol. 94, no. 18, pp. 1–5, 2016.

[74] H. Tetlow and M. Gradhand, "Semiconductor spintronics: Tuning the spin Hall effect in Si," *Phys. Rev. B - Condens. Matter Mater. Phys.*, vol. 87, no. 7, pp. 30–32, 2013.

[75] Y. Niimi *et al.*, "Extrinsic spin Hall effect induced by iridium impurities in copper," *Phys. Rev. Lett.*, vol. 106, no. 12, pp. 1–4, 2011.

[76] J. C. R. Sánchez *et al.*, "Spin-to-charge conversion using Rashba coupling at the interface between non-magnetic materials," *Nat. Commun.*, vol. 4, pp. 1–7, 2013.

[77] M. Jamali *et al.*, "Giant Spin Pumping and Inverse Spin Hall Effect in the Presence of Surface and Bulk Spin-Orbit Coupling of Topological Insulator Bi2Se3," *Nano Lett.*, vol. 15, no. 10, pp. 7126–7132, 2015.

[78] O. Mosendz, J. E. Pearson, F. Y. Fradin, G. E. W. Bauer, S. D. Bader, and A. Hoffmann, "Quantifying spin hall angles from spin pumping: Experiments and theory," *Phys. Rev. Lett.*, vol. 104, no. 4, Jan. 2010.

[79] J. B. S. Mendes *et al.*, "Efficient spin transport through polyaniline," *Phys. Rev. B*, vol. 95, no. 1, pp. 1–8, 2017.

[80] D. Sun *et al.*, "Inverse spin Hall effect from pulsed spin current in organic semiconductors with tunable spin-orbit coupling," *Nat. Mater.*, vol. 15, no. 8, pp. 863–869, Aug. 2016.

[81] L. Nuccio *et al.*, "Importance of spin-orbit interaction for the electron spin relaxation in organic semiconductors," *Phys. Rev. Lett.*, vol. 110, no. 21, May 2013.

[82] Z. G. Yu, "Spin-orbit coupling and its effects in organic solids," *Phys. Rev. B - Condens. Matter Mater. Phys.*, vol. 85, no. 11, 2012.

[83] H. Liu, J. Wang, M. Groesbeck, X. Pan, C. Zhang, and Z. V. Vardeny, "Studies of spin related processes in fullerene C60 devices," *J. Mater. Chem. C*, vol. 6, no. 14, pp. 3621–3627, 2018.

[84] S. Liang *et al.*, "Curvature-enhanced Spin-orbit Coupling and Spinterface Effect in Fullerene-based Spin Valves," *Sci. Rep.*, vol. 6, Jan. 2016.

[85] S.-J. Wang *et al.*, "Long spin diffusion lengths in doped conjugated polymers due to enhanced exchange coupling," *Nat. Electron.*, vol. accepted, no. March, 2019.

[86] I. A. Vonwald *et al.*, "Morphology, Structure, and Enhanced Intramolecular Conduction in Ultralong Conjugated Polymer Brushes," *J. Phys. Chem. C*, vol. 122, no. 14, pp. 7586–7596, 2018.

[87] R. Geng *et al.*, "Engineering of Spin Injection and Spin Transport in Organic Spin Valves Using π-Conjugated Polymer Brushes," *Adv. Funct. Mater.*, vol. 26, no. 22, pp. 3999–4006, 2016.

[88] Z. Qiu *et al.*, "Experimental investigation of spin Hall effect in indium tin oxide thin film," *Appl. Phys. Lett.*, vol. 103, no. 18, pp. 2011–2014, 2013.

[89] F. L. Bakker, A. Slachter, J. P. Adam, and B. J. Van Wees, "Interplay of peltier and seebeck effects in nanoscale nonlocal spin valves," *Phys. Rev. Lett.*, vol. 105, no. 13, pp. 1–4, 2010.

[90] A. N. Caruso *et al.*, "Defect contributions to conductivity in poly(3-hexylthiophene)?," *Phys. Status Solidi Basic Res.*, vol. 243, no. 6, pp. 1321–1330, 2006.

[91] C. Cerqueira *et al.*, "Evidence of Pure Spin-Current Generated by Spin Pumping in

Interface-Localized States in Hybrid Metal-Silicon-Metal Vertical Structures," *Nano Lett.*, vol. 19, no. 1, pp. 90–99, 2019.

[92] N. Kleinhenz *et al.*, "Ordering of Poly(3-hexylthiophene) in Solutions and Films: Effects of Fiber Length and Grain Boundaries on Anisotropy and Mobility," *Chem. Mater.*, vol. 28, no. 11, pp. 3905–3913, 2016.

[93] J. D. Roehling, I. Arslan, and A. J. Moulé, "Controlling microstructure in poly(3-hexylthiophene) nanofibers," *J. Mater. Chem.*, vol. 22, no. 6, pp. 2498–2506, 2012.

[94] J. Bardeen and W. H. Brattain, "Physical principles involved in transistor action," *Phys. Rev.*, vol. 75, no. 8, pp. 1208–1225, Apr. 1949.

[95] S. Datta and B. Das, "Electronic analog of the electro-optic modulator," *Appl. Phys. Lett.*, vol. 56, no. 7, pp. 665–667, Feb. 1990.

[96] N. N. Ledentsov *et al.*, "Radiative states in type-II GaSb/GaAs quantum wells," *Phys. Rev. B*, vol. 52, no. 19, pp. 14058–14066, Nov. 1995.

[97] S. Schmitt-Rink, D. S. Chemla, and D. A. B. Miller, "Linear and nonlinear optical properties of semiconductor quantum wells," *Adv. Phys.*, vol. 38, no. 2, pp. 89–188, Jan. 1988.

[98] V. Huard, R. T. Cox, K. Saminadayar, A. Arnoult, and S. Tatarenko, "Bound states in optical absorption of semiconductor quantum wells containing a two-dimensional electron gas," *Phys. Rev. Lett.*, vol. 84, no. 1, pp. 187–190, Jan. 2000.

[99] H. L. Störmer, R. Dingle, A. C. Gossard, W. Wiegmann, and M. D. Sturge, "Two-dimensional electron gas at a semiconductor-semiconductor interface," *Solid State Commun.*, vol. 29, no. 10, pp. 705–709, Mar. 1979.

[100] M. Sakano *et al.*, "Strongly spin-orbit coupled two-dimensional electron gas emerging

near the surface of polar semiconductors," *Phys. Rev. Lett.*, vol. 110, no. 10, p. 107204, Mar. 2013.

[101] L. Meier, G. Salis, I. Shorubalko, E. Gini, S. Schön, and K. Ensslin, "Measurement of Rashba and Dresselhaus spin-orbit magnetic fields," *Nat. Phys.*, vol. 3, no. 9, pp. 650–654, Jul. 2007.

[102] S. Datta, "How we proposed the spin transistor," *Nature Electronics*, vol. 1, no. 11. Nature Publishing Group, p. 604, 01-Nov-2018.

[103] E. I. Rashba, "Theory of electrical spin injection: Tunnel contacts as a solution of the conductivity mismatch problem," *Phys. Rev. B - Condens. Matter Mater. Phys.*, vol. 62, no. 24, p. R16267, Dec. 2000.

[104] G. Schmidt, D. Ferrand, L. Molenkamp, A. Filip, and B. van Wees, "Fundamental obstacle for electrical spin injection from a ferromagnetic metal into a diffusive semiconductor," *Phys. Rev. B - Condens. Matter Mater. Phys.*, vol. 62, no. 8, pp. R4790–R4793, Aug. 2000.

[105] H. J. Zhu, M. Ramsteiner, H. Kostial, M. Wassermeier, H. P. Schönherr, and K. H. Ploog, "Room-temperature spin injection from fe into GaAs," *Phys. Rev. Lett.*, vol. 87, no. 1, p. 016601, Jun. 2001.

[106] B. T. Jonker, G. Kioseoglou, A. T. Hanbicki, C. H. Li, and P. E. Thompson, "Electrical spin-injection into silicon from a ferromagnetic metal/tunnel barrier contact," *Nat. Phys.*, vol. 3, no. 8, pp. 542–546, Jul. 2007.

[107] G. Lampel, "Nuclear dynamic polarization by optical electronic saturation and optical pumping in semiconductors," *Phys. Rev. Lett.*, vol. 20, no. 10, pp. 491–493, Mar. 1968.

[108] D. T. Pierce and F. Meier, "Photoemission of spin-polarized electrons from GaAs," *Phys.*

Rev. B, vol. 13, no. 12, pp. 5484–5500, Jun. 1976.

[109] B. S. Mendoza and J. L. Cabellos, “Optical spin injection at semiconductor surfaces,” *Phys. Rev. B - Condens. Matter Mater. Phys.*, vol. 85, no. 16, p. 165324, Apr. 2012.

[110] F. Pezzoli *et al.*, “Optical spin injection and spin lifetime in Ge heterostructures,” *Phys. Rev. Lett.*, vol. 108, no. 15, p. 156603, Apr. 2012.

[111] K. Ando *et al.*, “Electrically tunable spin injector free from the impedance mismatch problem,” *Nat. Mater.*, vol. 10, no. 9, pp. 655–659, Jun. 2011.

[112] J. B. S. Mendes, A. Aparecido-Ferreira, J. Holanda, A. Azevedo, and S. M. Rezende, “Efficient spin to charge current conversion in the 2D semiconductor MoS2 by spin pumping from yttrium iron garnet,” *Appl. Phys. Lett.*, vol. 112, no. 24, p. 242407, Jun. 2018.

[113] E. Lesne *et al.*, “Highly efficient and tunable spin-to-charge conversion through Rashba coupling at oxide interfaces,” *Nat. Mater.*, vol. 15, no. 12, pp. 1261–1266, 2016.

[114] L. Cheng *et al.*, “Far out-of-equilibrium spin populations trigger giant spin injection into atomically thin MoS 2,” *Nature Physics*, vol. 15, no. 4. Nature Publishing Group, pp. 347–351, 01-Apr-2019.

[115] E. Vetter *et al.*, “Observation of carrier concentration dependent spintronic terahertz emission from n -GaN/NiFe heterostructures,” *Appl. Phys. Lett.*, vol. 117, no. 9, p. 093502, Aug. 2020.

[116] M. Tonouchi, “Cutting-edge terahertz technology,” *Nat. Photonics*, vol. 1, no. 2, pp. 97–105, 2007.

[117] S. Zhong, “Progress in terahertz nondestructive testing: A review,” *Frontiers of Mechanical Engineering*, vol. 14, no. 3. Higher Education Press, pp. 273–281, 01-Sep-

2019.

[118] S. Fan *et al.*, “Terahertz non-destructive imaging of cracks and cracking in structures of cement-based materials,” *AIP Adv.*, vol. 7, no. 11, Nov. 2017.

[119] A. Redo-Sanchez, N. Laman, B. Schulkin, and T. Tongue, “Review of terahertz technology readiness assessment and applications,” *Journal of Infrared, Millimeter, and Terahertz Waves*, vol. 34, no. 9. pp. 500–518, Sep-2013.

[120] M. Naftaly, N. Vieweg, and A. Deninger, “Industrial applications of terahertz sensing: State of play,” *Sensors (Switzerland)*, vol. 19, no. 19. MDPI AG, 01-Oct-2019.

[121] J. Federici and L. Moeller, “Review of terahertz and subterahertz wireless communications,” *Journal of Applied Physics*, vol. 107, no. 11. 01-Jun-2010.

[122] T. Kleine-Ostmann and T. Nagatsuma, “A review on terahertz communications research,” *Journal of Infrared, Millimeter, and Terahertz Waves*, vol. 32, no. 2. pp. 143–171, Feb-2011.

[123] H. J. Song and T. Nagatsuma, “Present and future of terahertz communications,” *IEEE Transactions on Terahertz Science and Technology*, vol. 1, no. 1. pp. 256–263, Sep-2011.

[124] S. Schlauderer *et al.*, “Temporal and spectral fingerprints of ultrafast all-coherent spin switching,” *Nature*, vol. 569, no. 7756, pp. 383–387, May 2019.

[125] J. Walowski and M. Münzenberg, “Perspective: Ultrafast magnetism and THz spintronics,” *J. Appl. Phys.*, vol. 120, no. 14, 2016.

[126] T. Kampfrath *et al.*, “Coherent terahertz control of antiferromagnetic spin waves,” *Nat. Photonics*, vol. 5, no. 1, pp. 31–34, Jan. 2011.

[127] T. Seifert *et al.*, “Efficient metallic spintronic emitters of ultrabroadband terahertz radiation,” *Nat. Photonics*, vol. 10, no. 7, pp. 483–488, 2016.

[128] Y. Wu *et al.*, “High-Performance THz Emitters Based on Ferromagnetic/Nonmagnetic Heterostructures,” *Adv. Mater.*, vol. 29, no. 4, Jan. 2017.

[129] D. Yang *et al.*, “Powerful and Tunable THz Emitters Based on the Fe/Pt Magnetic Heterostructure,” *Adv. Opt. Mater.*, vol. 4, no. 12, pp. 1944–1949, Dec. 2016.

[130] T. Seifert *et al.*, “Ultrabroadband single-cycle terahertz pulses with peak fields of 300 kV cm-1 from a metallic spintronic emitter,” *Appl. Phys. Lett.*, vol. 110, no. 25, Jun. 2017.

[131] H. Amano *et al.*, “The 2018 GaN power electronics roadmap,” *Journal of Physics D: Applied Physics*, vol. 51, no. 16. Institute of Physics Publishing, 26-Mar-2018.

[132] J. Y. Tsao *et al.*, “Ultrawide-Bandgap Semiconductors: Research Opportunities and Challenges,” *Advanced Electronic Materials*, vol. 4, no. 1. Blackwell Publishing Ltd, 01-Jan-2018.

[133] W. Stefanowicz *et al.*, “Experimental determination of Rashba spin-orbit coupling in wurtzite n -GaN:Si,” *Phys. Rev. B - Condens. Matter Mater. Phys.*, vol. 89, no. 20, May 2014.

[134] F. Kaess *et al.*, “Correlation between mobility collapse and carbon impurities in Si-doped GaN grown by low pressure metalorganic chemical vapor deposition,” *J. Appl. Phys.*, vol. 120, no. 10, Sep. 2016.

[135] W. Weber *et al.*, “Demonstration of Rashba spin splitting in GaN-based heterostructures,” *Appl. Phys. Lett.*, vol. 87, no. 26, pp. 1–3, 2005.

[136] J. H. Buß, J. Rudolph, F. Natali, F. Semond, and D. Hägele, “Temperature dependence of electron spin relaxation in bulk GaN,” *Phys. Rev. B - Condens. Matter Mater. Phys.*, vol. 81, no. 15, Apr. 2010.

[137] M. Battiato and K. Held, “Ultrafast and Gigantic Spin Injection in Semiconductors,” *Phys.*

Rev. Lett., vol. 116, no. 19, pp. 1–5, 2016.

[138] T. J. Huisman *et al.*, “Femtosecond control of electric currents in metallic ferromagnetic heterostructures,” *Nat. Nanotechnol.*, vol. 11, no. 5, pp. 455–458, May 2016.

[139] M. Chen, R. Mishra, Y. Wu, K. Lee, and H. Yang, “Terahertz Emission from Compensated Magnetic Heterostructures,” *Adv. Opt. Mater.*, vol. 6, no. 17, Sep. 2018.

[140] J. Shen, X. Fan, Z. Chen, M. F. Decamp, H. Zhang, and J. Q. Xiao, “Damping modulated terahertz emission of ferromagnetic films excited by ultrafast laser pulses,” *Appl. Phys. Lett.*, vol. 101, no. 7, Aug. 2012.

[141] T. Kleine-Ostmann, M. Koch, and P. Dawson, “Modulation of THz radiation by semiconductor nanostructures,” *Microw. Opt. Technol. Lett.*, vol. 35, no. 5, pp. 343–345, Dec. 2002.

[142] D. Takane, S. Souma, T. Sato, T. Takahashi, K. Segawa, and Y. Ando, “Work function of bulk-insulating topological insulator Bi2-xSbxTe3-ySey,” *Appl. Phys. Lett.*, vol. 109, no. 9, Aug. 2016.

[143] J. I. Pankove and H. Schade, “Photoemission from GaN,” *Appl. Phys. Lett.*, vol. 25, no. 1, pp. 53–55, 1974.

[144] J. Wang *et al.*, “Spin-optoelectronic devices based on hybrid organic-inorganic trihalide perovskites,” *Nat. Commun.*, vol. 10, no. 1, pp. 1–6, 2019.

[145] C. Zhang *et al.*, “Magnetic field effects in hybrid perovskite devices,” *Nat. Phys.*, vol. 11, no. 5, pp. 427–434, 2015.

[146] P. Odenthal *et al.*, “Spin-polarized exciton quantum beating in hybrid organic-inorganic perovskites,” *Nat. Phys.*, vol. 13, no. 9, pp. 894–899, 2017.

[147] D. Giovanni *et al.*, “Highly spin-polarized carrier dynamics and ultralarge photoinduced

magnetization in CH3NH3PbI3 perovskite thin films," *Nano Lett.*, vol. 15, no. 3, pp. 1553–1558, 2015.

[148] D. Niesner *et al.*, "Giant Rashba Splitting in CH3NH3PbBr3 Organic-Inorganic Perovskite," *Phys. Rev. Lett.*, vol. 117, no. 12, pp. 1–6, 2016.

[149] M. Kepenekian, R. Robles, C. Katan, D. Sapori, L. Pedesseau, and J. Even, "Rashba and Dresselhaus Effects in Hybrid Organic-Inorganic Perovskites: From Basics to Devices," *ACS Nano*, vol. 9, no. 12, pp. 11557–11567, 2015.

[150] J. Yin *et al.*, "Layer-Dependent Rashba Band Splitting in 2D Hybrid Perovskites," *Chem. Mater.*, vol. 30, no. 23, pp. 8538–8545, 2018.

[151] Y. Zhai *et al.*, "Giant Rashba splitting in 2D organic-inorganic halide perovskites measured by transient spectroscopies," *Sci. Adv.*, vol. 3, no. 7, p. e1700704, Jul. 2017.

[152] M. Sajedi *et al.*, "Absence of a giant Rashba effect in the valence band of lead halide perovskites," *Phys. Rev. B*, vol. 102, no. 8, p. 081116, Aug. 2020.

[153] S. Yang, E. Vetter, T. Wang, A. Amassian, and D. Sun, " Observation of long spin lifetime in MAPbBr 3 single crystals at room temperature ," *J. Phys. Mater.*, vol. 3, no. 1, p. 015012, Jan. 2020.

[154] S. A. Wolf *et al.*, "Spintronics: A spin-based electronics vision for the future," *Science (80-.).*, vol. 294, no. 5546, pp. 1488–1495, Nov. 2001.

[155] A. Hoffmann, "Spin hall effects in metals," *IEEE Trans. Magn.*, vol. 49, no. 10, pp. 5172–5193, 2013.

[156] J. Sinova, D. Culcer, Q. Niu, N. A. Sinitsyn, T. Jungwirth, and A. H. MacDonald, "Universal intrinsic spin Hall effect," *Phys. Rev. Lett.*, vol. 92, no. 12, 2004.

[157] K. Ando, T. Yoshino, and E. Saitoh, "Optimum condition for spin-current generation from

magnetization precession in thin film systems," *Appl. Phys. Lett.*, vol. 94, no. 15, 2009.

[158] T. Kimura, Y. Otani, T. Sato, S. Takahashi, and S. Maekawa, "Room-temperature reversible spin hall effect," *Phys. Rev. Lett.*, vol. 98, no. 15, 2007.

[159] V. Garcia *et al.*, "Ferroelectric control of spin polarization," *Science (80-.).*, vol. 327, no. 5969, pp. 1106–1110, 2010.

[160] K. I. Uchida, H. Adachi, T. Ota, H. Nakayama, S. Maekawa, and E. Saitoh, "Observation of longitudinal spin-Seebeck effect in magnetic insulators," *Appl. Phys. Lett.*, vol. 97, no. 17, 2010.

[161] S. Gardelis, C. G. Smith, C. H. W. Barnes, E. H. Linfield, and D. A. Ritchie, "Spin-valve effects in a semiconductor field-effect transistor: A spintronic device," *Phys. Rev. B - Condens. Matter Mater. Phys.*, vol. 60, no. 11, pp. 7764–7767, 1999.

[162] K. Ando *et al.*, "Electric manipulation of spin relaxation using the spin hall effect," *Phys. Rev. Lett.*, vol. 101, no. 3, 2008.

[163] A. Manchon and S. Zhang, "Theory of spin torque due to spin-orbit coupling," *Phys. Rev. B - Condens. Matter Mater. Phys.*, vol. 79, no. 9, 2009.

[164] Y. Ji, A. Hoffmann, J. S. Jiang, and S. D. Bader, "Spin injection, diffusion, and detection in lateral spin-valves," *Appl. Phys. Lett.*, vol. 85, no. 25, pp. 6218–6220, 2004.

[165] E. Saitoh, M. Ueda, H. Miyajima, and G. Tatara, "Conversion of spin current into charge current at room temperature: Inverse spin-Hall effect," *Appl. Phys. Lett.*, vol. 88, no. 18, p. 182509, May 2006.

[166] L. Liu, T. Moriyama, D. C. Ralph, and R. A. Buhrman, "Spin-torque ferromagnetic resonance induced by the spin Hall effect," *Phys. Rev. Lett.*, vol. 106, no. 3, 2011.

[167] K. Shen, G. Vignale, and R. Raimondi, "Microscopic theory of the inverse Edelstein

effect," *Phys. Rev. Lett.*, vol. 112, no. 9, 2014.

[168] W. Zhang, M. B. Jungfleisch, W. Jiang, J. E. Pearson, and A. Hoffmann, "Spin pumping and inverse Rashba-Edelstein effect in NiFe/Ag/Bi and NiFe/Ag/Sb," *J. Appl. Phys.*, vol. 117, no. 17, 2015.

[169] M. A. Brand *et al.*, "Precession and Motional Slowing of Spin Evolution in a High Mobility Two-Dimensional Electron Gas," *Phys. Rev. Lett.*, vol. 89, no. 23, 2002.

[170] B. Guzelturk *et al.*, "Terahertz Emission from Hybrid Perovskites Driven by Ultrafast Charge Separation and Strong Electron–Phonon Coupling," *Adv. Mater.*, vol. 30, no. 11, pp. 1–8, 2018.

[171] J. Li and P. M. Haney, "Optical spintronics in organic-inorganic perovskite photovoltaics," *Phys. Rev. B*, vol. 93, no. 15, 2016.

[172] C. Zhang, D. Sun, and Z. V. Vardeny, "Multifunctional Optoelectronic–Spintronic Device Based on Hybrid Organometal Trihalide Perovskites," *Adv. Electron. Mater.*, vol. 3, no. 2, 2017.

[173] A. Kojima, K. Teshima, Y. Shirai, and T. Miyasaka, "Organometal halide perovskites as visible-light sensitizers for photovoltaic cells," *J. Am. Chem. Soc.*, vol. 131, no. 17, pp. 6050–6051, 2009.

[174] J. Burschka *et al.*, "Sequential deposition as a route to high-performance perovskite-sensitized solar cells," *Nature*, vol. 499, no. 7458, pp. 316–319, 2013.

[175] D. H. Cao, C. C. Stoumpos, O. K. Farha, J. T. Hupp, and M. G. Kanatzidis, "2D Homologous Perovskites as Light-Absorbing Materials for Solar Cell Applications," *J. Am. Chem. Soc.*, vol. 137, no. 24, pp. 7843–7850, 2015.

[176] G. Grancini *et al.*, "One-Year stable perovskite solar cells by 2D/3D interface

engineering," *Nat. Commun.*, vol. 8, pp. 1–8, 2017.

[177] S. D. Stranks *et al.*, "Electron-Hole Diffusion Lengths Exceeding," vol. 342, no. October, pp. 341–345, 2013.

[178] M. Yuan *et al.*, "Perovskite energy funnels for efficient light-emitting diodes," *Nat. Nanotechnol.*, vol. 11, no. 10, pp. 872–877, 2016.

[179] Z. Xiao *et al.*, "Efficient perovskite light-emitting diodes featuring nanometre-sized crystallites," *Nat. Photonics*, vol. 11, no. 2, pp. 108–115, 2017.

[180] K. Lin *et al.*, "Perovskite light-emitting diodes with external quantum efficiency exceeding 20 per cent," *Nature*, vol. 562, no. 7726, pp. 245–248, 2018.

[181] M. Saliba *et al.*, "Structured Organic-Inorganic Perovskite toward a Distributed Feedback Laser," *Adv. Mater.*, vol. 28, no. 5, pp. 923–929, 2016.

[182] P. Liu, X. He, J. Ren, Q. Liao, J. Yao, and H. Fu, "Organic-Inorganic Hybrid Perovskite Nanowire Laser Arrays," *ACS Nano*, vol. 11, no. 6, pp. 5766–5773, 2017.

[183] S. Chen *et al.*, "A Photonic Crystal Laser from Solution Based Organo-Lead Iodide Perovskite Thin Films," *ACS Nano*, vol. 10, no. 4, pp. 3959–3967, 2016.

[184] C. Bao *et al.*, "Low-Noise and Large-Linear-Dynamic-Range Photodetectors Based on Hybrid-Perovskite Thin-Single-Crystals," *Adv. Mater.*, vol. 29, no. 39, 2017.

[185] L. Dou *et al.*, "Solution-processed hybrid perovskite photodetectors with high detectivity," *Nat. Commun.*, vol. 5, p. 5404, 2014.

[186] L. Shen *et al.*, "A Self-Powered, Sub-nanosecond-Response Solution-Processed Hybrid Perovskite Photodetector for Time-Resolved Photoluminescence-Lifetime Detection," *Adv. Mater.*, vol. 28, no. 48, pp. 10794–10800, 2016.

[187] M. I. Saidaminov *et al.*, "Planar-integrated single-crystalline perovskite photodetectors,"

Nat. Commun., vol. 6, p. 8724, 2015.

[188] A. Walsh, “Principles of chemical bonding and band gap engineering in hybrid organic-inorganic halide perovskites,” *J. Phys. Chem. C*, vol. 119, no. 11, pp. 5755–5760, 2015.

[189] D. Niesner *et al.*, “ Structural fluctuations cause spin-split states in tetragonal (CH 3 NH 3)PbI 3 as evidenced by the circular photogalvanic effect ,” *Proc. Natl. Acad. Sci.*, vol. 115, no. 38, pp. 9509–9514, 2018.

[190] E. Mosconi, T. Etienne, and F. De Angelis, “Rashba Band Splitting in Organohalide Lead Perovskites: Bulk and Surface Effects,” *J. Phys. Chem. Lett.*, vol. 8, no. 10, pp. 2247–2252, 2017.

[191] P. Haney *et al.*, “Giant Rashba splitting in 2D organic-inorganic halide perovskites measured by transient spectroscopies,” *Sci. Adv.*, vol. 3, no. 7, p. e1700704, 2017.

[192] K. Frohna *et al.*, “Inversion symmetry and bulk Rashba effect in methylammonium lead iodide perovskite single crystals,” *Nat. Commun.*, vol. 9, no. 1, p. 1829, 2018.

[193] J. Xu, T. Zhu, Y. K. Luo, Y. M. Lu, and R. K. Kawakami, “Strong and Tunable Spin-Lifetime Anisotropy in Dual-Gated Bilayer Graphene,” *Phys. Rev. Lett.*, vol. 121, no. 12, 2018.

[194] M. I. Saidaminov *et al.*, “High-quality bulk hybrid perovskite single crystals within minutes by inverse temperature crystallization,” *Nat. Commun.*, vol. 6, p. 7586, 2015.

[195] V. Castel, N. Vlietstra, B. J. Van Wees, and J. Ben Youssef, “Frequency and power dependence of spin-current emission by spin pumping in a thin-film YIG/Pt system,” *Phys. Rev. B - Condens. Matter Mater. Phys.*, vol. 86, no. 13, 2012.

[196] Y. Tserkovnyak, A. Brataas, G. E. W. Bauer, and B. I. Halperin, “Nonlocal magnetization dynamics in ferromagnetic heterostructures,” *Rev. Mod. Phys.*, vol. 77, no. 4, pp. 1375–

1421, 2005.

[197] M. Johnson and R. H. Silsbee, "Interfacial charge-spin coupling: Injection and detection of spin magnetization in metals," *Phys. Rev. Lett.*, vol. 55, no. 17, pp. 1790–1793, 1985.

[198] T. Maassen, I. J. Vera-Marun, M. H. D. Guimarães, and B. J. Van Wees, "Contact-induced spin relaxation in Hanle spin precession measurements," *Phys. Rev. B - Condens. Matter Mater. Phys.*, vol. 86, no. 23, 2012.

[199] J. Li, B. Huang, and I. Appelbaum, "Oblique Hanle effect in semiconductor spin transport devices," *Appl. Phys. Lett.*, vol. 92, no. 14, 2008.

[200] F. Zheng, L. Z. Tan, S. Liu, and A. M. Rappe, "Rashba spin-orbit coupling enhanced carrier lifetime in CH 3 NH 3 PbI 3," *Nano Lett.*, vol. 15, no. 12, pp. 7794–7800, 2015.

[201] D. Sun *et al.*, "Surface-enhanced spin current to charge current conversion efficiency in CH3NH3PbBr3-based devices," *J. Chem. Phys.*, vol. 151, no. 17, 2019.

[202] J. C. Rojas-Sánchez *et al.*, "Spin to Charge Conversion at Room Temperature by Spin Pumping into a New Type of Topological Insulator: α -Sn Films," *Phys. Rev. Lett.*, vol. 116, no. 9, 2016.

[203] H. Wang *et al.*, "Surface-State-Dominated Spin-Charge Current Conversion in Topological-Insulator-Ferromagnetic-Insulator Heterostructures," *Phys. Rev. Lett.*, vol. 117, no. 7, 2016.

[204] M. Kepenekian and J. Even, "Rashba and Dresselhaus Couplings in Halide Perovskites: Accomplishments and Opportunities for Spintronics and Spin-Orbitronics," *J. Phys. Chem. Lett.*, vol. 8, no. 14, pp. 3362–3370, 2017.

[205] Z. G. Yu and Y. S. Li, "Unraveling the Spin Relaxation Mechanism in Hybrid Organic-Inorganic Perovskites," *J. Phys. Chem. C*, vol. 123, no. 23, pp. 14701–14706, 2019.

[206] P. Deorani *et al.*, “Observation of inverse spin hall effect in bismuth selenide,” *Phys. Rev. B - Condens. Matter Mater. Phys.*, vol. 90, no. 9, 2014.

[207] M. Harder, Y. Gui, and C. M. Hu, “Electrical detection of magnetization dynamics via spin rectification effects,” *Phys. Rep.*, vol. 661, pp. 1–59, 2016.

[208] A. Tsukahara *et al.*, “Self-induced inverse spin Hall effect in permalloy at room temperature,” *Phys. Rev. B - Condens. Matter Mater. Phys.*, vol. 89, no. 23, 2014.

[209] R. Iguchi and E. Saitoh, “Measurement of spin pumping voltage separated from extrinsic microwave effects,” *J. Phys. Soc. Japan*, vol. 86, no. 1, 2017.

[210] W. J. H. Leyland, R. T. Harley, M. Henini, A. J. Shields, I. Farrer, and D. A. Ritchie, “Oscillatory Dyakonov-Perel spin dynamics in two-dimensional electron gases,” *Phys. Rev. B - Condens. Matter Mater. Phys.*, vol. 76, no. 19, 2007.

[211] Y. Liu, Z. Yang, and S. F. Liu, “Recent Progress in Single-Crystalline Perovskite Research Including Crystal Preparation, Property Evaluation, and Applications,” *Adv. Sci.*, vol. 5, no. 1, 2018.

[212] J. Wang *et al.*, “Spin-optoelectronic devices based on hybrid organic-inorganic trihalide perovskites,” *Nat. Commun.*, vol. 10, no. 1, p. 129, 2019.

[213] R. Wang, S. Hu, X. Yang, X. Yan, H. Li, and C. Sheng, “Circularly polarized photoluminescence and Hanle effect measurements of spin relaxation in organic-inorganic hybrid perovskite films,” *J. Mater. Chem. C*, vol. 6, no. 12, pp. 2989–2995, 2018.

[214] X. Liu, H. Zhang, B. Zhang, J. Dong, W. Jie, and Y. Xu, “Charge Transport Behavior in Solution-Grown Methylammonium Lead Tribromide Perovskite Single Crystal Using α Particles,” *J. Phys. Chem. C*, vol. 122, no. 26, pp. 14355–14361, 2018.

[215] C. L. Tien, T. W. Lin, K. C. Yu, T. Y. Tsai, and H. F. Shih, “Evaluation of Electrical,

Mechanical Properties, and Surface Roughness of DC Sputtering Nickel-Iron Thin Films," *IEEE Trans. Magn.*, vol. 50, no. 7, 2014.

[216] M. Matsushima *et al.*, "Quantitative investigation of the inverse Rashba-Edelstein effect in Bi/Ag and Ag/Bi on YIG," *Appl. Phys. Lett.*, vol. 110, no. 7, 2017.

[217] M. Isasa *et al.*, "Origin of inverse Rashba-Edelstein effect detected at the Cu/Bi interface using lateral spin valves," *Phys. Rev. B*, vol. 93, no. 1, 2016.

[218] J. B. S. Mendes *et al.*, "Spin-Current to Charge-Current Conversion and Magnetoresistance in a Hybrid Structure of Graphene and Yttrium Iron Garnet," *Phys. Rev. Lett.*, vol. 115, no. 22, 2015.